Predicting bed grain size in Maine rivers using lidar topographic data

Author: Andrew Olaf Nesheim

Boston College

The Graduate School of Arts and Sciences

Department of Geology and Geophysics

PREDICTING BED GRAIN SIZE IN MAINE RIVERS USING LIDAR TOPOGRAPHIC DATA

a thesis

by

ANDREW OLAF NESHEIM

submitted in partial fulfillment of the requirements

for the degree of

Master of Science

2011

Abstract

Predicting bed grain size in Maine rivers using lidar topographic data

Andrew O. Nesheim

Advisor: Noah Snyder

River channel morphology in northern New England depends on channel position relative to glacial geomorphology and history. This thesis considers three paraglacial Maine rivers: the West Branch of the Pleasant River (WBPR), a steep inland imposed-form tributary of the Piscataquis River, and the Narraguagus and Sheepscot rivers, two coastal low-gradient rivers. I use a simple model based on the Shields and Manning equations to predict median bed grain size in these recently deglaciated watersheds. The main objectives of this study are to: (1) understand how bedrock controls on the longitudinal profile and sediment inputs impact substrate grain size and channel morphology in the WBPR; (2) apply a model predicting substrate grain size based on digital elevation model (DEM)-derived geometric channel parameters; (3) compare the results from the high-gradient WBPR to previously studied low-gradient coastal Maine rivers; and (4) explore the implications of my findings on channel and habitat restoration in paraglacial rivers. I use standard and lidar (light detection and ranging) digital elevation models (DEMs) and spatial analyses to measure channel parameters necessary to predict bed grain size and compare them to field measurements. Predicted bed grain size falls within a factor of two of the field-measured median in ~70% of the study sites. The model performs best in supply-limited alluvial single-thread channel segments with gravel-cobble lag deposit beds, and is less successful in transport-limited depositional segments with relatively fine

beds and greater channel variability. Channel segments that are transitional between these two cases (intermediate channel complexity and grain size) are associated with intermediate grain size prediction accuracy. Model failures occur in segments that deviate from the single-thread gravel-bed channel type, and may indicate areas to focus restoration efforts. This study builds on previous research on low-gradient coastal rivers in Maine, and has wide application to future research or restoration projects concerned with sediment mobilization and fluvial ecology.

Acknowledgments

TO THE

Friends and Companions

WHO HAVE SHARED WITH HIM THE PLEASURES OF CAMPING OUT
IN THE WOODS OF MAINE,

THE AUTHOR

AFFECTIONATELY DEDICATES THIS LITTLE VOLUME,

IN THE EARNEST HOPE THAT, EVEN IF IT SHOULD CONTAIN
NOTHING NEW TO THEM, IT WILL AT LEAST SERVE
TO RECALL BRIGHT MEMORIES OF DAYS
THAT ARE PAST.

(From Hubbard, 1882; p. 17)

This research was funded by the National Science Foundation (GEO-EAR Geomorphology and Land Use Dynamics and Education and Human Resources, award #0645343).

Thanks to Stephanie Strouse, as well as Mike Cuttler, David Santaniello, Susie Bresney, Dan Hallstrom and Kim Rhodes at Boston College for braving the beavers and bloodsuckers of the West Branch -- this project would have been impossible without your help.

Thank you to Doug Edmonds and Alan Kafka for their general wisdom and careful reviews, and special thanks to Noah Snyder for funding this project and providing thoughtful guidance and support during my time at BC.

Table of contents

List of Figures

List of Tables

1. INTRODUCTION

1.1 Motivation

The morphology of rivers of the northeastern United States is dictated by the glacial history of the region, as the underlying terrain is set by recent glacial erosion and deposition. This glacial legacy determines the longitudinal profile of channels and directly influences sediment supply, channel geometry and substrate characteristics. In this thesis, I use Geographic Information Systems (GIS)-derived channel parameters to predict bed grain size in several Maine rivers. I focus on the relatively high gradient West Branch of the Pleasant River (WBPR) and compare the results to two lower-gradient coastal rivers in Maine (the Narraguagus and Sheepscot rivers). The predictions in this study are useful for informing future channel and habitat restoration efforts as well as understanding controls on channel morphology and substrate in different glacial settings (Snyder et al., 2008).

Atlantic salmon habitat suitability is a key driver of current stream research and restoration in Maine, and understanding the impact of river processes on species habitat quality is a primary motivation for this study. The majority of research addressing links between fluvial geomorphology and habitat focuses on the rivers of the Pacific Northwest (e.g., Montgomery et al., 1999; Pess et al., 2002; Buffington et al., 2004), but several studies examine rivers in northern New England and the neighboring provinces of Atlantic Canada with similar geologic and land use histories (namely, postglacial and logging-influenced). Within this environment, high-relief river systems in Canada have received the most attention (Coloumbe-Pontbriand and LaPointe, 2004; Hedger

et al., 2006; Davey and LaPointe, 2007). These study areas are valuable references and comparisons for the relatively unstudied WBPR. An increasing amount of research has also been conducted on low-gradient river systems along the northeastern coast of the United States (e.g., Magilligan et al., 2008), including the Narraguagus and Sheepscot rivers (Snyder et al., 2008; Wilkins and Snyder, 2011; Strouse, in progress).

Median grain size (D_{50}) is an important parameter for assessing potential salmon habitat and restoration efforts, as Atlantic salmon are known to spawn and rear in gravel-bedded rivers with a median grain size of 16-256 mm (Kondolf and Wolman, 1993). Assessing changes in bed grain size along the longitudinal profile of channels is critical for determining the location of likely salmon habitat. Predicting bed grain size using GIS is a useful for reducing resource-intensive fieldwork associated with typical grain size surveys, as well as prioritizing restoration projects (e.g., dam removals and culvert replacements) based on potential impact on habitat. Several papers have focused on the relationship between GIS-based channel geomorphic data and fish habitat, and they serve as important reference points for this study (Buffington et al., 2004; Coloumbe-Pontbriand and LaPointe, 2004; Legleiter et al., 2004; Hedger et al., 2006; Davey and LaPointe, 2007; Neeson et al., 2007; Donaldson et al., 2009; Donaldson and Sklar, 2010; Kim and LaPointe, 2010; Wilkins and Snyder, 2011). Both the Wilkins and Snyder (2011) and Buffington et al. (2004) studies focused on the influence of channel morphology on salmon habitat availability, and these models provide the basis for habitat mapping on the West Branch of the Pleasant River. Wilkins and Snyder (2011) found that predictions of grain size using geographic information systems (GIS) analysis are well-

supported by field measurements with 62-70% of the falling within a factor of two. I extend the application of this model and test it on both coastal low-gradient and inland high-gradient rivers in Maine.

1.2 Study locations and land use history

The primary field area for this thesis, the WBPR, is an inland tributary of the Piscataquis River, which flows into the Penobscot River in central Maine. It is located in a relatively remote area of the state, inland of the coastal Narraguagus and Sheepscot rivers (Figures 1-3). The area has been subject to large-scale timber harvest since the 18th century, and a significant portion of the WBPR watershed consists of privately owned land managed for timber harvest (Wilson, 2005). Much of the forest cover in the watershed is new growth from the past 50-100 years, and from 1850-1941 the river was used for transporting the cut wood from the upstream part of the watershed to the Penobscot River in large log drives (Shangraw, 2005). These drives led to significant changes to the channel, including widening of the "Jaws," the narrowest part of the steep 4-km-long gorge known as Gulf Hagas, from 2.4 m to 8.2 m in order to facilitate log passage (Figures 4-6; Shangraw, 2005). The presence of numerous former logging camps along the WBPR speaks to the legacy of logging activity in the area.[1] The camp at Little Lyford Pond is a notable example (Figures 7-9). A significant anthropogenic influence unique to the WBPR is the presence of Katahdin Iron Works (KI), a major iron production site that was operational from 1840-1890 (Maine Geological Survey, 2005).

[1] The Appalachian Mountain Club's Little Lyford Pond Camps (along with several other camps in Piscataquis County) are located at the sites of former temporary logging camps built in 1874 and designed to accommodate seasonal loggers (Shangraw, 2005).

The ironworks facilities took advantage of local sulfide ores, and 16 smelting kilns and a blast furnace (now demolished, save for a single partially restored kiln) were located near the channel (Eastman, 1967; Figures 10-11). A dam was built across the WBPR to provide power to the bellows of the blast furnace, and remnants of this dam are still visible today at the outlet of Silver Lake (Figures 11-13).

The Narraguagus and Sheepscot rivers are both classified as coastal rivers, as they flow directly into the Gulf of Maine. Similar to the WBPR, the Narraguagus River watershed has a history of extensive logging, and until around 1900 cut wood was transported down the mainstem and tributaries of the river using temporary splash dams (Kasprak et al., 2011). Today approximately 60% of the Narraguagus watershed is privately managed for timber harvest (Arter, 2003). A number of mill dams were also built on the relatively low-gradient river, but no dams remain besides a small ice control facility at Cherryfield (Kasprak et al., 2011). The Sheepscot River (including both the mainstem and west branch) is the southwestern-most study river, and is also a low-gradient system. The river was historically used for hydropower milling operations, due to its close proximity to populated areas, and several former mill dams are still present along the channel. The watershed consists primarily of private and agricultural land, and was heavily deforested subsequent to European settlement. The overall forest cover in eastern coastal Maine has increased approximately 18-22% from 1880 to 1995, and the change in the Sheepscot basin has been particularly dramatic with an increase in forest cover of 100-186% as formerly cleared agricultural land becomes reforested (Irland, 1998).

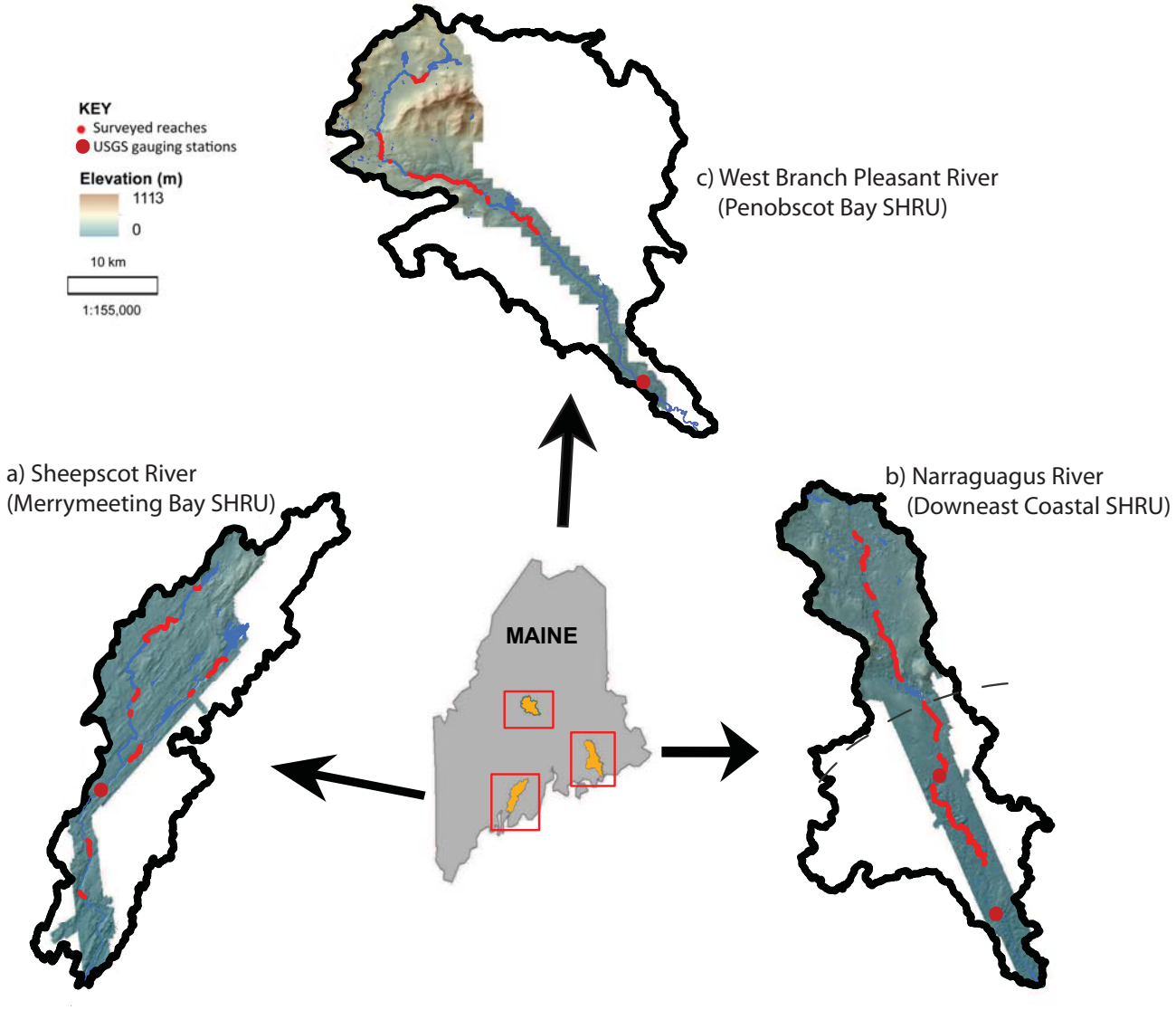

Figure 1. The Maine reference map indicates the location of the three study rivers within the three federally designated Salmon Habitat Recovery Units (SHRUs) of the Gulf of Maine Distinct Population Segment (GOM DPS) of Atlantic salmon. The detail maps delineate the locations of the lidar data collection areas within the watersheds, and the dashed black line on the Narraguagus marks the approximate Pleistocene sea level highstand paleo-shoreline.

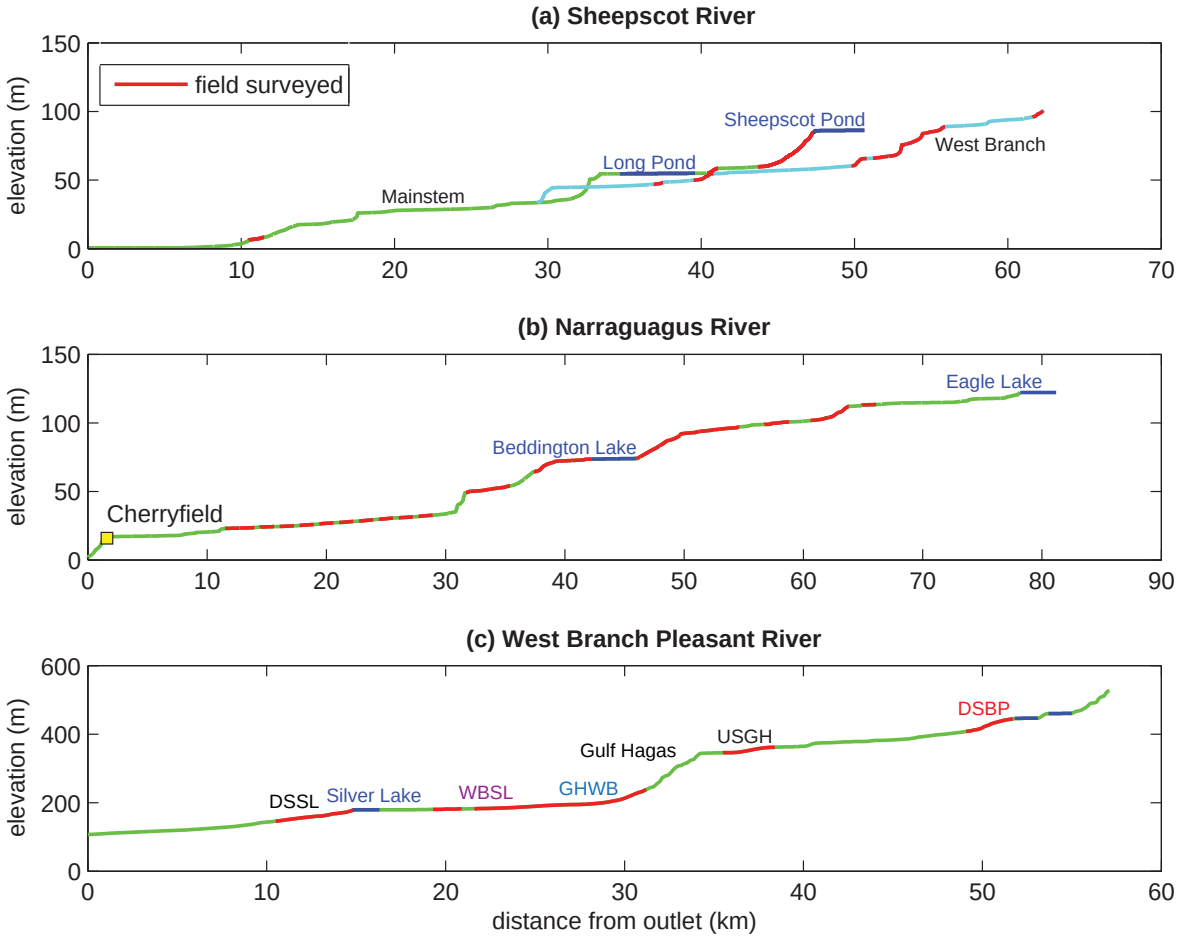

Figure 2. The three panels show longitudinal profiles of all three study rivers: the Sheepscot (a), Narraguagus (b) and WBPR (c). The channel profiles are resolved from 10 meter DEMs and correspond with the lidar data collection areas from Figure 1. The surveyed channel segments are labelled for the WBPR (c), and the dashed line marks the boundary between the GHWB and WBSL segments.

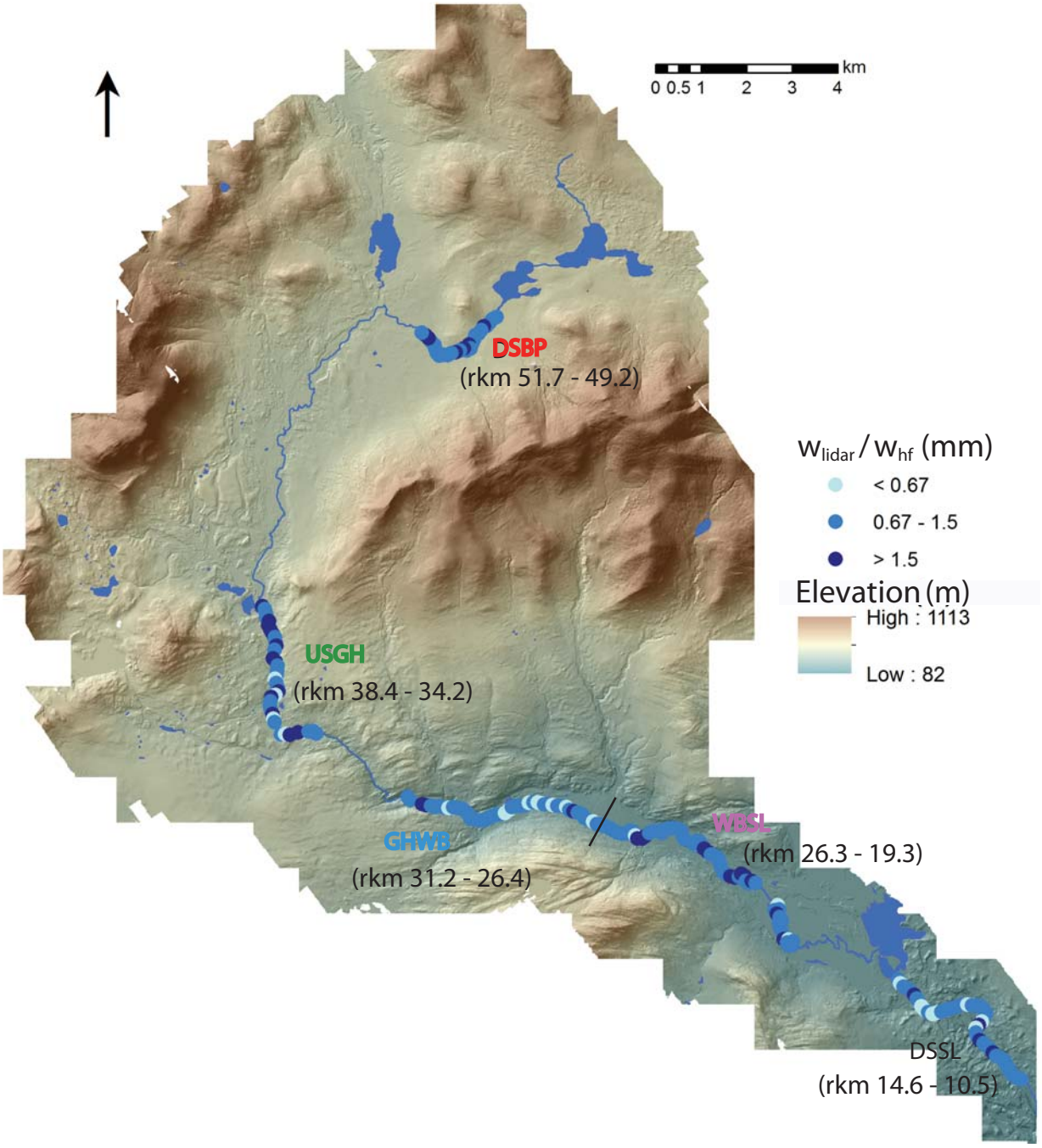

Figure 3. Locations of field surveyed segments of the WBPR. The blue points represent the ratio of GIS-measured width (w_{lidar}) to field-measured width (w_{hf}).

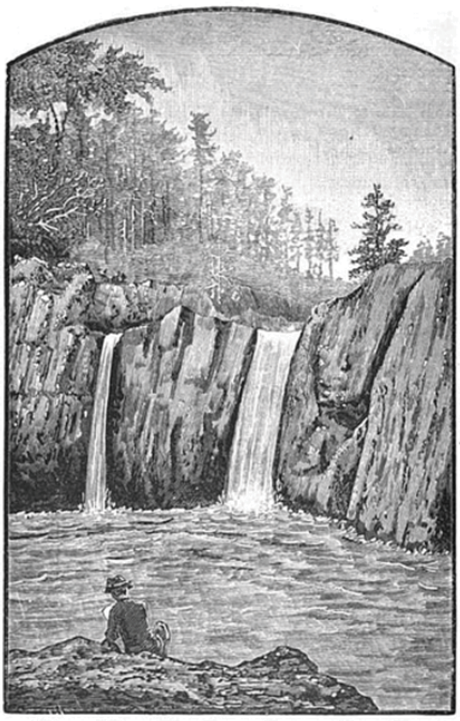

Billings' Falls, West Branch Pleasant River, Me.

Figure 4. A lithograph of Billings' Falls in Gulf Hagas on the WBPR at moderate flow (Farrar, 1880)

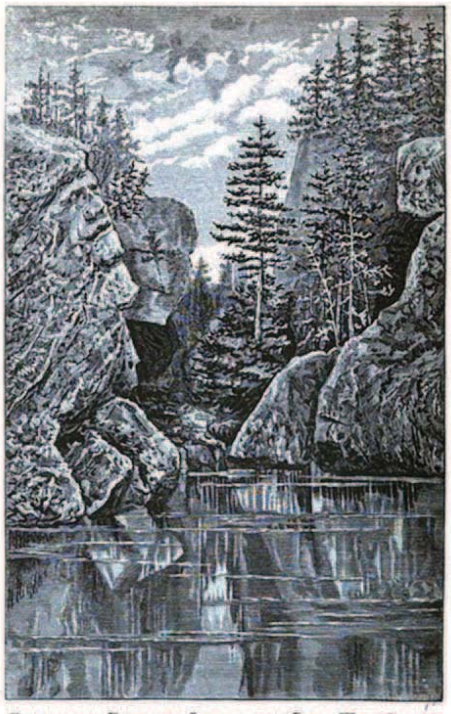

Face in the Rock and Jaws of the Gulf, West Branch Pleasant River, Me.

Figure 5. A lithograph of the "Jaws" near the base of Gulf Hagas on the WBPR (Farrar, 1880)

BILLING'S FALLS—IN THE GULF.

Figure 6. An 1882 photo of Billings' Falls on the WBPR at high flow (Hubbard, 1882). The lumber in the lower right of the frame is an artifact of extensive of logging in the WBPR watershed. The falls in this photo correspond with the location shown in Figure 4.

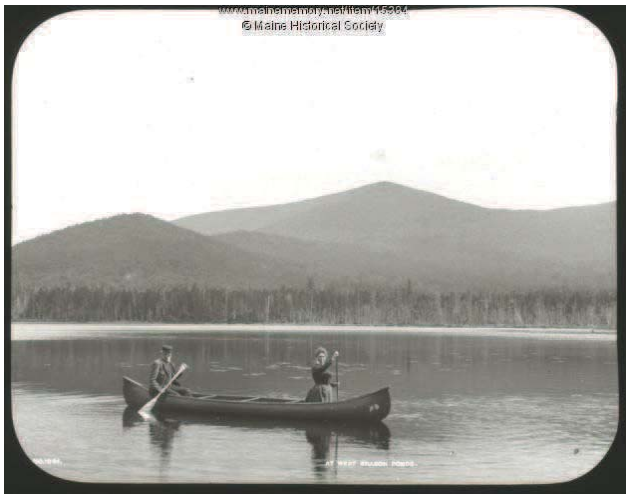

Figure 7. A photo of West Branch Pond on the WBPR, circa 1900 (Maine Historical Society, 2011).

Figure 8. A photo of Little Lyford Pond on the WBPR, circa 1900. Note the landslide scar on the hillslope in the background (Maine Historical Society, 2011).

Figure 9. A photo of Lower Little Lyford Pond on the WBPR, circa 1900 (Maine Historical Society, 2011).

Figure 10. A photo of the kilns at the Katahdin Ironworks site below Silver Lake on the WBPR, circa 1890 (Maine Geological Society, 2005)

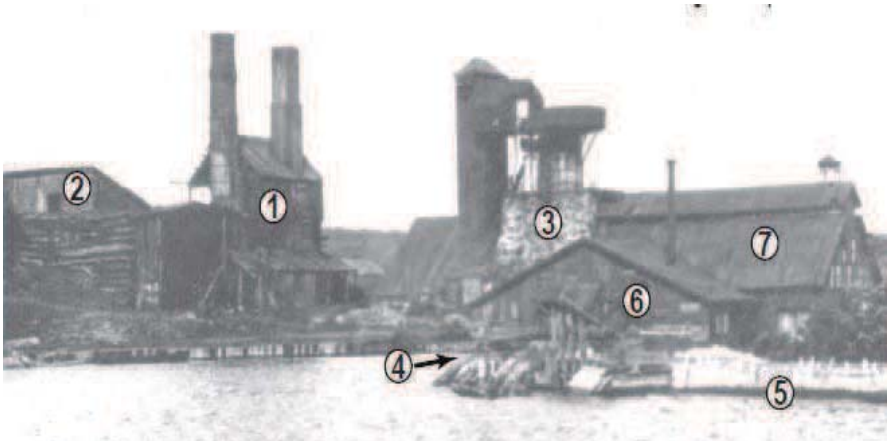

While ore was roasted in the Iron Kiln(1) workers filled the Charcoal Storage Shed(2) with charcoal from the brick kilns. The charcoal, ore, and limestone were dumped into the Furnace(3) and then superheated by pumped-in air. A Sluiceway(4) diverted water from the Dam(5) through the Machine House(6) where it powered cylinders that forced the air into the furnace. The melted iron then ran out into sand molds on the floor of the Casting House(7) where the pigs were formed.

Figure 11. A photo of the site of the former iron works facilities at the outlet of Silver Lake, circa 1890. (Maine Department of Conservation, 2011).

SILVER LAKE HOTEL,

KATAHDIN IRON WORKS, MAINE.

ABSOLUTELY THE HEALTHIEST SPOT IN MAINE.

SITUATED in the heart of the big game region, near the very best Trout fishing and good camps. The famous

MINERAL SPRING

is close by the hotel. Invalids and people seeking rest invariably find the mountain and iron air most beneficial, while hay fever is unknown here.

House has recently been put in good repair. All rooms with a good view. Bath rooms have hot and cold water. First-class table. For moderate terms, address

Proprietor SILVER LAKE HOTEL,

KATAHDIN IRON WORKS, ME.

Figure 12. An early 20th century advertisement for the Silver Lake hotel, located near the dammed outlet of Silver Lake on the WBPR (Bangor & Aroostook, 1905)

Figure 13. A photo of the WBPR downstream of Silver Lake, near the former site of Katahdin Ironworks (Bangor & Aroostook, 1902).

1.3 Geologic and glacial history

1.3.1 Bedrock geology

The geology of the WBPR watershed is composed of Devonian-Silurian metasedimentary and Devonian intrusive rocks (Thompson and Borns, 1985). The Gulf Hagas gorge is a prominent feature in the watershed, and is located where the WBPR flows over the vertically-dipping mudstone beds of the Carrabasset Formation (Johnston, 2009). The underlying geology of the Narraguagus watershed consists of Paleozoic metamorphic rocks and Devonian granites, and the Sheepscot watershed is made of primarily Paleozoic metasedimentary rocks.

1.3.2 Glacial history

Maine underwent repeated episodes of continental glaciation during the Pleistocene, and this glacial legacy is evident in the surficial geology of the watersheds, which is made up primarily of glacial till, bedrock and, in the Narraguagus and Sheepscot watersheds, glaciomarine deposits (Thompson and Borns, 1985). The Laurentide ice sheet retreated north to the current Maine coastline by 14 ka, but the crust remained isostatically depressed by the weight of the ice (Schnitker et al., 2001). This lowered elevation relative to sea level resulted in marine transgression across much of coastal Maine, and the accompanying deposition of glaciomarine sands and gravels between the glacial front and the ocean (Belknap et al., 1987; Barnhardt et al., 1995). The WBPR watershed was inland during the late Pleistocene, but the other two watersheds were submerged during this epoch: the Narraguagus River was partially inundated, while the Sheepscot River was almost completely inundated (Figure 1). Post-glacial isostatic

adjustment of the crust continues to play an important role in the evolution of the landscape and drainage networks in Maine.

1.3.3 Channel profiles

The WBPR is considerably steeper (average gradient 0.0074) than either the Narraguagus (average gradient 0.0015) or Sheepscot (average gradient 0.0026) rivers, but all three rivers are broken up into alternating steep (gradient >0.002) and flat (gradient <0.0005) sections (Figure 2). The bed material in the fast-flowing steep sections is composed primarily of coarse sand, gravel, and cobbles, while the relatively flat and slow-moving sections (including natural and artificial lakes, ponds, and marshes) are sand- and mud- bedded (Wilkins and Snyder, 2011). The WBPR watershed has a greater total relief (1030 m) than either of the coastal watersheds (451 m for the Narraguagus, 337 m for the Sheepscot; Figure 1).

1.4 Atlantic salmon habitat

In recent centuries, anthropogenic modification of Maine river systems has obscured the state of the watersheds prior to European settlement. Timber harvest and log drives have had a major impact on the river systems through the removal of in-channel boulder and LWD obstructions and channel straightening (Magilligan et al., 2008). These changes have potentially resulted in wider and shallower channels with decreased bank stability in comparison to undisturbed environments (Montgomery, 2003; NRC, 2004). Geomorphic factors such as sediment supply, bed sediment mobilization, substrate embeddedness and channel complexity play important roles in supporting ecological

systems (Montgomery et al., 1999; Piegay et al., 2000; Buffington et al., 2004). As a result, a movement towards restoration of many of these watersheds has been prompted by ecological concerns related to habitat loss and degradation, particularly since the listing of the anadromous[2] Maine Atlantic salmon (*Salmo salar*) as an endangered population (Lisles, 2000; NRC, 2004). The Narraguagus and Sheepscot rivers are classified respectively as critical habitat for the Downeast Coastal and Merrymeeting Bay Salmon Habitat Recovery Units (SHRUs) of the Gulf of Maine Distinct Population Segment (GOM DPS) of Atlantic salmon. Despite low numbers of returning fish these rivers still host populations viable enough to warrant restoration efforts (Arter, 2003; Fay et al., 2006; NOAA, 2017; Wilkins and Snyder, 2011). The WBPR does not flow directly into the Atlantic Ocean, but it falls within the watershed of the coastal Penobscot River, and is also designated as critical habitat for the Penobscot Basin DPS.

Atlantic salmon form redds and spawn in late autumn in low order upstream reaches of coastal rivers in New England, Atlantic Canada and northern Europe. Juvenile Atlantic salmon spend the first 2-4 years of their lives in freshwater (where they are recognized in subsequent developmental stages as alevin, fry and parr) before migrating to the northern Atlantic Ocean as smolts. The fish typically spend several years in the ocean before returning to their home rivers to spawn as mature, 4-7 kg fish (MDFW, 2007). Unlike most other species of salmon, Atlantic salmon often return to the ocean after spawning.

[2] Species that spend most of their lives in the oceans and migrate upriver to spawn.

Upon return to freshwater, a number of factors must be met to enable spawning success and subsequent juvenile survival, including sufficient habitat complexity (deep pools, in-channel debris, bank vegetation), mobile gravel bed sediment, and cool water temperatures in summer (NRC, 2004). Thus, geology and local geomorphic processes control ideal spawning habitat (Montgomery, 2004). Coarse and easily mobilized gravel bed sediments are necessary for construction of redds by salmon and ensures that eggs receive a steady supply of oxygen. The degree of embeddedness[3] of the channel substrate is important in this respect, as immobile sediment restricts both the ability of salmon to construct redds and the delivery of nutrients to eggs. Similarly, channel armoring caused by a lack of sediment supply is critical to the ability of salmon to successfully spawn. Too much fine sediment in a stream also hinders salmon spawning and rearing by cutting off oxygen supply to redds, regardless of embeddedness or armoring.

In addition, salmon require a clear migratory route from the ocean to spawning grounds. Several run-of-the-river dams impede migration routes on the Narraguagus and Sheepscot rivers, while the WBPR has numerous dams between it and the Penobscot River estuary. Ongoing channel barrier removal and the construction of fish passage around dams could potentially open up a broad range of historic anadromous species habitat, particularly on the WBPR (NRC, 2004; Penobscot River Restoration Trust, 2010).

[3] The degree to which fine-grain sediments surround coarse bed material.

1.5 Purpose of study

The main objectives of this study are to:

1) understand how bedrock controls on the longitudinal profile and sediment inputs impact substrate grain size and channel morphology in the West Branch of the Pleasant River (WBPR);

2) apply a model predicting substrate grain size based on digital elevation model (DEM)-derived geometric channel parameters;

3) compare the model results from the high-gradient WBPR to previously studied low-gradient coastal Maine rivers; and

4) explore the implications of my findings on channel and habitat restoration in paraglacial rivers.

To do this, I use DEM-derived data to predict substrate grain size using a simple semi-empirical grain-size prediction model tested on low-gradient coastal rivers in Maine by Wilkins and Snyder (2011):

$$D_{50} = \frac{\tau_b}{(\rho_s - \rho) g \tau_*}, \text{ (Equation 1)}$$

with model parameters defined in Table 1.

Parameter	Definition
n	Manning roughness coefficient (assumed to be 0.03, 0.04 or 0.06, as noted)
ρ	Density of water (1000 kg/m^3)
ρ_s	Density of sediment (assumed to be 2650 kg/m^3)
k_q	Coefficient of discharge-drainage area relationship, I calculate for RI=2 years
c	Exponent of discharge-drainage area relationship (assumed to be 1)
w_a	Field-measured active channel width (m)
w_{hf}	Field-measured high-flow channel width (m)
w_{lidar}	Lidar-derived channel width (m)
h_a	Field-measured active channel depth (m)
h_{hf}	Field-measured high-flow channel depth (m)
S_{lidar}	Lidar-derived channel gradient
A	Drainage area, calculated from 10-m DEMs (m^2)
$\tau_{b\ pred}$	Bed shear stress calculated using Eq. 2 and 3, w_{lidar}, and S_{lidar} (Pa), Eq. 5
$\tau_{b\ pred(w_{hf})}$	Bed shear stress calculated using Eq. 2 and 3, w_{hf}, and S_{lidar} (Pa), Eq. 7
τ_*	Shields parameter assumed to be 0.04 (Snyder et al., 2008), Eq. 6
$D_{50\ field}$	Median grain size measured in the field (mm)
$D_{50\ pred}$	Median grain size calculated using τ_*=0.04 and $\tau_{b\ pred}$ (mm), Eq. 1
Q	Channel discharge, approximated by A and k_q (m^{3}s^{-1}), Eq. 4

Table 1. Definition of field- and DEM-derived parameters.

1.6 Prior research

The Buffington et al. (2004) and Wilkins and Snyder (2011) papers establish the scientific basis for this approach. Both studies focus on predicting salmon habitat availability using DEMs and field measurements; Buffington et al. (2004) in mountain rivers in the Pacific Northwest and Wilkins and Snyder (2011) in lower gradient coastal rivers in Atlantic Maine and Canada. Buffington et al. (2004) incorporate variations in hydraulic roughness (*n*) and channel types (step-pool, pool-riffle, wood-forced pool-riffle, step-pool, cascade) for high gradient drainage basins. Wilkins and Snyder (2011) do not incorporate the variations in channel type and hydraulic roughness that Buffington et al. (2004) explore, but the advantages of their model are the relative simplicity of the analysis, the geographical and geological similarity of the study locations with mine, and that the model is applicable to entire rivers and does not require resource-intensive field data collection. Wilkins and Snyder (2011) apply the model to coastal low gradient rivers using DEM data, whereas I apply it to a high gradient river and compare the two types of systems. Their results show that the model tends to overpredict substrate grain size for channel reaches with low grain size. I use an expanded dataset to examine this problem, and include data from the higher-gradient West Branch of the Pleasant River (WBPR) as well as coastal rivers.

This study uses DEM and field measurements to predict channel substrate characteristics, and a number of previous papers have explored similar approaches. Carbonneau et al. (2004) used low-altitude aerial photographs of streambeds to predict and map bed grain size, and Carbonneau et al. (2005) used image processing of aerial

photographs to estimate bed grain size. These studies use datasets that are limited in their coverage, and are not as readily or easily applied as the approach used in this analysis, which relies on 10 m and lidar DEMs. Donaldson and Sklar (2010) and Donaldson et al. (2009) used 10 m and lidar DEM-based data similar to that of Wilkins and Snyder (2011) to predict channel type. Other remote-sensing studies focusing on the relationship between channel type and habitat include: Legleiter et al. (2004), who evaluated methods of remotely measuring stream depth and quantifying in-channel habitat; Hedger et al. (2006), who explored the linkage between variation in substrate size and juvenile Atlantic salmon using remote sensing; and Fonstad and Marcus (2005), who developed a method to remotely predict stream depths from aerial images. In addition to these studies, Neeson et al. (2007) used GIS-derived geomorphic variables to predict spawning habitat for anadromous lamprey in the Great Lakes and Kim and LaPointe (2010) studied the relationship between the relative size of Atlantic salmon runs and spatial distribution of favorable habitat in 14 watersheds in the Gaspé Peninsula of Quebec, a region with a glacial history similar to Maine.

This study is part of a larger research effort on paraglacial[4] coastal rivers in Maine. A number of Boston College graduate students have worked in the Sheepscot and Narraguagus rivers, and these studies provide the opportunity for comparison of bedload mobilization and channel morphology among different types of rivers (Castele, 2007; Snyder et al., 2008; Wilkins and Snyder, 2011; Strouse, in progress). Prior studies have determined that glacial history and channel gradient are primary controls on bed grain

[4] Defined as a transitional landscape, "adjusted neither to [the] Last Glacial Maximum nor to contemporary geomorphic processes" (Slaymaker, 2009).

size in lower-gradient rivers partially inundated by the Pleistocene sea level highstand (Wilkins and Snyder, 2011).

2. MODEL

2.1 Background

River channels are typically classified by both morphology and ability to transport sediment. Morphological classifications of channel types fall within three broad categories: colluvial, bedrock and alluvial (Montgomery and Buffington, 1997). Colluvial channels are headwater reaches dominated by mass wasting, and are not relevant to the parts of the WBPR studied here. Bedrock channels have sediment transport rate limited by the amount of sediment supplied to the channel (supply-limited), as opposed to channels where the morphology adjusts so that transport rate matches the sediment load delivered from upstream (Montgomery and Buffington, 1997). Alluvial channels are defined by the presence of transportable substrate sediments (alluvium), and thus a wide range of channel types can be classified as alluvial. These channels are either transitional between supply- and transport-limited or strictly limited by their transport capacity of the channel (Montgomery and Buffington, 1998). These categories are not static: long-term (e.g., due to climate change) or seasonal increases in sediment supply and decreases in discharge can lead to the transition of bedrock channels to alluvial channels, and decreases in sediment supply and increases in discharge can shift alluvial channels to bedrock channels (Howard, 1987).

Channels are also categorized by whether they have mobile or immobile bed and banks. Alluvial channels are self-formed, in that the river itself deposits the bed and bank material. Self-formed channels adjust their gradient (S), channel geometry (w, h) and bed roughness (n) to accommodate changes in sediment supply and discharge, and actively rework their banks and floodplains. The dominant channel-forming discharge event in alluvial channels is often referred to as the bankfull flow, and it has a recurrence interval of 1-2 years (Wolman and Miller, 1960). Bedrock channels are imposed-form, meaning that the channel path is set by non-fluvial factors (such as glacial or tectonic history). Bedrock channels typically have relatively sparse in-channel deposits of alluvium (e.g., bars), have immobile banks, and channel gradient and geometry are dependent on the underlying bedrock.

The term "threshold channel" refers to an alluvial gravel-bedded river in which the boundary shear stress in the channel at bankfull flow is only marginally greater than the threshold shear stress required to entrain the bed material (Parker, 1979; Andrews, 1983; Lisle et al., 2000). Threshold channels can have a single dominant channel (single-threaded) or multiple channel (multi-threaded) morphology. Bedrock channels are typically single-threaded and lack in-channel depositional bars, but alluvial channels can be either single- or multi-threaded depending on factors such as slope, vegetation and sediment supply (Lisle et al., 2000). Single-threaded alluvial channels often have alternating bars along the channel, while multi-threaded alluvial channels have more extensive depositional features including mid-channel bars and islands.

The bedload in threshold channels remains immobile at most flows; the transport rate is relatively low and the banks are resistant to erosion (Andrews, 1983). In this case the bed sediment is primarily composed of lag deposits, which are immobile artifacts of past high flow transport conditions. The concept of a threshold channel is important for this analysis, as I approximate discharge using a recurrence interval of 2 years (bankfull flow; Table 1; Equation 4) and so I assume that the median grain size (D_{50}) is entrained by the bankfull flow. As a result grain size predictions based on this approach are only applicable in single-thread threshold channels, in which the bedload is mobilized only at high flow. Grain size predictions are not applicable for sand-bed or finer channels, in which the coarsest bed sediments are entrained at lower flows.

Channel geometry can be defined by measurements of parameters such as width, depth and slope (w, h and S; Leopold and Maddock, 1953). These parameters, along with median grain size ($D_{50\ field}$), are primarily set by discharge events with a recurrence interval of 1-2 years and the amount of sediment supplied to the channel (Wolman and Miller, 1960). At a reach-scale, S also adjusts to variations in sediment supply by erosion and deposition and/or changes in sinuosity (via channel cutoffs). The presence of glacial ponds and lakes alternating with steep bedrock sections provides evidence that S on the three study rivers is largely set by glacial erosion and underlying bedrock of the paraglacial landscapes (Figures 1-2). Any change in S on these rivers takes place over a timescale several orders of magnitude larger compared with changes in width and depth (Parker et al., 2007).

2.2 Model setup

Similar to Wilkins and Snyder (2011), I use digital elevation model (DEM)-derived parameters to predict grain size in paraglacial rivers in Maine. The objective of this approach is to use a model that can be remotely applied along the length of a river, without using field-measured parameters. The model inputs include simple geometric channel parameters (S, w) and drainage area (A) measured from remote sensing and geographic information systems (GIS) data. I use these parameters to predict substrate grain size by estimating high-flow shear stress at points along the river longitudinal profiles. Channel slope (S) and depth (h) allow for an estimate of bed shear stress (τ_b), which is the resisting force of the bed to the downstream force of the flow (assuming a steady, uniform flow):

$$\tau_b = \rho g h S, \text{ (Equation 2)}$$

where ρ is the density of water (1000 kg/m^3) and g is gravitational acceleration at the Earth's surface. A limitation in applying this equation is that it is not possible to measure h using DEM data. This problem is circumvented by substituting the Manning friction relationship and an equation for the conservation of mass for water ($Q=uwh$; assuming rectangular channel cross sections) into Equation 2. This gives τ_b as a function of w, Q, and n: (e.g., Snyder et al., 2003):

$$\tau_b = \rho g n^{3/5} \left[\frac{Q}{w}\right]^{3/5} S^{7/10}, \text{ (Equation 3)}$$

where n is the coefficient of channel roughness, Q is discharge, and w is the width of the channel. Q is difficult to measure directly along stream longitudinal profiles, and as a result I approximate Q using drainage area (A), which is derived from spatial analysis of 10-m DEMs using standard ArcGIS methods. Q has a power-law relationship with A:

$$Q = k_q A^c \text{ , (Equation 4)}$$

where k_q is an empirical coefficient associated with a given flood recurrence interval (RI) and c is a constant (assumed to be 1) dependent on the fraction of the watershed contributing flow to the channel during the flow event in question (Dunne and Leopold, 1978). I then substitute this relationship into Equation 3 to calculate τ_b in terms of A:

$$\tau_b = \rho g n^{3/5} \left[\frac{k_q A^c}{w}\right]^{3/5} S^{7/10}. \text{ (Equation 5)}$$

The Shields parameter (τ_*) is a dimensionless ratio of downstream bedload entraining forces (τ_b) to the submerged weight of the bed sediment. This parameter enables an estimate of stream competence, or maximum particle size entrained by the flow, using the values for τ_b:

$$\tau_* = \frac{\tau_b}{(\rho_s - \rho) g D} \text{ , (Equation 6)}$$

where D is the grain diameter (or the median grain size at a cross section), ρ_s is the density of the particle (ρ_s =2650 kg/m^3, which is the density of quartz and feldspar). Bedload mobilization typically corresponds to a τ_* range of 0.03-0.07 (Buffington and Montgomery, 1997), and Snyder et al. (2008) found mobile beds for values of $\tau_* \geq 0.04$ on the Sheepscot and Narraguagus rivers. The model for predicting median grain size (Equation 1, reproduced below) rearranges the Shields equation to solve for D_{50}:

$$D_{50} = \frac{\tau_b}{(\rho_s - \rho) g \tau_*},$$

where I calculate τ_b using Equation 5.

2.3 Model assumptions and hypotheses

I use a simple modeling approach to predict grain size, in which I estimate four of the parameters and hold them constant: (1) n; (2) τ_*; (3) k_q; and (4) c. I calculate τ_b with constant roughness (n=0.04) at every point along the channel, which may not reflect the local variability in roughness. Unlike Wilkins and Snyder (2011), Buffington and Montgomery (2004) take local variations in roughness along the channel profile into account. For comparison, I explore the sensitivity of my results to variations in n. The Shields parameter is held constant (τ_*=0.04) for predicting grain size, consistent with Wilkins and Snyder (2011). I assume that D_{50} is entrained at high flows on the order of 2 years, and thus grain size predictions based on this approach are only applicable in threshold channels in which the bedload is mobilized at high flow. I calculate k_q for a recurrence interval of 2 years, which is within the 1.5-2 year range for primary channel-forming events (Wolman and Miller, 1960; Mount, 1995; Lisle et al., 2000).

Based on these assumptions, I hypothesize that for supply-limited (low bedload supply) threshold reaches with S set by glacial history and bedrock geology, bed grain size should depend on local hydraulics (set by Q, S, h and w) and the model should be most successful. This corresponds to reaches where bed sediment is primarily composed of lag deposits that are only transported during floods. My second hypothesis is that transport-limited (high sediment supply) non-threshold reaches should have bed

sediments that depend on the grain size of the material being supplied, local hydraulics and the time interval since last high flow event. The model may or may not work in these reaches, which are likely characterized by gravel bars or islands and a wider range of grain sizes. This hypothesis points to the influence of sediment inputs (e.g., the White Brook tributary downstream of Gulf Hagas, at river kilometer 26.4, Figure 2c) as sediment sources for the river and important controls on bedload grain size and transport frequency.

I test these hypotheses by examining variations in the ratios of predicted to field-measured median grain size ($D_{50\ field}$, $D_{50\ pred}$) and bed shear stress ($\tau_{b\ field}$, $\tau_{b\ pred}$) along the channel profile, as well as exploring channel geometry and morphology including S, w and h (discussed in Methods). As hypothesized, this prediction method should work best in single-thread, alluvial gravel bed rivers with low sediment supply relative to transport capacity. Building on Leopold and Maddock (1953) and the concept of a bankfull[5] channel geometry, Parker et al. (2007) determined quasi-universal bankfull hydraulic relationships for threshold channels. Calculating high-flow width and depth (w_{hf}, h_{hf}) and S as functions of Q and $D_{50\ field}$ for the WBPR and comparing the results to the Parker et al. (2007) dataset provides an additional means of evaluating whether the WBPR behaves like a classic threshold (single-thread, alluvial gravel bed) channel. The Wilkins and

[5] I use the "high-flow" designation (w_{hf} and h_{hf}; defined largely by changes in bank vegetation) rather than "bankfull," which assumes an alluvial channel morphology (channel with floodplain). However, Parker et al. (2007) use the "bankfull" designation in their equations, and so for the purpose of comparison I use "high-flow" to approximate "bankfull" (see section 3.2.2).

Snyder (2011) prediction method is designed for threshold channels, and would not be expected to work as well if the necessary criteria are not met.

3. METHODS

3.1 GIS measurements

Digital elevation models (DEMs) are a useful tool for remotely measuring the channel characteristics and morphology of river systems (e.g., Snyder et al., 2000). I used DEMs to make measurements of drainage area (A), channel width (w) and gradient (S). I then used these variables to calculate τ_b (Equation 5) and predict D_{50} (Equation 1).

DEMs are commonly derived from digitized topographic maps. However, making measurements from these DEMs has several limitations. The low resolution (typically 10 meters per pixel) means that measurements are less accurate for channel-scale parameters (such as w and S) than watershed-scale parameters (A; Snyder, 2009). 10 m DEMs provide an accurate portrayal of watershed boundaries and drainage patterns, are so are used to calculate A in ArcGIS using a flow accumulation algorithm.

Light detection and ranging (or lidar), a technology used in airborne laser swath mapping (ALSM) of topography, provides a means by which to obtain up to a one hundred-times finer-resolution measurements of the same features (Snyder, 2009). Lidar surveys yield DEMs from direct aerial laser measurements of the surface of the earth rather than being derived from a secondary source (topographic maps). Lidar DEMs have a horizontal (pixel) resolution of ~1 meter, which is smaller than typical channel widths.

I use lidar data to measure channel width (w), elevation and slope (S) of the study rivers. I first measure width (w_{lidar}) at every 100 m along the river by drawing and measuring lines from bank to bank across the active channel perpendicular to the centerline on a lidar-derived shaded-relief image at a scale of 1:2,500 (Wilkins and

Snyder, 2011). I used the lidar DEM to calculate slope (S_{lidar}) by tracing the channel path on a lidar-derived shaded relief image and extracting elevation values from the channel centerline, which I then smoothed using a 25-point moving average filter. In order to calculate S_{lidar} over a range of elevation change greater than the peaks in the profile elevation related to the original DEM gridding process or sampling of banks or floodplains, I connect the minima along the channel profile. I then interpolate elevations at 0.5 m spacing along the profile and calculate S_{lidar} value for each 100 m station (Figure 2a-c; Snyder, 2009; Wilkins and Snyder, 2011).

3.2 Field data collection

3.2.1 Basic information

I use field measurements of channel characteristics to test the accuracy of DEM-based measurements and predictions. Primary field data are gathered from reach-scale channel measurements at global positioning system (GPS)-referenced stations every 100 m along the longitudinal profile of the channels (Figures 1-3). Fieldwork in the summer of 2009 on the West Branch of the Pleasant River focused on identifying channel access points and preliminary survey work on the upper reaches of the river. Standard field measurements include active and high-flow channel width and depth (w_a, w_{hf}, h_a, h_{hf}) surveys and Wolman method point counts (Wolman, 1954). In 2009 I collected data beginning at the outlet of First Roach Pond at river kilometer (rkm, measured upstream from the confluence with the mainstem Pleasant River) 51.7 and downstream to rkm 49.1. The field season in the summer of 2010 focused on collecting

data from both the upper (rkm 38.4-34.0) and lower (downstream of Gulf Hagas at rkm 31.2-10.6, Figures 2c and 3; Table 2) parts of the river in order to investigate changes in channel morphology above and below the gorge. Field measurements from the Narraguagus River come from fieldwork done as part of a prior Master's thesis at Boston College (Wilkins, 2009; Figures 1 and 2a). Data from the Sheepscot River were collected as part of various Boston College student projects between 2006 and 2010 (Hazlinsky, in progress; Strouse, in progress; Figures 1 and 2b).

River	Date collected	Total length surveyed	Pebblecounts
WBPR	2009 2010	20.8 km	91
Narraguagus	2007 2008	23.9 km (+17.9 partial)	116
Sheepscot	2006 2009 2010	7.0 km in mainstem (+11.0 km partial), 8.3 km in West Branch	69

Table 2. Field survey data for the three rivers**.**

3.2.2 Width and depth measurements

Field measurements of active and high flow channel width and depth involve cross-sectional channel surveying of active width (w_a), high-flow width (w_{hf}), active depth (h_a) and high-flow depth (h_{hf}) with a Laser Tech 200 LR laser range finder. Measurements are taken by one person standing in the channel thalweg and sighting a survey rod held on each bank. The water surface at the banks serves as the reference for w_a, while w_{hf} is defined by the transition from aquatic to riparian vegetation on the bank

profile (Leopold, 1994; Snyder et al., 2008). I use "high-flow" parameters rather than self-formed "bankfull" parameters, both because field measurements are made independent of stage and a bankfull designation assumes a self-formed channel (Wilkins and Snyder, 2011). Measurements of channel width and depth (w, h) are only made at channel cross sections where it is shallow enough to stand in the thalweg and we are still able to operate the laser rangefinder at eye level. This requirement limits the length of several of the study segments (Figure 1). The width to depth ratio (w/h) is also calculated for every channel cross section, as they are frequently used as non-dimensional indicators of channel geometry (Knighton, 1998). Definitions of field and DEM-derived parameters are listed in Table 1.

3.2.3 Grain size measurements

I conducted cross-sectional grain-size point counts of at least 100 clasts every 200 meters using the Wolman method (Wolman, 1954) to determine median (D_{50}) and coarse-fraction (D_{84}) grain size at a given channel cross-section. I processed pebble count data in Matlab to produce plots of grain size distribution for the sampled locations, and I use the calculations of $D_{50\ field}$ and $D_{84\ field}$ to evaluate downstream trends in sediment over the length of the rivers (Appendix). I compare these results with the calculated predictions of grain size ($D_{50\ pred}$; Equation 1).

4. RESULTS AND INTERPRETATIONS

4.1 Channel descriptions and segments

Due to the changes in channel characteristics along the length of the West Branch of the Pleasant River (WBPR) through the study area, I divide the surveyed channel into 5 segments based on changes in the longitudinal profile and sediment supply: downstream of Branch Pond (DSBP), upstream of Gulf Hagas (USGH), Gulf Hagas to White Brook (GHWB), White Brook to Silver Lake (WBSL) and downstream of Silver Lake (DSSL; Figures 2c and 3; Table 3). The upper surveyed segment of the WBPR (DSBP) is a narrow single-thread stream with relatively homogenous substrate grain size compared to downstream reaches of the channel. The immediate drainage basin is heavily wooded, and the banks are thickly vegetated (Figures 14-15). Downstream of rkm 49.1 (USGH segment, Figure 16) the channel is occasionally diverted by beaver activity and large woody debris (LWD), and it transitions to a lower-gradient section dominated by ponds and lakes. The base level of the channel upstream of rkm 34.2 is set by bedrock ledges at the upstream boundary of Gulf Hagas, a high-gradient bedrock gorge that extends from rkm 34.2-30.0 (Figures 2c, 4-6 and 17-19; Table 3). The GHWB segment is single-threaded, and the WBPR transitions from the bedrock of Gulf Hagas to an alluvial gravel-bedded channel. In the GHWB segment the influence of past logging in the watershed is apparent, particularly around rkm 27.5, where cut logs and other debris are actively eroding out of gravel in the banks (Figure 20). The White Brook tributary enters the channel on river left (north) at rkm 26.4 and marks the upstream boundary of the WBSL survey segment. The White Brook alluvial fan chokes the WBPR channel with

gravel, and downstream in-channel bars become common. By rkm 25.6 the channel is mostly multi-threaded, with evidence of active channel migration in numerous abandoned side channels (Figure 21). The channel becomes increasingly sand-bedded downstream, with patchy gravel substrate in some reaches. This channel segment is more transport-limited, self-formed and depositional relative to the other segments, and LWD is common in the channel (Figure 22) as it becomes progressively lower-gradient leading into Silver Lake, a shallow marsh-fringed lake at the site of the former Katahdin Iron Works (KI) facility (Figures 2c and 23-24). The downstream outlet of the lake is controlled at rkm 14.8 by an in-channel, 70 m-wide remnant boulder dam originally used to power the bellows of the KI iron smelting furnaces (Figures 11 and 24). Downstream of Silver Lake to rkm 10.5 (DSSL) the channel is largely single-thread, and boulders and bedrock chutes are prevalent (Figure 25).

Several qualitative inferences relating to sediment supply can be drawn from field observations and the channel longitudinal profile: WBSL has the highest sediment supply (due to the influence of the tributary fan at rkm 26.4) and exhibits the smallest $D_{50\ field}$ and S_{lidar} means and least range in S_{lidar} (Table 3). The segments downstream of lakes (DSBP and DSSL) have the least sediment supplied to the channel, and GHWB and USGH are intermediate between these two end members. DSSL provides the best example of an imposed-form segment, with notable bedrock-dominated channel sections, a relative lack of finer sediment and a large $D_{50\ field}$ mean and standard deviation (Table 3).

Segment name	A range(m^2)	$D_{50\ field}$ range (mm)	$D_{50\ field}$ mean, std dev (mm)	S_{lidar} range	S_{lidar}	w_{hf}/h_{hf}	h_{hf} (m)	w_{hf}(m)	Length (rkm)
DSBP	19072700-24841400	326-75	69±26	0.0429-0.0042	0.0149± 0.0107	12.1±2.6	0.71±0.09	8.6±1.8	51.7 – 49.2
USGH	88255500-107959500	132-2	59±43	0.0148-0.0008	0.0038± 0.0034	20.2±8.7	0.81±0.36	14.4±4.6	38.4 – 34.2
GHWB	112623900-216371700	206-14	90±63	0.0985-0.0007	0.0097± 0.0149	21.7±12.0	1.01±0.33	19.5±5.9	31.2 – 26.4
WBSL	216730000-230739900	86-5	33±22	0.0073-0.0005	0.0018± 0.0155	21.6±10.0	0.90±0.34	17.3±5.8	26.3 – 19.3
DSSL	306107300-315517800	283-75	159±57	0.0160-0.0021	0.0069± 0.0040	33.0±19.2	0.99±0.38	28.2±10.0	14.8 – 10.5
Combined	19072700-315517800	326-2	82±64	0.0985-0.0005	0.0078± 0.0134	0.90±0.34	0.90±0.34	18.5±8.8	20.8 km

Table 3. Statistics and range of parameters for WBPR surveyed channel segments.

Figure 14. The view upstream at the outlet of Roach Pond on the WBPR, below rkm 51.7 (7/28/2009).

Figure 15. The view downstream from First West Branch Pond on the WBPR at rkm 51.6 (NPS 7/29/2010).

Figure 16. The view downstream from rkm 36.4 in the USGH segment of the WBPR (NPS 7/27/2009).

Figure 17. The view upstream from Billings' Falls in Gulf Hagas on the WBPR (7/27/2009).

Figure 18. The view downstream at rkm 31.2 on the WBPR at the downstream end of Gulf Hagas (8/4/2010).

Figure 19. The view downstream from rkm 31.2 on the WBPR in the GHWB segment (8/4/2010).

Figure 20. The view upstream from rkm 27.6 on the WBPR, showing buried logging debris eroding from the river right bank (NPS 7/28/2010).

Figure 21. The view upstream from rkm 25.6 on the WBPR, showing the actively migrating channel above Silver Lake (8/1/2010).

Figure 22. The view downstream from rkm 17.0 on the WBPR showing the LWD-obstructed and sand-bedded segment upstream of Silver Lake (8/2/2010).

Figure 23. The view across Silver Lake (rkm 19.3-14.8) on the WBPR (8/2/2010).

Figure 24. The view upstream from rkm 14.8, at the outlet of Silver Lake on the WBPR (NPS 7/29/2010).

Figure 25. The view upstream from rkm 10.6 in the DSSL segment of the WBPR (8/3/2010).

4.2 Field and GIS measurements

4.2.1 Channel width and depth

Active and high-flow channel width (w_a, w_{hf}) and depth (h_a, h_{hf}) measurements come from field surveys. The variability of w_a and w_{hf} increases downstream with increasing drainage area (A), whereas both h_a and h_{hf} have a similar pattern of magnitude distribution along the channel profile (Figure 26).

Unlike lidar width measurements (w_{lidar}), channel depth (h) cannot be determined from the lidar dataset, and so measurements of depth come solely from field surveys of h_a and h_{hf} (Table 3). As a result, I only compare lidar and field w measurements. Wilkins and Snyder (2011) found that GIS measurements of width best match w_a on the Narraguagus River, but I focus on w_{hf} for comparison. w_{lidar} measurements match w_{hf} measurements better than w_a on the WBPR, particularly in the more bedrock-dominated, supply-limited channel segments (such as DSSL) that make up a significant portion of the surveyed points (Table 3). Despite the high resolution of the lidar DEM, only 71% of w_{lidar} fall within a factor of ±1.5 of the w_{hf} measurements (Figure 27). This discrepancy between w_{lidar} and w_{hf} includes both overestimations and underestimations of channel width. The majority of the scatter in Figure 27 represents wider w_{lidar} measurements than w_{hf} measurements (31 overestimations against 24 underestimations), while of those overestimations 52% are greater than a factor of +2. In comparison, only 25% of the w_{lidar} measurements are narrower than w_{hf} by more than a factor of 1/2. I explore these results further in section 5.1 below.

For the WBPR, width-to-depth ratio (w_{hf}/h_{hf}) displays a general increasing trend and the range is considerably greater in the middle and downstream surveyed channel reaches. It appears at first glance that the mean w_{hf}/h_{hf} for the WBPR is the similar to the Narraguagus and Sheepscot rivers (Figure 28). However, a z-test for means shows that the null hypothesis that the mean w_{hf}/h_{hf} for the WBPR is the same as the Narraguagus and Sheepscot rivers can be rejected at a significance level of α=0.05. The WBPR distribution most closely resembles the Narraguagus River with respect to ratio magnitude, and the Sheepscot River with respect to shape of the distributions (Figure 28; Table 4).

Parameter:	**WBPR**	**Narraguagus**	**Sheepscot**
Active width (w_a) (m)	15.61±8.71	18.47 ± 8.52	13.44±8.38
High-flow width (w_{hf}) (m)	18.50±8.77	26.48 ± 17.57	17.57±11.03
Active depth (h_a) (m)	0.54±0.29	0.80 ± 0.44	0.48±0.27
High-flow depth (h_{hf}) (m)	0.90±0.34	1.34 ± 0.48	1.02±0.42
Width to depth ratio (w_{hf}/h_{hf})	22.60±13.62	21.24 ± 13.47	18.55±9.02

Table 4. Average and standard deviation for field measurements of channel width and depth.

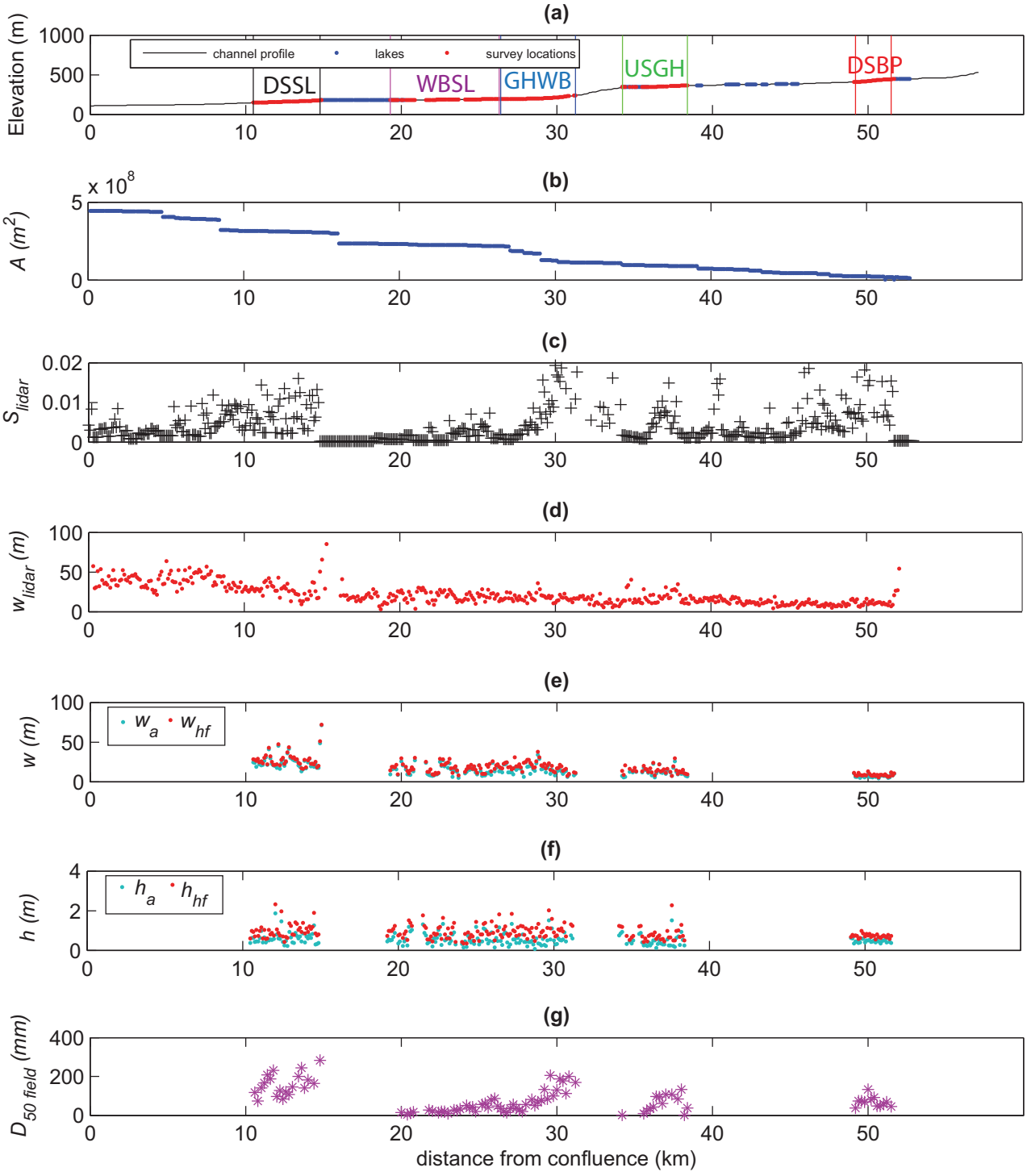

Figure 26 (a-g). GIS-measured elevation, drainage area (A), slope (S), and channel width (w_{lidar}) for the WBPR are shown in panels a-c. Field-measured high-flow and active channel width (w_{hf}, w_a), high-flow and active depth (h_{hf}, h_a) and median grain size ($D_{50\ field}$) are shown in panels e-g.

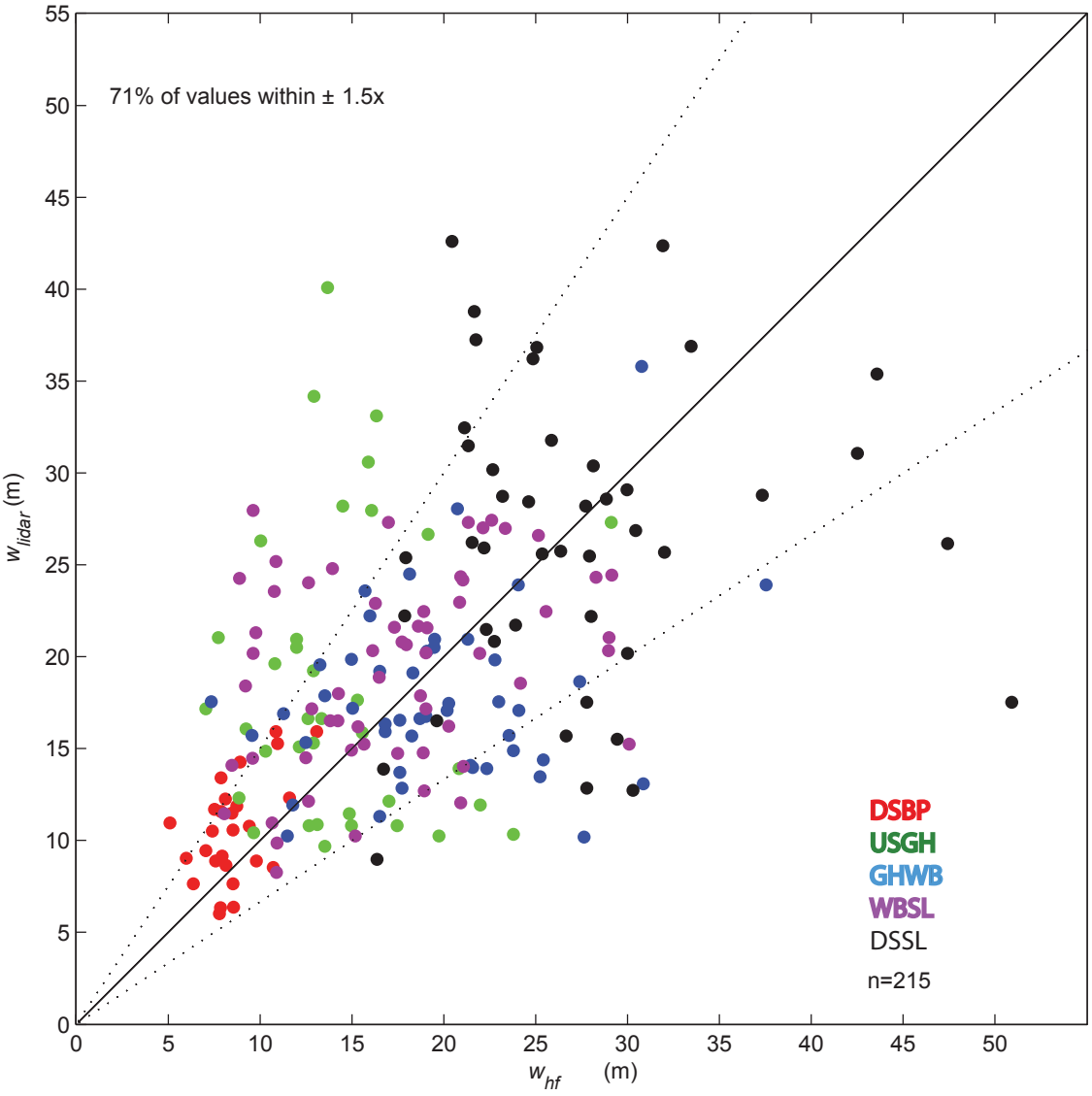

Figure 27. 1:1 plot of channel widths measured from lidar (w_{lidar}) and in the field (w_{hf}) for the WBPR. Each color corresponds to a separate survey segment.

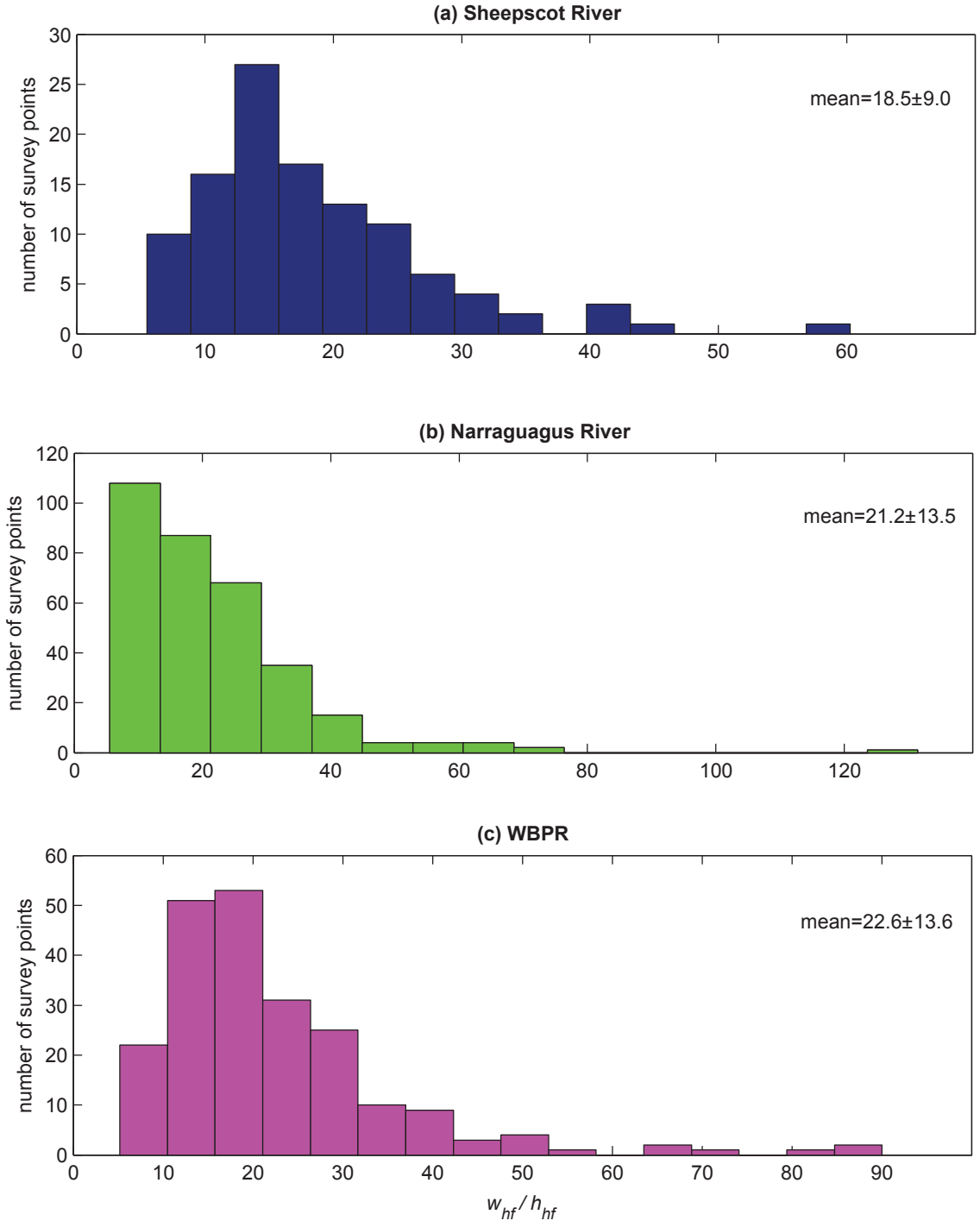

Figure 28. Histograms of high-flow width to depth ratios (w_{hf}/h_{hf}) for all three study rivers. The axis scales vary between panels.

4.2.2 Bed shear stress measurements and interpretation

All three rivers display a close relationship between bed shear stress calculated using GIS measurements of S_{lidar}, A and w_{lidar} (Equation 5, referred to here as $\tau_{b\ pred}$) and bed shear stress calculated using S_{lidar} and h_{hf} (Equation 2, referred to here as $\tau_{b\ field}$) for higher shear stresses, but the correspondence is somewhat weaker below about 20 Pa (Figures 29-30). In this range, the $\tau_{b\ pred}$ values are more likely to be greater than the corresponding $\tau_{b\ field}$ values by a factor of two. For the WBPR, 56% of the $\tau_{b\ pred}$ values fall within a factor of ±2 of the $\tau_{b\ field}$ values (Figures 30). The worst predictions of bed shear stress occur in the WBSL segment of the river, which has a higher sediment load and is more depositional relative to the other segments (Figure 31). Removing the WBSL segment from the data provides a match of 68% of predicted shear stresses within a factor of ±2 of field shear stress. This is similar to the shear stress prediction accuracy in the Narraguagus and Sheepscot Rivers (Figure 30).

The ability to accurately measure channel width using lidar is critical to determining bed shear stress in the channel, as I use w_{lidar} to calculate $\tau_{b\ pred}$ (Equation 5). As mentioned in section 4.2.1, 71% of w_{lidar} measurements fall within a factor of ±1.5 of w_{hf} measurements. In order to evaluate the potential influence of this difference in width measurements, I calculate $\tau_{b\ pred}$ using the field-measured w_{hf} in place of w_{lidar} (Equation 7):

$$\tau_{b\ pred(w_{hf})} = \rho g n^{3/5} \left[\frac{k_q A^c}{w_{hf}}\right]^{3/5} {S_{lidar}}^{7/10}, \text{(Equation 7)}$$

and compare it to $\tau_{b\ pred}$ calculated using with w_{lidar} (Equation 5, reproduced below):

$$\tau_{b\ pred} = \rho g n^{3/5} \left[\frac{k_q A^c}{w_{lidar}}\right]^{3/5} {S_{lidar}}^{7/10}$$

These results show that 89% of the predicted bed shear stress values fall within a factor of ±1.5 of each other (Figure 32). Thus, irrespective of using GIS- (Equation 7) or field-measured (Equation 5) widths to calculate predicted bed shear stress, the resulting values are similar.

4.2.3 Field grain size measurements

The WBPR has a considerably coarser average bed grain size than either the Narraguagus or Sheepscot Rivers, consistent with its higher slope (Figures 2 and 33). The DSBP and USGH segments have a finer and greater overall range of $D_{50\ field}$ than the GHWB segment downstream of the Gulf Hagas bedrock canyon (Figure 26h; Table 3). $D_{50\ field}$ decreases downstream from Gulf Hagas, with an abrupt increase at the boundary between the GHWB and WBSL segments at rkm 26.4 (Figures 26 and 34-35). Downstream fining due to selective deposition is a well-documented process (Paola et al., 1992; Rice and Church, 1998; Davey and LaPointe, 2007) and a clear downstream fining trend in $D_{50\ field}$ is noticeable leading into Silver Lake (WBSL, Figures 22, 26g and 34-35). Downstream of Silver Lake (DSSL), the range and magnitude of $D_{50\ field}$ is restricted relative to WBSL (Figure 35e-f; Table 3).

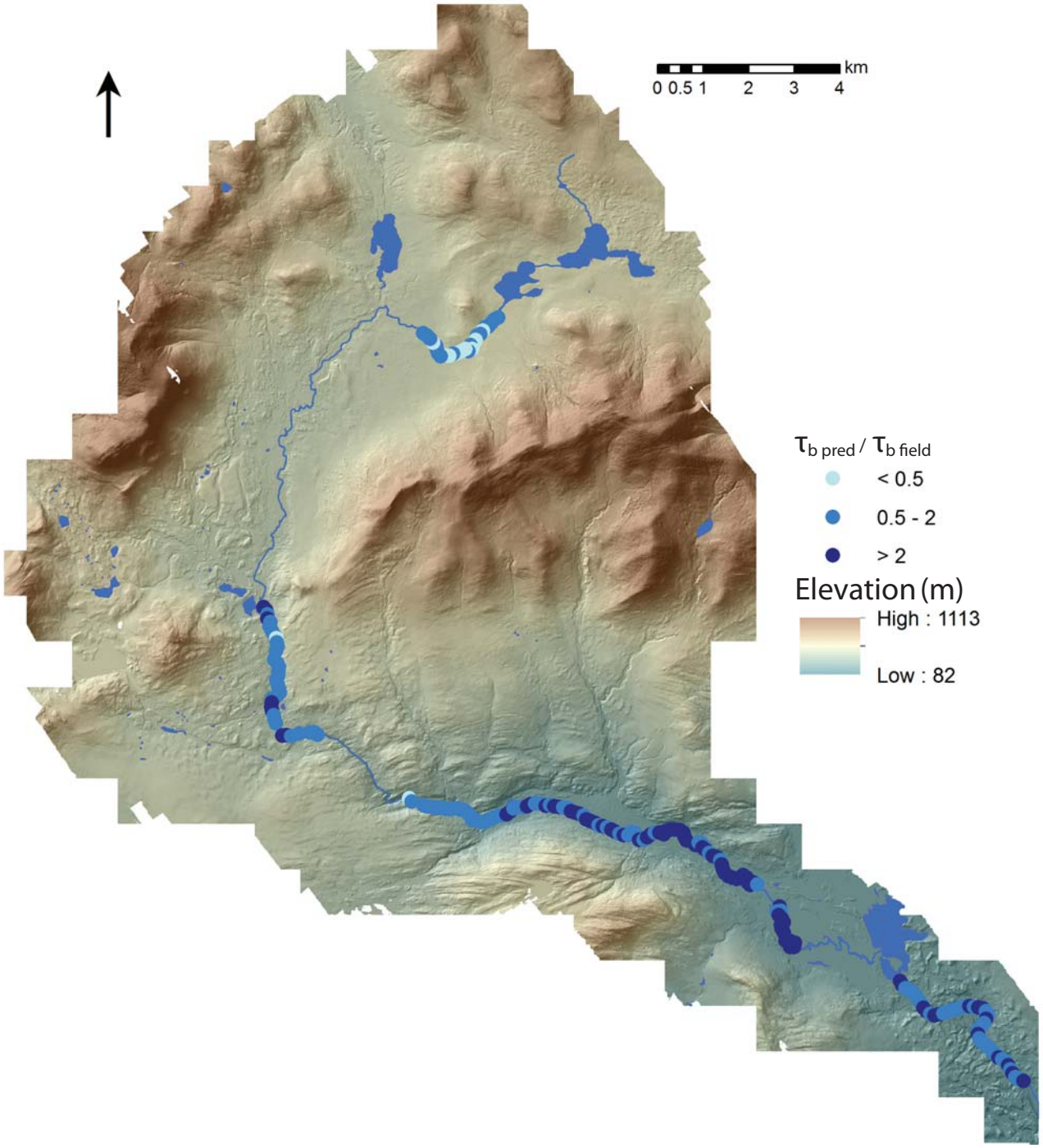

Figure 29. Shaded relief map showing the ratio of predicted to field-measured bed shear stress ($\tau_{b\ pred} / \tau_{b\ field}$) on the WBPR.

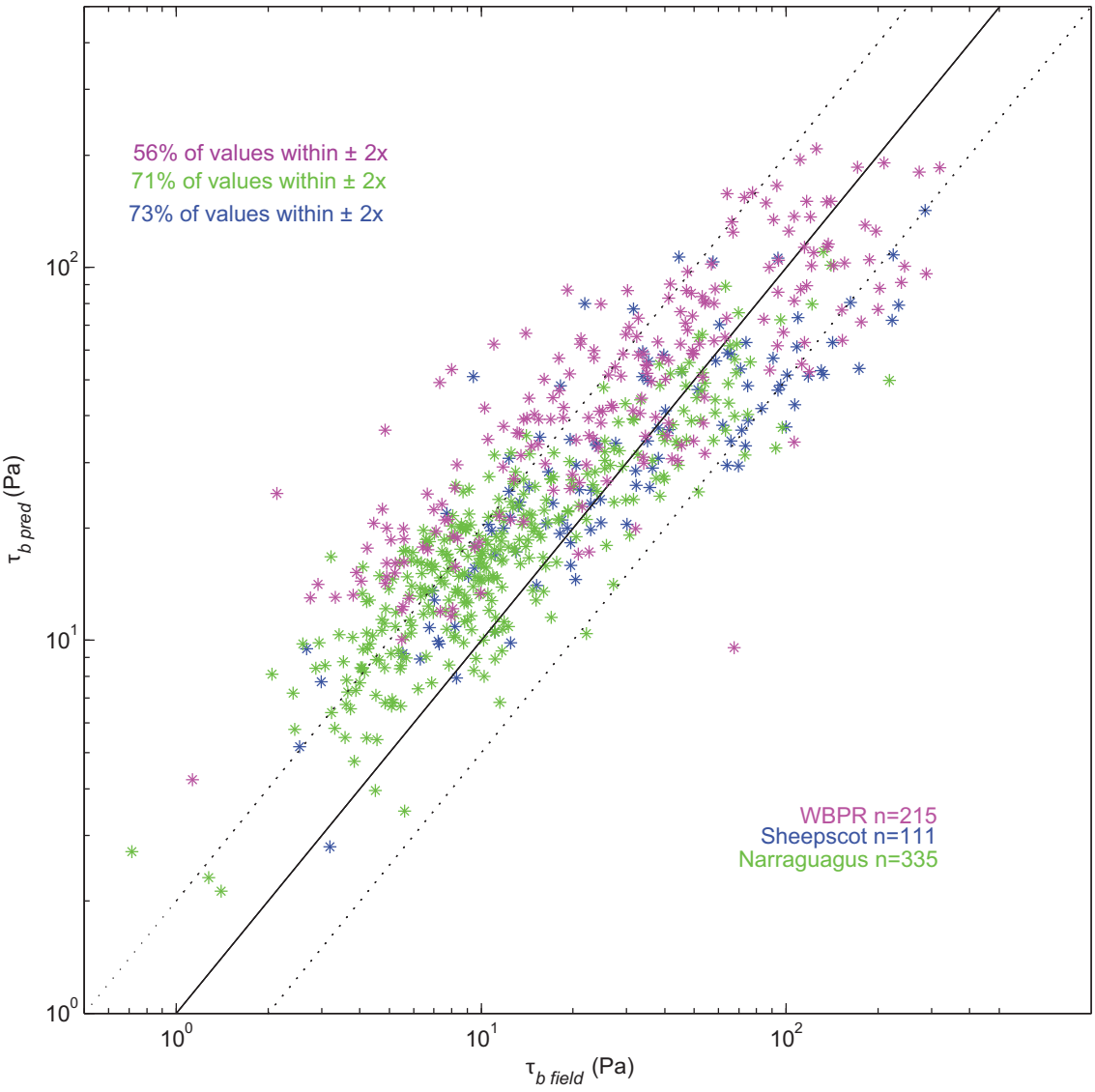

Figure 30. 1:1 plot of predicted bed shear stress ($\tau_{b\ pred}$) to field-measured bed shear stress ($\tau_{b\ field}$) for all three study rivers.

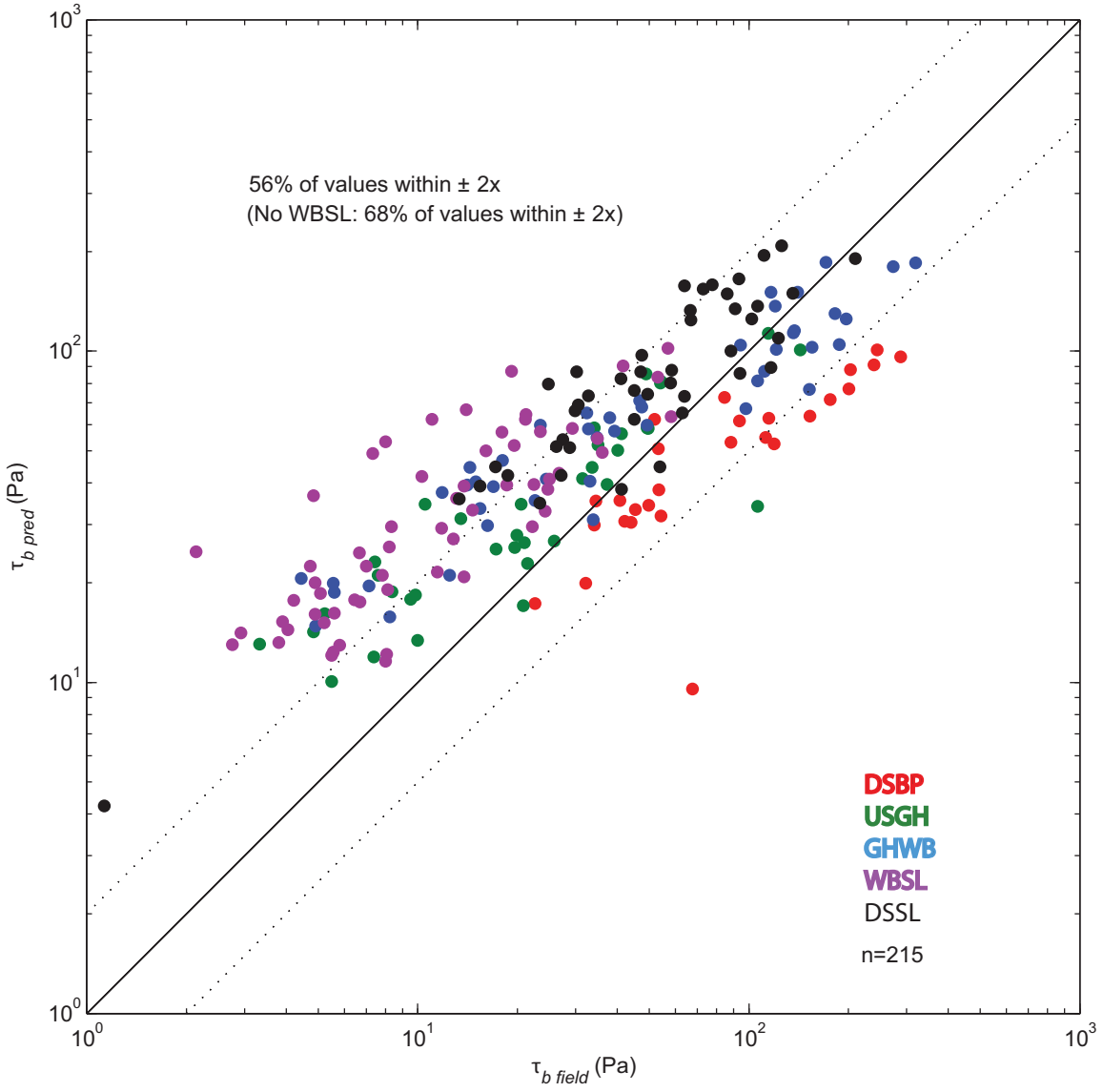

Figure 31. 1:1 plot of predicted bed shear stress ($\tau_{b\ pred}$) to field-measured bed shear stress ($\tau_{b\ field}$) for the WBPR. Each color corresponds to a separate survey segment.

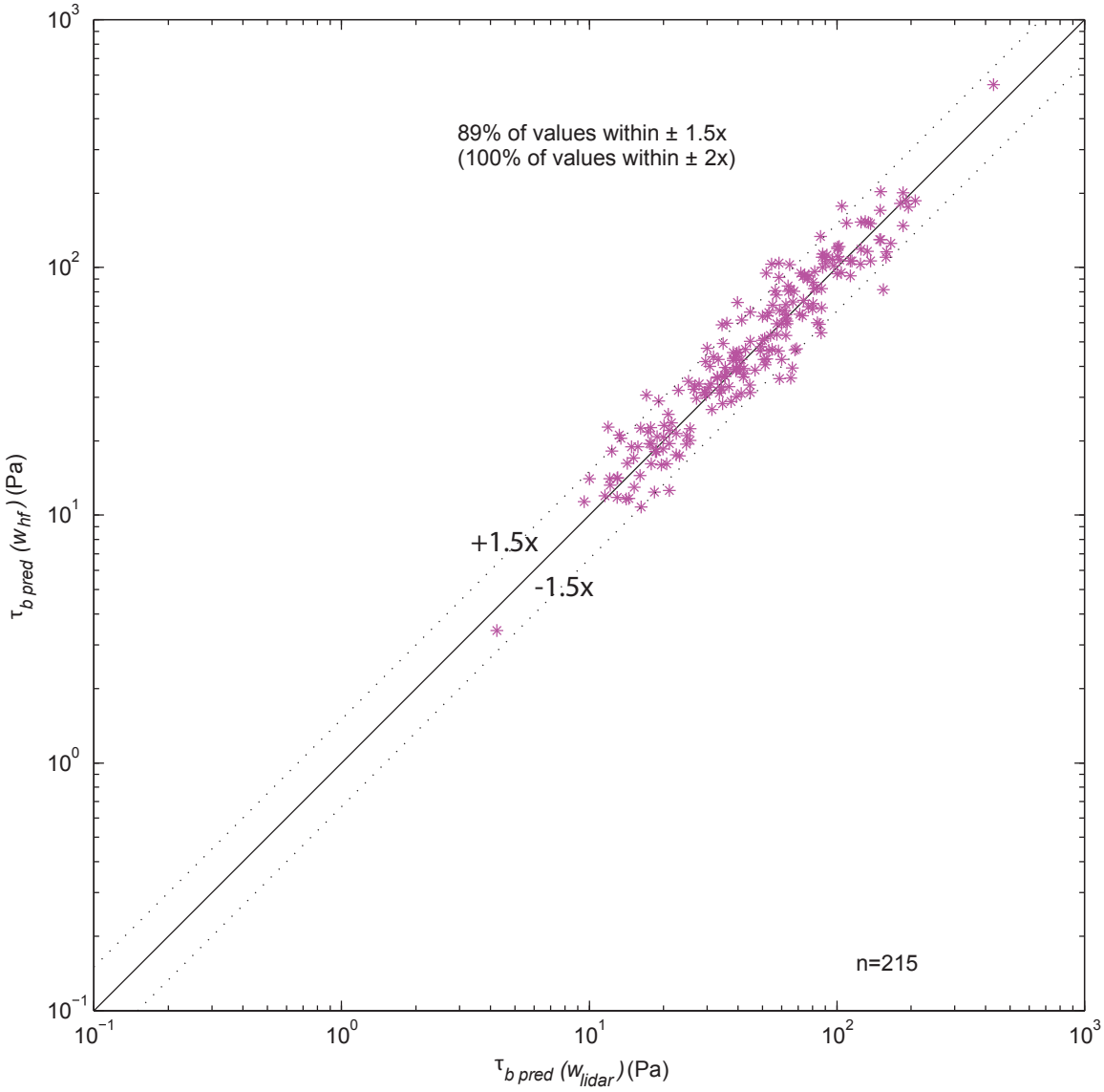

Figure 32. 1:1 plot of bed shear stress calculated using field-measured widths ($\tau_{b\ pred\ (whf)}$) to bed shear stress calculated using lidar widths ($\tau_{b\ pred\ (wlidar)}$) for the WBPR.

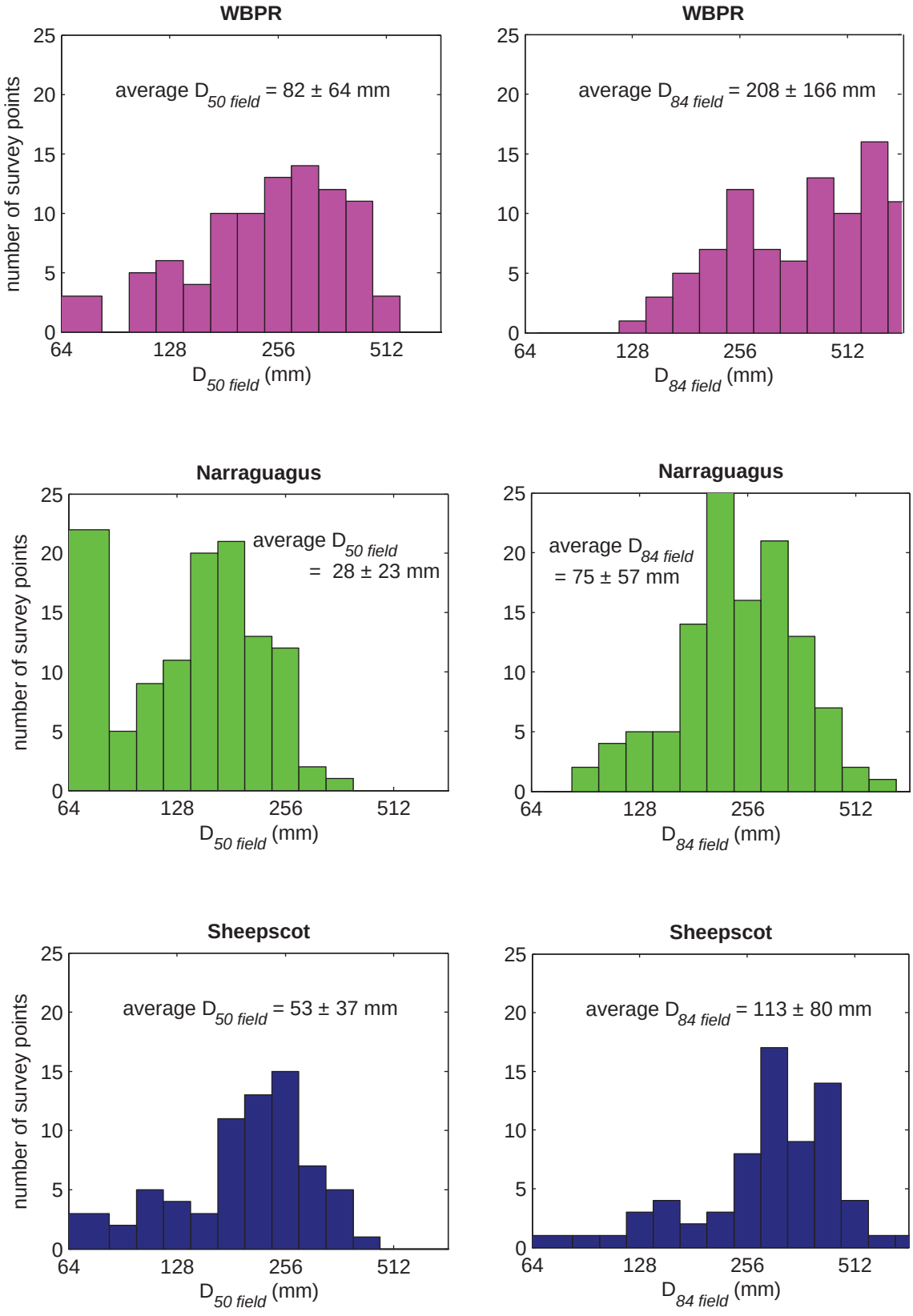

Figure 33. Histograms of field- measured median- and coarse-fraction grain size ($D_{50\ field}$, $D_{84\ field}$) for all three study rivers.

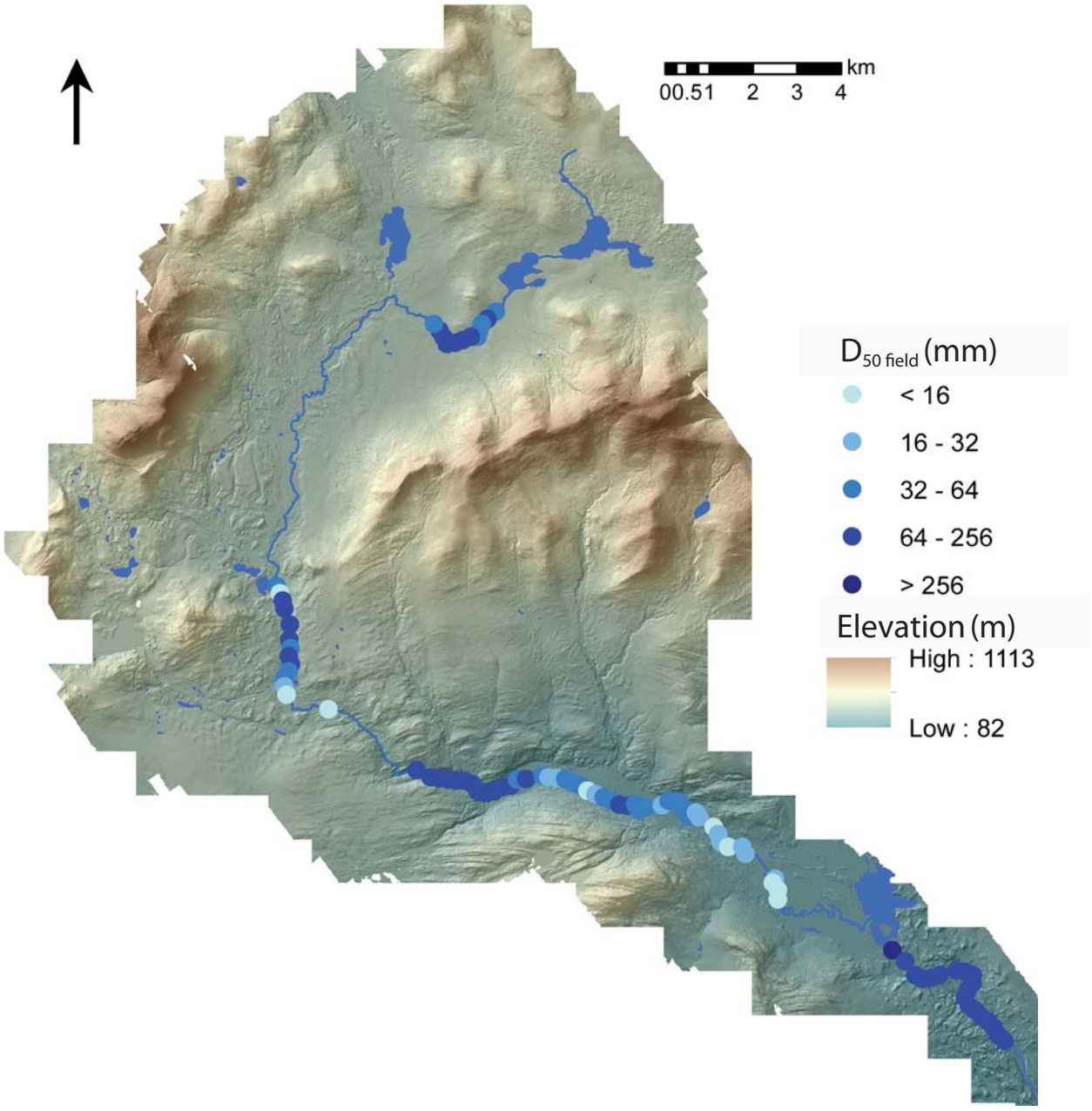

Figure 34. Shaded relief map showing field-measured median grain size ($D_{50\ field}$) for the WBPR.

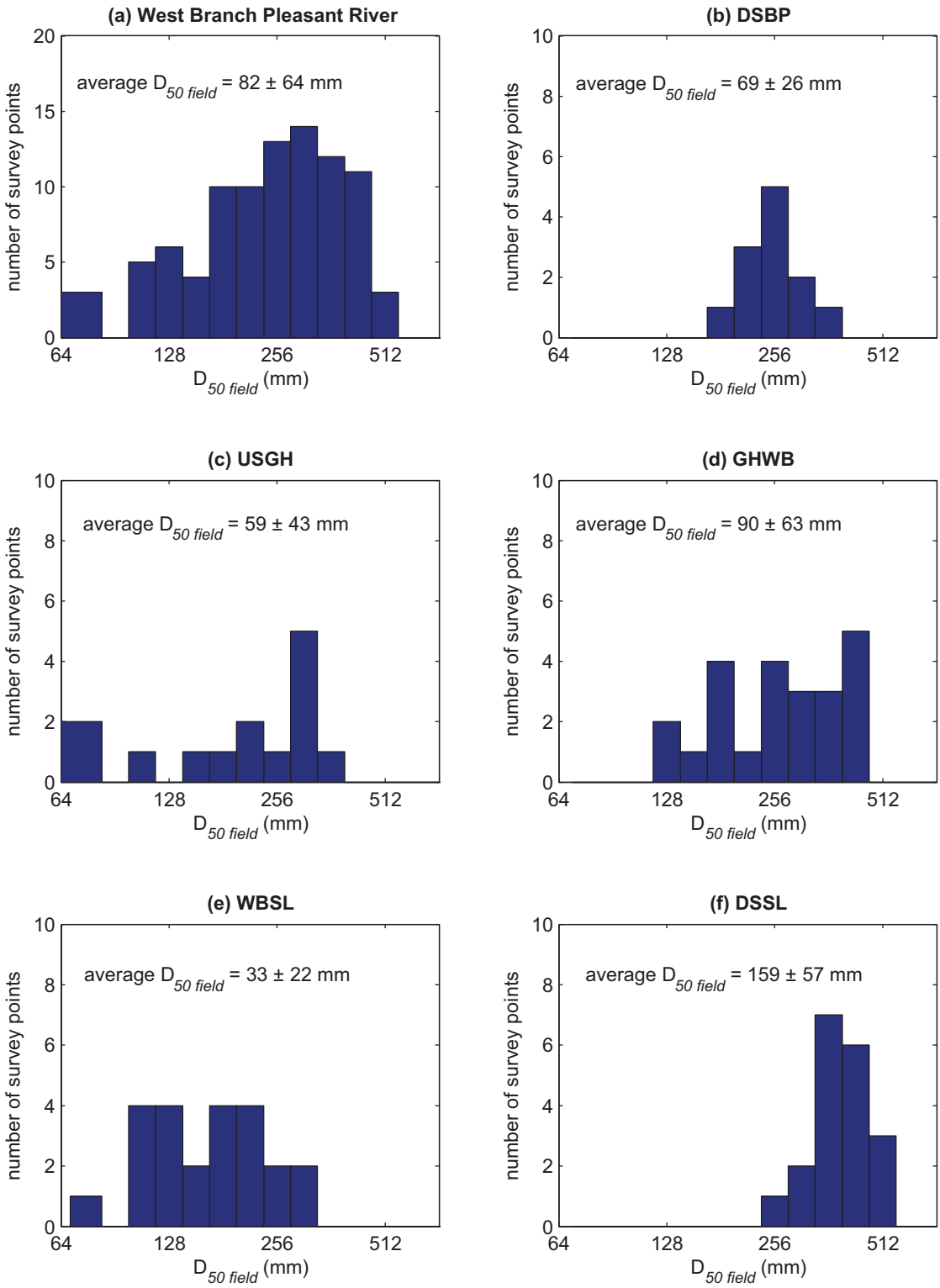

Figure 35. Histograms of field-measured median grain size ($D_{50\ field}$) values for the entire WBPR (a) and each field-surveyed segment of the WBPR (b - f).

4.3 Grain size predictions

Sixty seven per cent of the field measured median grain sizes ($D_{50\ field}$) in the WBPR fall within a factor of ±2 range of the predicted values ($D_{50\ pred}$), compared to 66% in the Narraguagus River and 59% in the Sheepscot River (Figures 36c and 37-38; Table 5; Equation 1).

WBPR segment	$D_{50\ pred\ n=0.04}$, % within ±2x
DSBP	75
USGH	64
GHWB	65
WBSL	48
DSSL	90
Combined	67

Table 5. D_{50} predictions for the WBPR.

The best fit between predicted and field-measured D_{50} occurs in the DSSL segment, where 90% of the predicted values within factor of ±2 of the field-measured values (Figures 39). As with shear stress (τ_b, Figure 31), the least successful predictions occur in the WBSL segment of the WBPR, with 48% within a factor of ±2 (Figure 39; Table 5; Equation 5). This is expected, as τ_b is a strong control on D_{50} (Equation 1). Removing the WBSL segment from this analysis increases the percentage of predicted D_{50} within a factor of ±2 to 73% (Figure 39). This improvement suggests that the transport-limited, depositional WBSL segment is behaving somewhat differently than the other parts of WBPR.

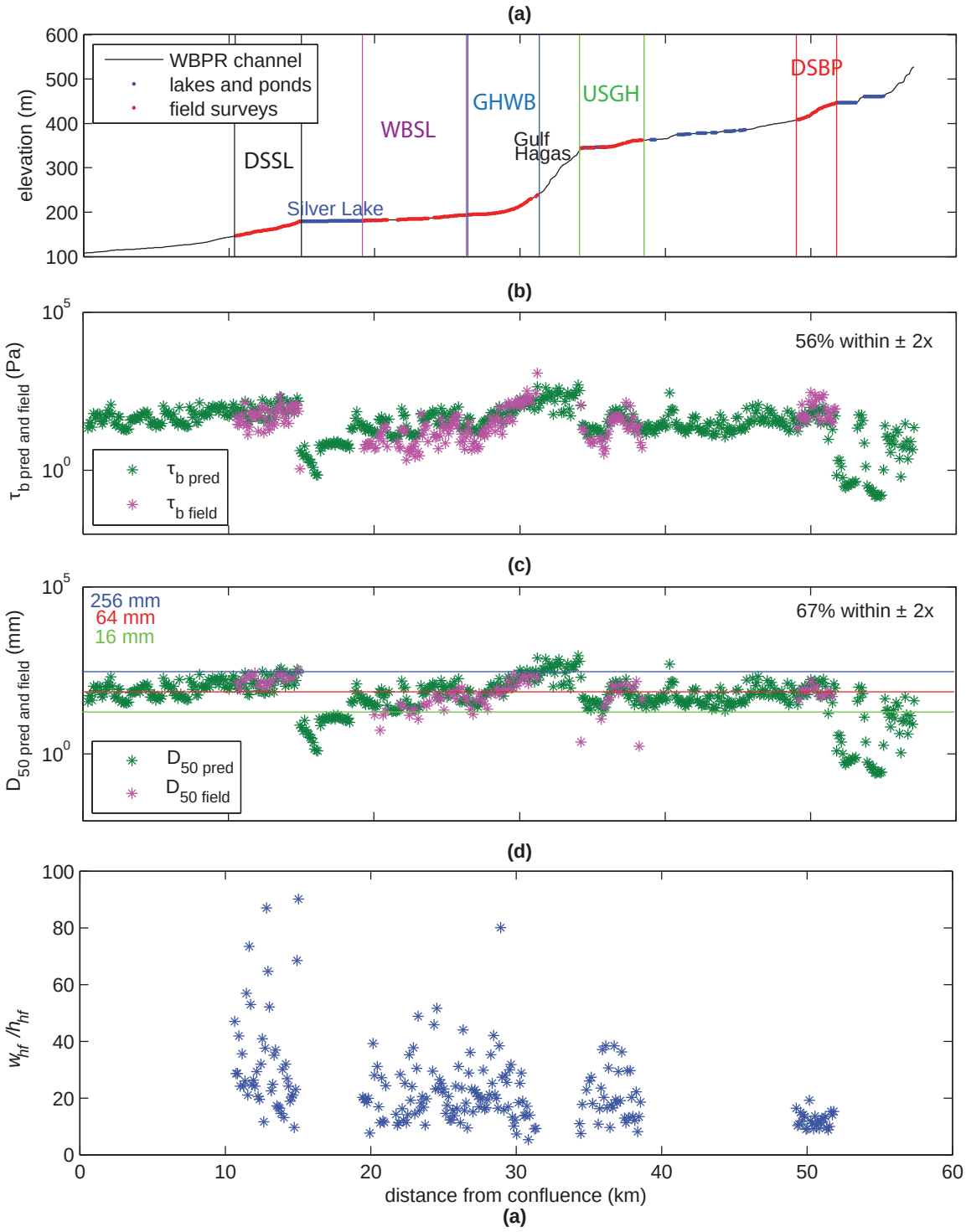

Figure 36. Plots of longitudinal profile indicating field-surveyed segments (a), predicted and field-measured shear stress ($\tau_{b\ pred}$, $\tau_{b\ field}$; b), predicted and field-measured median grain size ($D_{50\ pred}$, $D_{50\ field}$; c) and field high-flow width to depth ratio (w_{hf}/h_{hf}; d) for the WBPR.

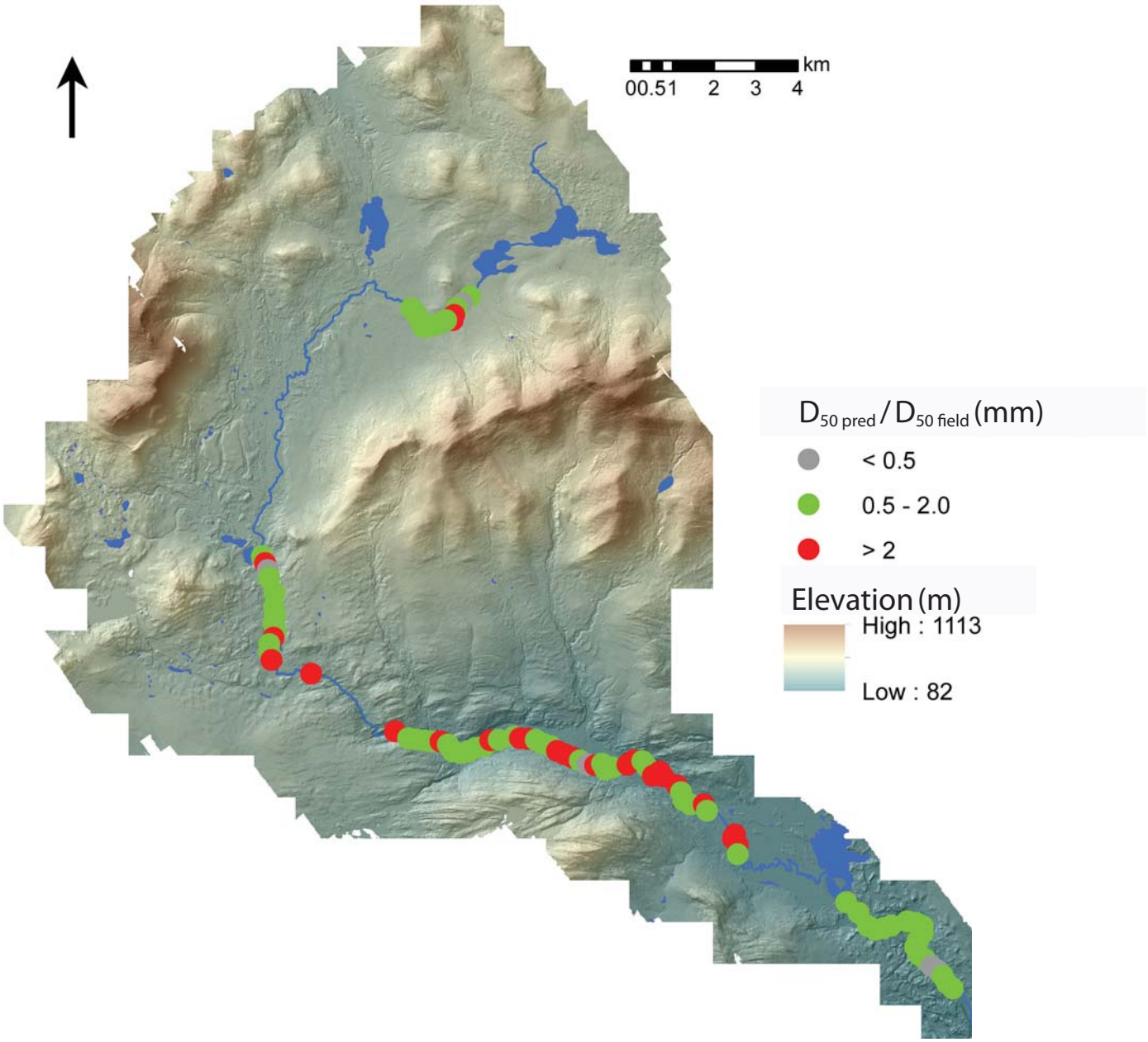

Figure 37. Shaded relief map showing the ratio of predicted to field-measured median grain size ($D_{50\ pred}/D_{50\ field}$) for the WBPR, using a constant intermediate roughness parameter (n=0.04) to calculate $D_{50\ lidar}$ (Equations 1 & 5).

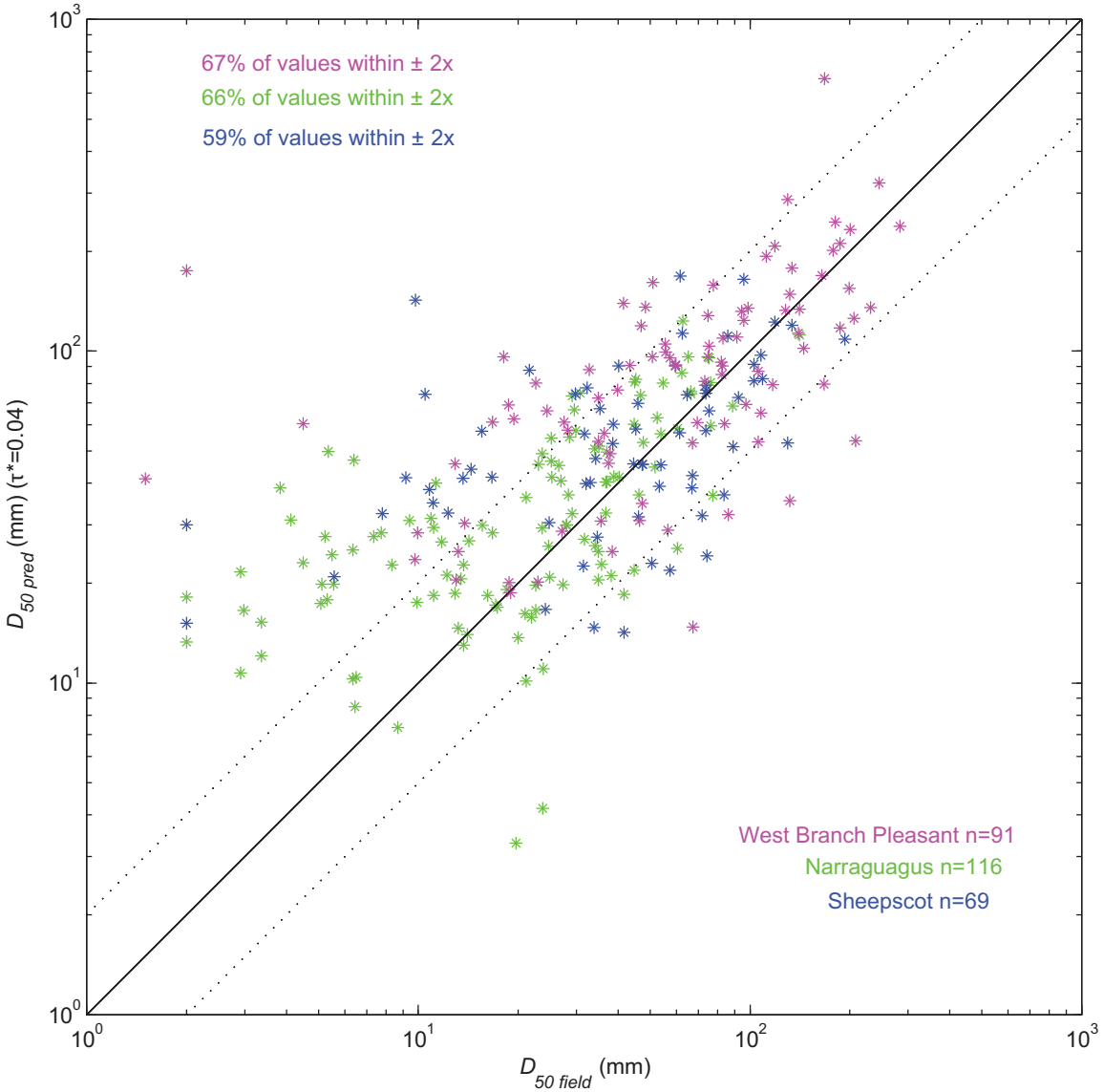

Figure 38. 1:1 plot of predicted median grain size ($D_{50\ pred}$) to field-measured median grain size ($D_{50\ field}$) for the three study rivers.

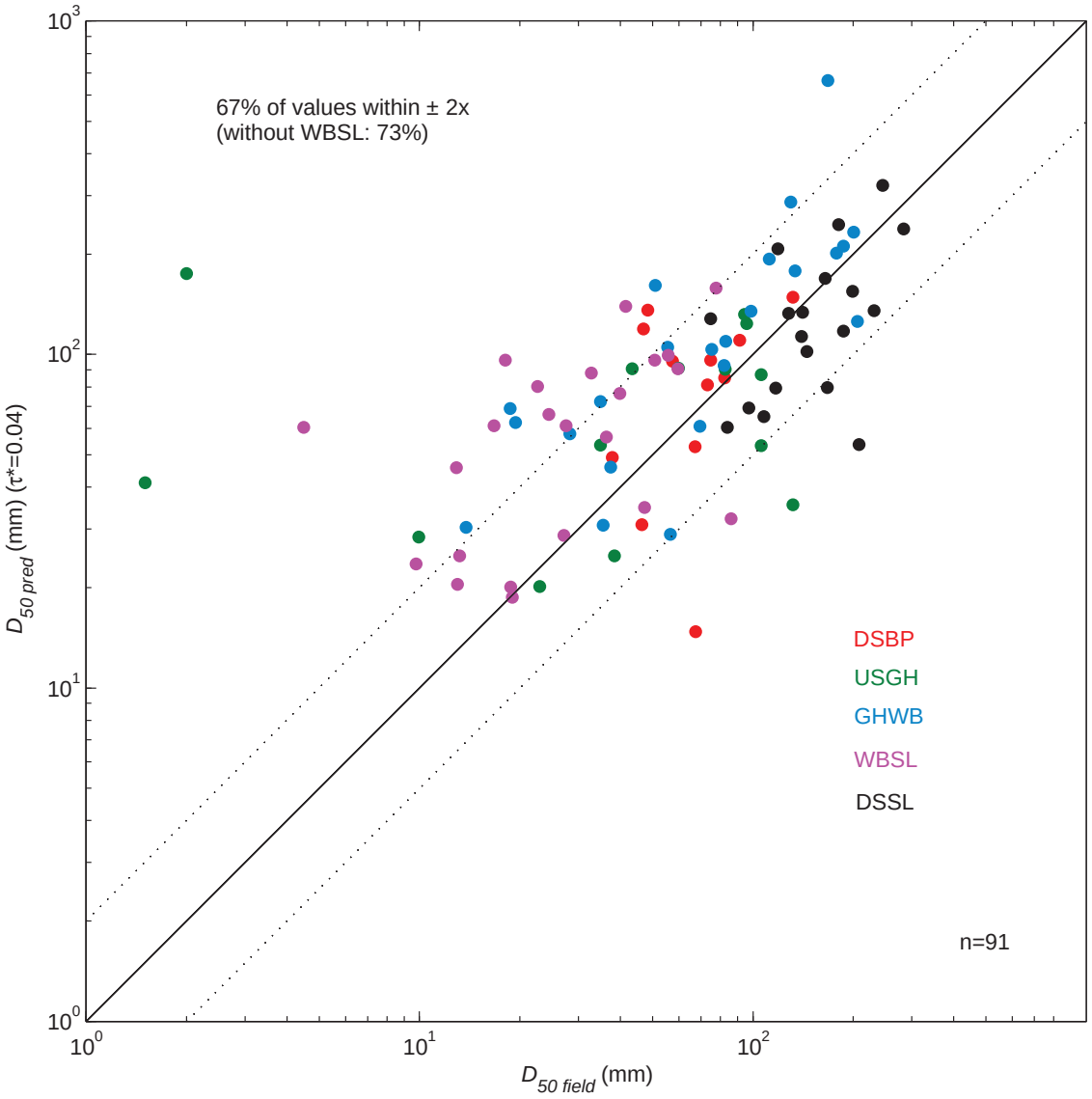

Figure 39. 1:1 plot of predicted median grain size ($D_{50\ pred}$) to field-measured median grain size ($D_{50\ field}$) for the WBPR. Each color corresponds to a separate survey segment.

5. DISCUSSION

In section 5.1, I discuss the application of the Wilkins and Snyder (2011) grain size prediction model to the geomorphology of the West Branch of the Pleasant River. In section 5.2, I discuss the accuracy of the Wilkins and Snyder (2011) model in the high-gradient paraglacial WBPR and the potential influence of measurement error in the prediction results. In section 5.3, I compare this study to prior D_{50} prediction studies and explore the influence of variations in channel roughness on D_{50} predictions. I then compare channel parameters with the prediction equations of Parker et al. (2007) to test whether the study segments behave like single-thread alluvial gravel channels. I conclude the chapter in section 5.4 by addressing the implications of these results for channel restoration projects.

5.1 Model application to the WBPR

Here I discuss locations on the WBPR where the model prediction results fail, focusing on the influence of sediment supply and downstream fining of grain size.

5.1.1 Model results and sediment supply

In the WBPR, the model accurately predicts bed grain size (D_{50}) in the range for ideal salmon spawning habitat (~50 mm), but tends to fail in finer parts of the channel ($D_{50} \leq 20$ mm; Figures 36c, 37 and 39; Equation 1). This was also seen by Wilkins and Snyder (2011), although the range of misfits on the WBPR is somewhat coarser than misfits on either the Narraguagus or Sheepscot rivers (Figure 38). These observations

support the hypothesis that this prediction model (Equation 1) is most applicable in supply-limited threshold channels where the bed sediment is composed of lag deposits only entrained during floods. The model predicts D_{50} most accurately in segments downstream of ponds or lakes, where sediment supply is low. These segments include the upstream DSBP segment and the downstream DSSL segment, which are relatively devoid of fine substrate (Figures 26g, 34-35, 36c and 39; Table 5). More depositional segments, such as the transport-limited WBSL, support the hypothesis that bed material depends on the size and quantity of sediment supplied to the channel. The WBSL segment has a higher sediment load due to the influence of the White Brook tributary, and the predicted values more closely match the field-measured values where coarse sediment is delivered to the channel (Figures 36c and 37). However, channel complexity (multi-thread vs. single-thread channels) increases and grain size decreases correspond with greater unpredictability and scatter farther downstream (Figures 26g and 36c). In the segments with intermediate matches between $D_{50\ pred}$ and $D_{50\ field}$ (USGH and GHWB), the model predicts grain size reasonably well, despite greater channel and $D_{50\ field}$ variability than DSBP or DSSL (Figures 16-20, 26h and 36c-d; Table 5).

In light of these results, it appears that this approach is a reasonably good predictor of grain size, particularly when the most depositional segment of the WBPR is excluded. This supports the hypothesis that the model should perform best in supply-limited threshold reaches where bed sediment is primarily composed of lag deposits, and worst in reaches where fine substrates predominate and D_{50} is entrained during more frequent flows. As hypothesized, the model works less well in transport-limited,

depositional, and/or non-threshold-channel segments, such as WBSL, that have increased fine sediment input and a higher degree of channel variability (Figures 36c and 39; Table 5). Channel segments with intermediate prediction accuracy (USGH, GHWB) have some variability with respect to grain size and channel morphology but not enough to significantly offset the predictive power of the model (Figure 36 and 39; Table 5). GIS data (including measurements of slope from DEMs, shaded relief imagery and aerial photographs) are useful for identifying low gradient multi-threaded channel segments (such as WBSL) where predictions are less likely to be successful because they do not fit the threshold channel case.

5.1.2 Downstream fining

Downstream fining of substrate grain size due to selective deposition has been extensively documented in both laboratory and field settings (Paola et al., 1992; Rice and Church, 1998; Davey and LaPointe, 2007), as the flow loses competence across low-gradient stretches of channel, gradually dropping out its larger grain size load. This pattern is evident in the WBPR, as the $D_{50\ field}$ values display a downstream fining trend within each surveyed channel segment of channel (Figures 26g and 36c). This segmented pattern of discrete fining trends is consistent with the sedimentary links concept of Rice and Church (1998), which breaks channels into distinct "links" based on reach-scale lateral inputs of coarse grained sediment. The work of Davey and LaPointe (2007) expands the approach of Rice and Church (1998) to a paraglacial "old mountain" system more similar to the WBPR, as it takes into account coarse sediment inputs from glacial deposits and alluvial fans. In the case of the WBPR, the bedrock canyon supplies coarse

sediment to the channel below Gulf Hagas (Figure 36). An increase in median grain size coincides with the delivery of the White Brook cobble-gravel tributary fan to the channel on river left at rkm 26.4 (Figure 26g). The slope of the channel bed exerts a strong influence on downstream fining, as relatively high-gradient channel segments transition to downstream base levels set by bedrock/coarse boulder reaches (such as upstream of Gulf Hagas and Silver Lake). Slope is an imposed variable in much of the channel (including DSBP and DSSL), but the more depositional WBSL segment suggests that in some locations slope has largely adjusted to the sediment load.

5.2 General application of the Wilkins and Snyder (2011) prediction model

I find that the Wilkins and Snyder (2011) bed grain size (D_{50}) model provides a reasonably accurate prediction of field grain size in an inland, high-gradient paraglacial threshold river system. In this section I explore the relative importance of the model parameters on the bed grain size prediction equation (Equation 1), as well as the potential impact of measurement error.

5.2.1 Predictor strength

Simple linear regressions of S, A, and w against $D_{50\ field}$ show that the lidar-based model (Equation 1) provides a stronger prediction of bed grain size than any of the individual DEM-derived channel parameters (Figure 40). In order to evaluate the influence of S, A, and w_{lidar} on the prediction model, I used standard multiple regression (Table 6; Equation 8). I also examine the relative significance of the regression parameters by testing the null hypothesis that S, A and w_{lidar} are equal to zero, against the

alternative hypothesis that at least one of the variables is not equal to zero. As the p-value <0.05, I reject the null hypothesis that the regression parameters are zero at a significant level of α=0.05, and I conclude that the parameters are jointly statistically significant at α=0.05. An analysis of the individual regression parameters shows that *S* is the most highly statistically significant variable, in that it has the greatest impact on the fit of the regression, with p<<0.05 (Table 6).

$$y = 82.4714 + 29.5190S + 20.0318A + 10.1099w_{lidar}$$

Equation 8. Regression equation.

Regression parameter	Coefficient	Standard error	P-value
S	29.5190	6.1653	6.85E-06
A	20.0318	7.7962	0.01189
w_{lidar}	10.1099	7.3951	0.17511

Table 6. Individual parameter regression data.

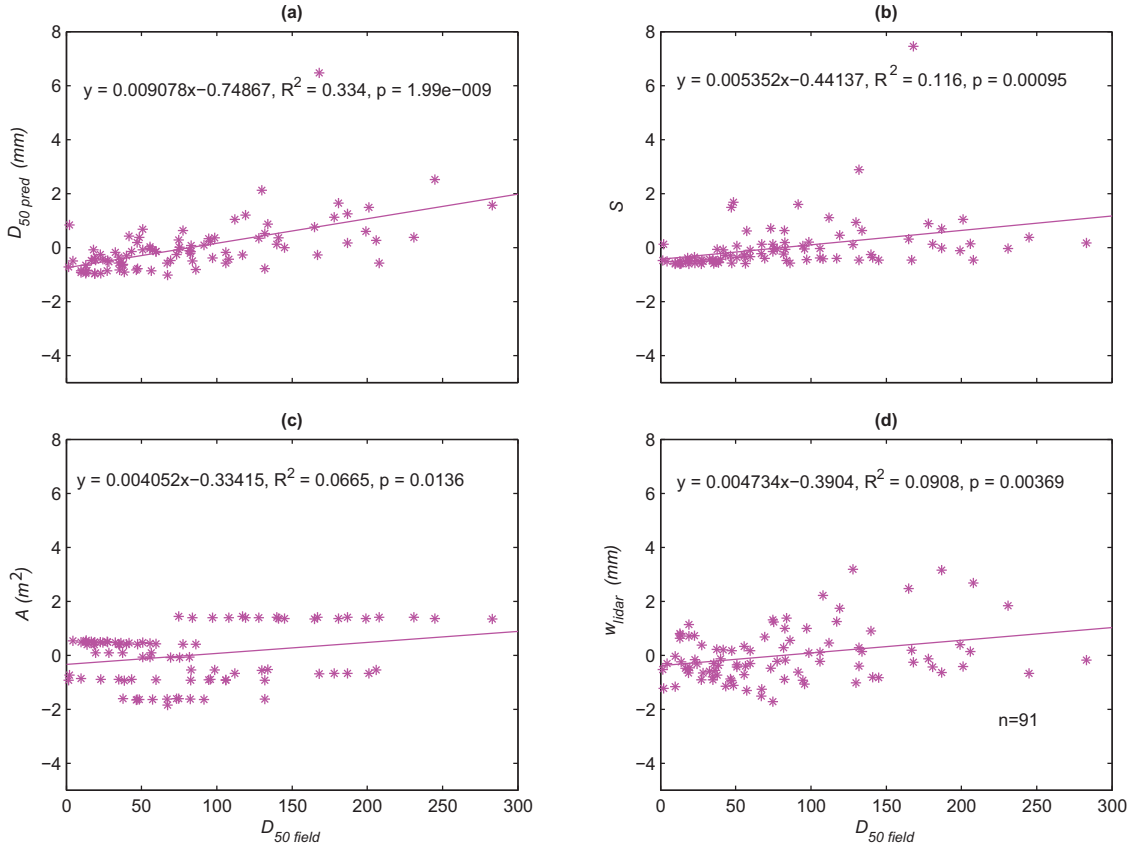

Figure 40. Regressions of predicted median grain size ($D_{50\ pred}$; panel a) and GIS-measured slope (S; panel b), drainage area (A; panel c), and channel width (w_{lidar}; panel d; all standardized to a mean of one and a standard deviation of zero) against field-measured median grain size ($D_{50\ field}$) for the WBPR.

5.2.2 Width measurements

Lidar width measurements (w_{lidar}) impact shear stress measurements (Equation 3), which in turn impact grain size predictions (Equation 1). As a result, measurement error can potentially cascade through the model. Locations where w_{lidar} is wider than w_{hf} are more common than the opposite case, and the magnitudes of the overestimations are greater (Figures 27). The lidar and digital orthophotograph quadrangle (DOQ) maps in Figures 41 show two alluvial, wide valley bottom reaches of the WBPR within the WBSL segment (Figure 26a). The upstream reach (Figure 41 a and c) is gravel-bedded and has no width misfits (w_{lidar}/ w_{hf} greater than a factor of +1.5 or less than a factor of -1.5). In contrast, the downstream reach (Figure 41 b and d) transitions into a primarily sand-bedded channel with a variable multi-threaded morphology by rkm 22.6. Although these reaches appear similar in the lidar and aerial photograph views, the downstream reach has several overpredictions. This suggests that factors (such as grain size) that are not readily apparent in the lidar or aerial photograph views have an impact on prediction accuracy. The presence of vegetation and trees overhanging the channel and unclear vegetation-bank interfaces may be potential limitations on the precision of field width measurements, but the primary difference between these reaches is substrate grain size, which can only be determined by field observation. The tendency of overpredictions of width to occur in fine-grained segments suggests that it is difficult to accurately measure width using GIS in these locations.

In certain underpredicted locations it is likely that fluvial features (such as bars, bank and islands) that appear to be extra-channel features in the lidar images are actually in-channel features within the high flow wetted perimeter of the channel. In other underpredicted locations, such as USGH, where the base level of the segment is controlled by the upstream end of the Gulf Hagas canyon at rkm 34.2, marshes and heavy vegetation make it difficult to discern banks clearly in the lidar dataset. As a result, USGH has the worst relationship between w_{lidar} and w_{hf} (Table 7). Re-measuring w_{lidar} based on vegetation height coverage reveals a better match between w_{lidar} and w_{hf} (Figure 42). To do this, I use ArcGIS tools to subtract the filtered lidar from the unfiltered lidar dataset, which produces a third coverage of the vertical difference between the two initial datasets equivalent to the vegetation height. Overlaying this vegetation coverage on the lidar shaded relief dataset is useful for remeasuring channel widths by differentiating between intra- and extra-channel features which might not be immediately apparent in the lidar images. However, this is not a perfect solution, as it does not fully resolve alluvial channel segments that may not have clearly defined bank-vegetation boundaries. Whether or not this vegetation coverage is referenced, width measurements are most accurate where the channel has clearly defined banks in the aerial photographs, in the lidar imagery and on the ground. Finally, despite the over- and under-predictions of width, shear stress calculations indicate that the variation between w_{lidar} and w_{hf} does not greatly impact τ_b predictions (Figures 30-31).

WBPR segment	% of w_{lidar} within ±1.5x of $w_{field\ hf}$	Count
DSBP	78	27
USGH	53	36
GHWB	74	47
WBSL	75	60
DSSL	73	45

Table 7. Comparison of lidar- and field-measured width.

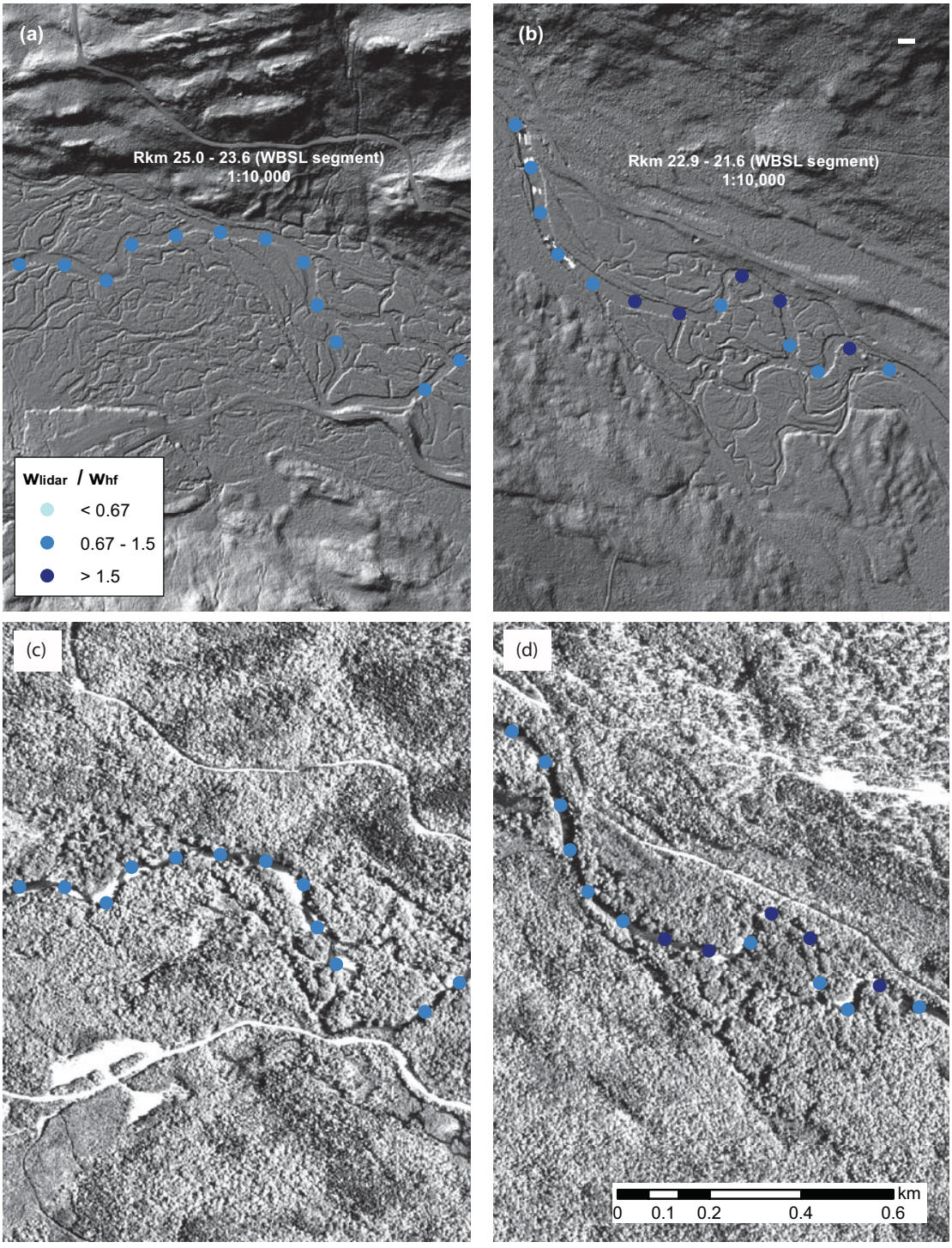

Figure 41. Lidar shaded relief maps (a-b) and digital orthophoto quadrangles (DOQs) (c-d) showing overestimations of channel widths ($w_{lidar}/w_{hf} > 1.5$) in the WBSL segment of the WBPR. The missing datapoints in panels a and c are locations where the flow is too deep to stand in and measure channel width.

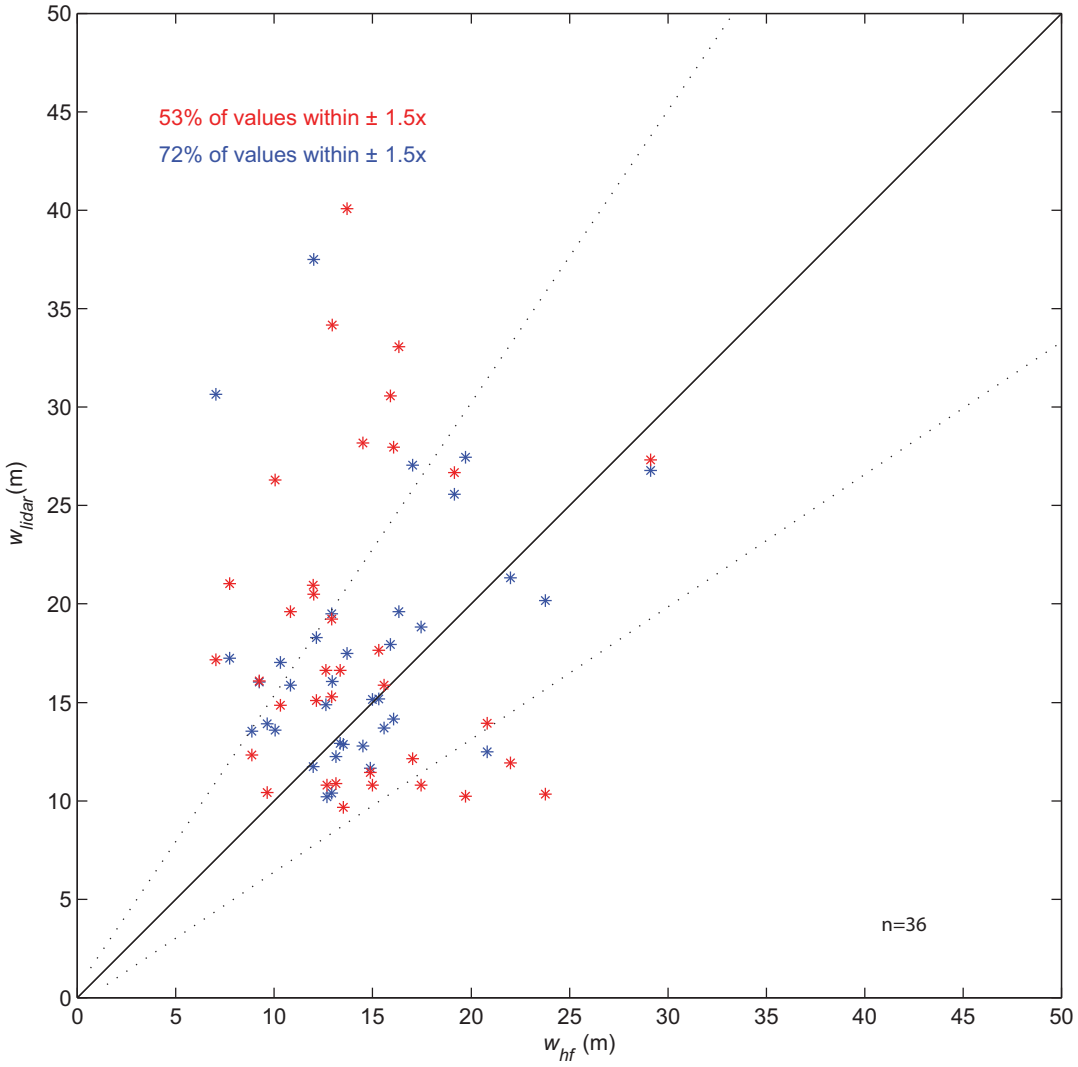

Figure 42. 1:1 plot of original (red) and revised (blue) lidar widths (w_{lidar}) and field-measured widths (w_{hf}) for the USGH segment of the WBPR.

5.3 Comparison to other studies

Many prior studies using DEM and field measurements to predict channel characteristics and habitat serve as useful references for this study (e.g., Carbonneau et al., 2004; Legleiter et al., 2004; Coloumbe-Pontbriand and LaPointe, 2004; Carbonneau et al., 2005; Fonstad and Marcus, 2005; Hedger et al., 2006; Neeson et al., 2007; Donaldson et al., 2009; Kim and LaPointe, 2010; Donaldson and Sklar, 2010). I focus on using channel geometry to predict substrate grain size, building off of Wilkins and Snyder (2011) and similar to Buffington et al. (2004). In this section I will discuss the important distinctions between the model I use and the Buffington et al. (2004) approach, as well as potential improvements to the model. I will also compare this study to the Parker et al. (2007) approach toward predicting alluvial channel geometry in order to explore where the WBPR does not fit the threshold channel case.

5.3.1 Comparison to Buffington et al. (2004): channel roughness

An objective of this study is to use a simple, easily applied model to predict grain size at a channel-length scale. Results of the bed grain size (D_{50}) predictions indicate that it is a reasonably good approach (Figures 37-39), but it raises the question of ways to improve or fine tune the model. Prediction of D_{50} using Equation 1 assumes a constant value for Manning roughness coefficient (n) of 0.04 (Table 8). This value of n is assigned based on visual comparison to similar rivers with measured roughness (Barnes, 1967), as well as precedence in the Wilkins and Snyder (2011) study of similar rivers. However, Buffington et al. (2004) took variations in channel roughness and channel type into account in their grain size predictions, and so in order to explore the potential effect of

roughness I compare grain size predictions using three approximated roughness values: n=0.06 (high-end), n=0.04 (assumed value) and n=0.03 (low-end) (Figures 43-44; Table 8). The low-end n values produce the best overall match with field-measured grain size, while the high-end roughness predictions produce the worst fit. However, the low-end n values produce a better fit than the assumed n value in only the GHWB and WBSL segments (Figure 44). As previously discussed, the WBSL segment is more fine-grained and depositional than the other channel segments (Figure 35). Excluding this segment from the calculations produces a better match for each value of n, while the best fit occurs with the intermediate roughness (n=0.04; Figure 44b). Varying roughness by segment along the channel longitudinal profile may be a useful approach for improving the accuracy of the grain size predictions.

WBPR segment	$D_{50\ pred\ (n=0.03)}$, % within ±2x	$D_{50\ pred\ (n=0.04)}$, % within ±2x	$D_{50\ pred\ (n=0.06)}$, % within ±2x
DSBP	67	75	67
USGH	64	64	64
GHWB	78	65	57
WBSL	57	48	26
DSSL	84	90	84
Combined segments	71	67	57
Combined (no WBSL)	74	76	68

Table 8. Relationship between predicted ($D_{50\ pred}$) and observed ($D_{50\ field}$) median grain size for each channel "link," using a range of roughness parameters to calculate $D_{50\ lidar}$. Combined data shows the total for the entire surveyed reaches of the river, while the combined (no WBSL) data excludes the alluvial WBSL segment.

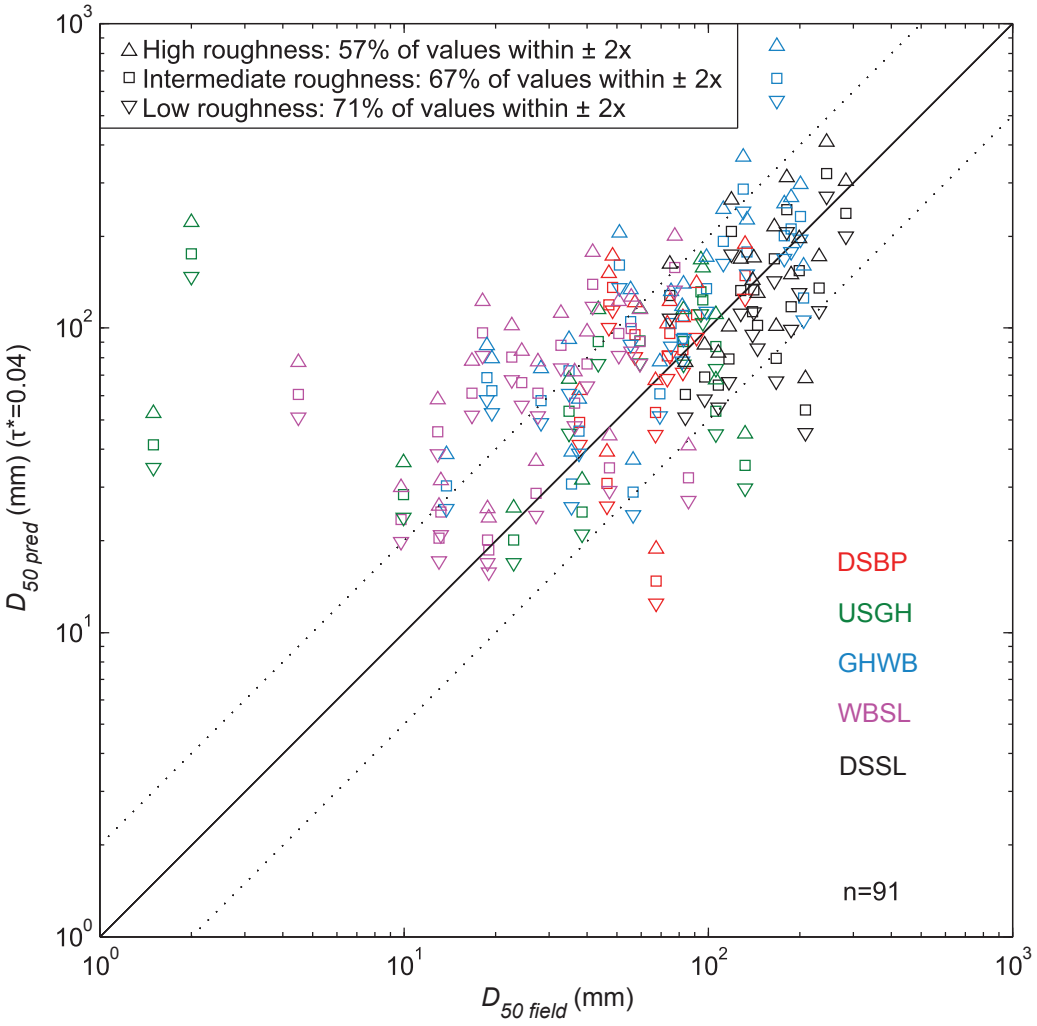

Figure 43. 1:1 plot of predicted median grain size ($D_{50\ pred}$) to field-measured median grain size ($D_{50\ field}$) with varying roughness (n) for the WBPR. Each color indicates a separate field-surveyed segment and each shape indicates a different n value.

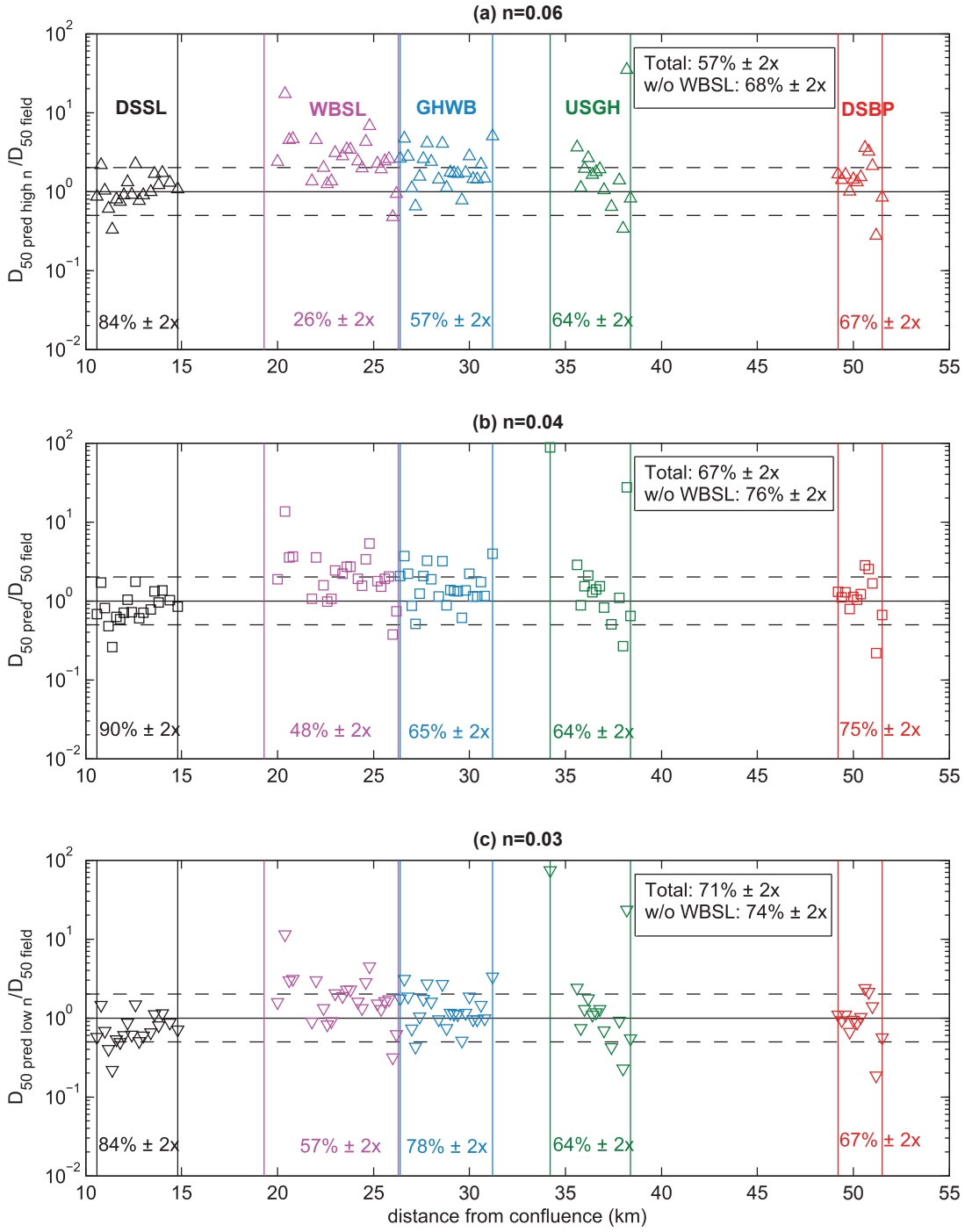

Figure 44. Plots of the ratio of predicted to field-measured median grain size ($D_{50\ pred}/D_{50\ field}$) for the WBPR. Each panel indicates a different roughness value (high roughness: n=0.06 (a), intermediate roughness: n=0.04 (b), and low roughness: n=0.03 (c)). Each color indicates a separate field-surveyed segment.

5.3.2 Comparison to Parker et al. (2007) predictions

In order to explore where the river best fits the threshold channel case, I compare channel geometry measurements to the threshold channel hydraulic geometry equations of Parker et al. (2007). Parker et al. (2007) use direct measurements of Q and D_{50} to predict slope, high-flow channel depth ($h_{pred\ hf}$, Equation 9) and high-flow channel width ($w_{pred\ hf}$, Equation 10) for alluvial single thread gravel-bed rivers with defined banks and floodplains. I use the "high-flow" designation rather than the "bankfull" of Parker et al. (2007) because it does not require a simple, alluvial (channel and floodplain) morphology. Their study found a high degree of universality between its baseline datasets (including rivers in Canada, Britain and USA), and exponents similar to previous studies (Millar, 2005). I do not have field measurements of slope (S), so I focus on h and w predictions. The Parker et al. (2007) relations (Equations 9-10) require measurements of Q (rather than the Q -A approximation, Equation 4) in addition to grain size in order to make predictions, thus this approach is useful strictly for comparison.

$$h_{pred\ hf} = \frac{0.082}{g^{1/5}} Q_{hf}^{2/5} \quad \text{(Equation 9)}$$

$$w_{pred\ hf} = \frac{4.63}{g^{1/5}} Q_{hf}^{0.4} \left(\frac{Q_{hf}}{\sqrt{gD_{50}}D_{50}^2}\right)^{0.0667} \quad \text{(Equation 10)}$$

For the WBPR dataset, 83% of predicted high-flow channel depths ($h_{pred\ hf}$) fall within a factor of ±2x of the field-measured depths (h_{hf}, Figure 45). The relationship between predicted and observed depth values are heavily influenced by drainage area, because Q is approximated using A (Equation 4). This influence is manifested as a

stratification of data points according to segment. The majority of the $h_{pred\ hf}$ misfits are overpredictions in the WBSL segment (Figure 45).

In their paper, Parker et al. use a factor of ±2x ratio to compare their calculations to observed values. However, I use a factor of ±1.5x ratio when comparing widths (Figures 27-31) or shear stress calculated using width measurements (Figure 36; Equations 5 and 7). In order to maintain consistency with the initial analysis and facilitate comparison with Parker et al. (2007), I present results for both ratios (Table 9). 78% of the Parker et al. (2007) width predictions ($w_{pred\ hf}$) fall within a factor of ±2x of w_{hf} measurements (Figure 46; Table 9). As for the relationship between $w_{pred\ hf}$ and w_{lidar}, 75% of $w_{pred\ hf}$ fall within a factor of ±2x of w_{lidar} and most of the misfits occur in the fine-grained and variable WBSL channel segment (Figures 26a-h and 47; Table 9; Equation 8).

WBPR segment	$w_{pred\ hf}$ **vs** w_{hf}, **% within ±1.5x**	$w_{pred\ hf}$ **vs** w_{hf}, **% within ±2x**	$w_{pred\ hf}$ **vs** w_{lidar}, **% within ±1.5x**	$w_{pred\ hf}$ **vs** w_{lidar}, **% within ±2x**	Number of comparison points
DSBP	83	92	75	92	12
USGH	43	71	50	71	14
GHWB	50	95	54	73	22
WBSL	9	35	13	63	24
DSSL	79	100	68	84	19
Combined	49	78	48	75	91

Table 9. Relationship between $w_{pred\ hf}$ and w_{lidar} for the WBPR.

Similar to the results of the initial grain size prediction model (Figures 36c and 37-39; Table 5; Equation 5), the Parker et al. (2007) predictions for the WBSL are less successful than the other segments, indicating that this segment may not be completely single-threaded and gravel-bedded (Table 9). Surprisingly, the more supply-limited

segments (DSBP, DSSL) have better results and behave like threshold channels of Parker et al. (2007), indicating that the channel has adjusted its width and depth to accommodate S, Q and sediment load.

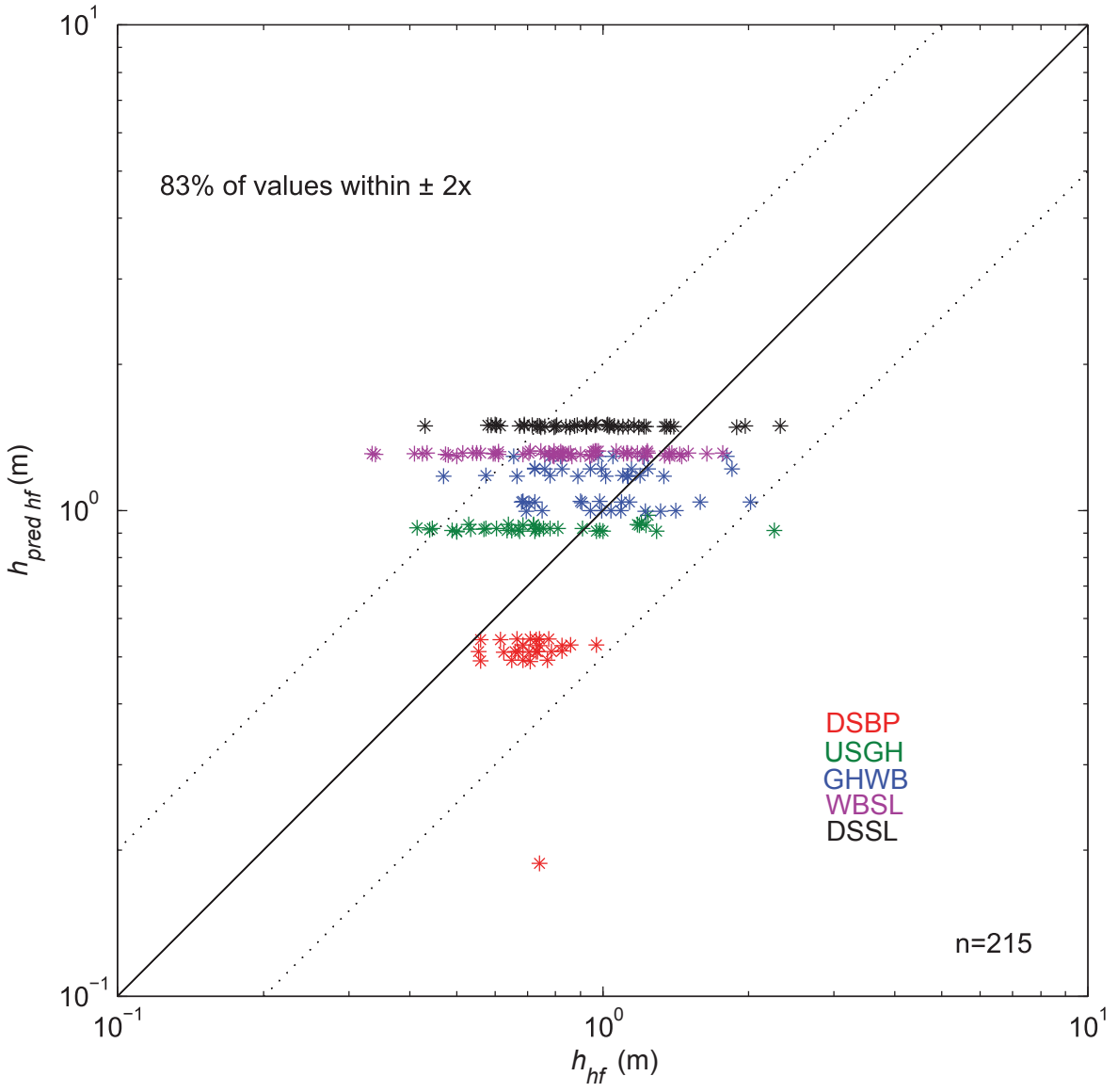

Figure 45. 1:1 plot of predicted high-flow depth calculated using Parker et al. (2007) ($h_{pred\ hf}$; Equation 9) to field-measured high-flow depth (h_{hf}) for the WBPR. Each color indicates a surveyed channel segment of the WBPR.

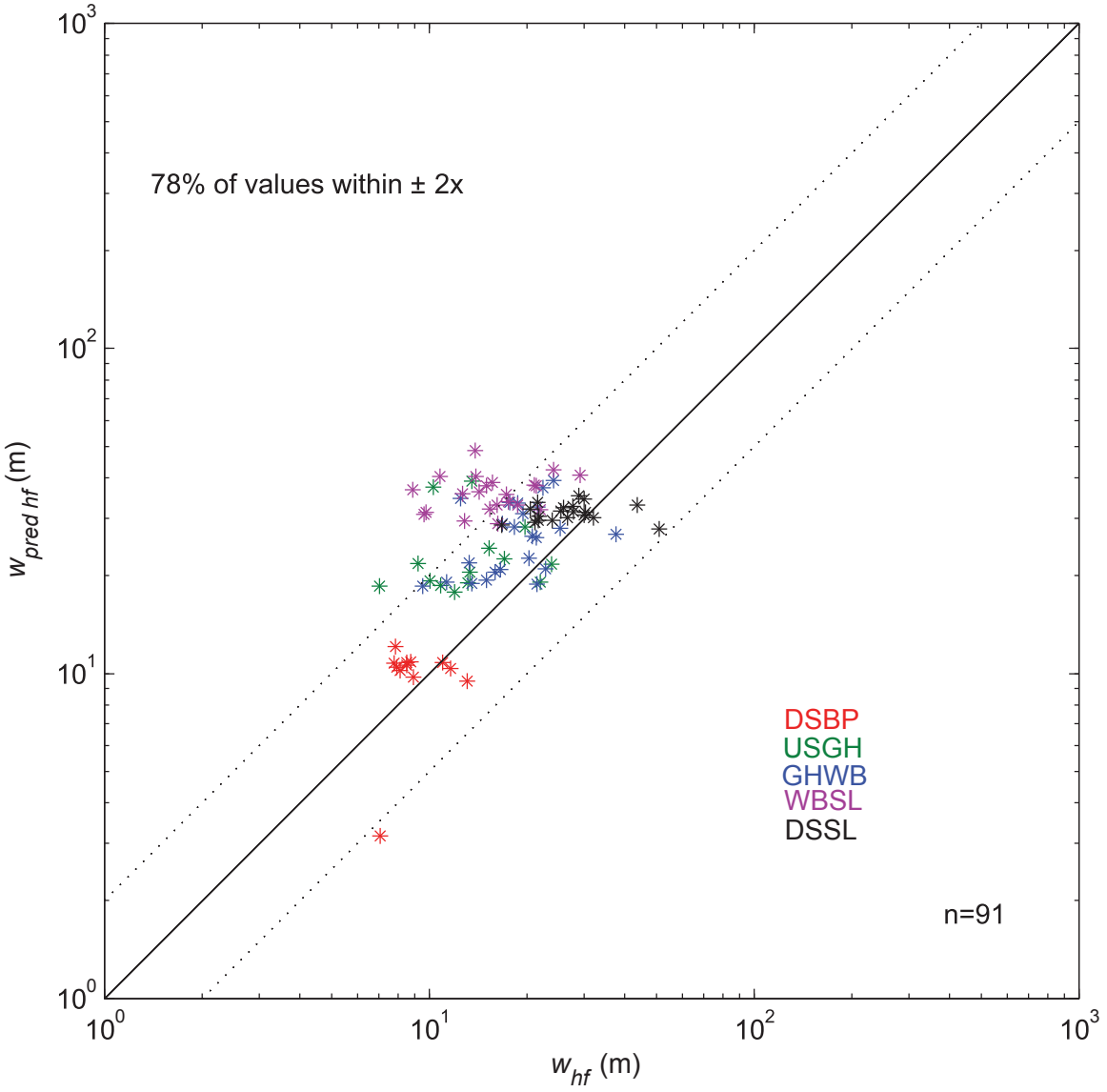

Figure 46. 1:1 plot of predicted high-flow width using Parker et al. (2007) ($w_{pred\ hf}$; Equation 10) to field-measured high-flow width (w_{hf}) for the WBPR. Each color indicates a field-surveyed segment of the WBPR.

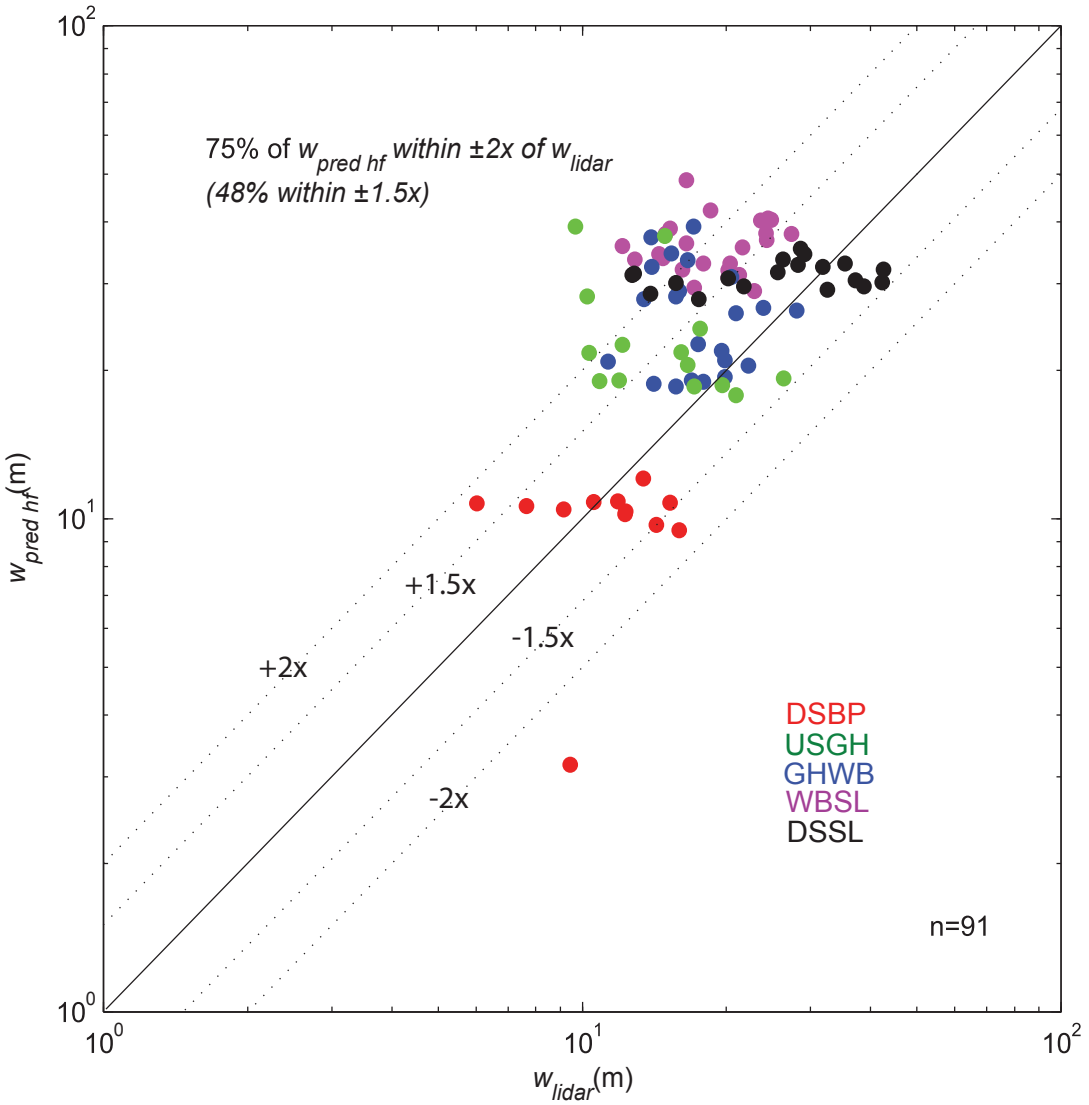

Figure 47. 1:1 plot of predicted high-flow widths calculated using Parker et al. (2007) ($w_{pred\ hf}$; Equation 10) to lidar widths (w_{lidar}) for the WBPR. Each color indicates a field-surveyed segment of the WBPR.

5.4 Implications for restoration

The model provides a reasonably accurate (67% of predicted values within ±2x of field-measured values) picture of bed grain size for the WBPR, but the tendency of the model to overpredict bed grain size when the field grain size is less than approximately 20 mm may result in an estimation of more spawning habitat (16-256 mm) than actually exists in the river (Figures 36c, 37-39). These results are similar to D_{50} predictions from coastal, low-gradient paraglacial rivers (Figure 38; Wilkins and Snyder, 2011), indicating that this prediction approach is applicable at a watershed scale in a range of paraglacial environments. However, both this study and Wilkins and Snyder (2011) find localized places where the model fails: the WBSL segment on the WBPR, and upstream of the former Hemlock Dam site on the Narraguagus. In these areas it is difficult to determine if the model is failing for environmental reasons (e.g., changes in sediment supply due to land use or other influences) or changes in channel type (e.g., gravel-bed single thread to sand-bed multithread.

Channel segments where the grain size predictions work relatively poorly may be useful in identifying and prioritizing restoration projects. As with other D_{50} prediction models (Buffington et al., 2004; Parker et al., 2007), model accuracy is best in single-thread, alluvial gravel bed (threshold) channel segments with low sediment supply (DSBP and DSSL, Figures 37-38; Table 5). Model misfits may point to the influence of variations in local sediment supply due to land use history. The cut wood buried in the bank at rkm 27.6 is a likely example of anthropogenic influence on sediment supply to the channel. Increased erosion and input of fine grained sediment may be linked to the

removal of soil-stabilizing trees, as D_{50} is overpredicted at this location (Figure 20). Wilkins and Snyder (2011) also speculated that D_{50} overpredictions occur where fine legacy sediments that have not yet been remobilized are present. Locations such as these may be indicators of places where potential restoration activities should be focused.

In my analysis I reference a range of grain size (16-256 mm) associated with salmon spawning and rearing habitat suitability, but no one has mapped salmon spawning habitat on the WBPR (Kondolf and Wolman, 1993; Buffington et al., 2004). In contrast, the Buffington et al. (2004) and Wilkins and Snyder (2011) studies provide templates for salmon habitat mapping using D_{50} predictions, and Wilkins and Snyder (2011) mapped potential salmon spawning habitat on the Narraguagus River. The WBPR remains inaccessible to most anadromous species, but the completion of the Penobscot River Restoration Project should enable increased anadromous species passage. Results of this study will be useful in future detailed habitat assessment both on the WBPR and on other rivers. Despite its limitations, this prediction model is an easily applied and time-efficient first-order tool for predicting grain size and estimating habitat suitability.

6. SUMMARY AND CONCLUSION

This study has the dual purpose of extending the application of the Wilkins and Snyder (2011) grain size prediction model (Equation 1) and testing its predictive limits in an inland, high-gradient paraglacial system. Results of this study show that the model works reasonably well for predicting bed grain size at a watershed scale in an inland, high-gradient paraglacial river system, with 67% of predicted values of bed grain size ($D_{50\ pred}$) within ±2x of field-measured values ($D_{50\ field}$; Figures 36c, 37-39). The model performs best in supply-limited single-thread channel segments with gravel-cobble lag deposit beds, and worst in transport-limited depositional segments with relatively fine substrate and greater channel variability. Channel segments that are transitional between these two cases (intermediate channel complexity and grain size distribution) are associated with intermediate grain size prediction accuracy.

The geomorphic parameters addressed in this study reveal the complexity and variability of the paraglacial WBPR. The surveyed channel covers diverse reach-scale morphologies, including the shallow, coarse gravel-bedded upstream reaches, the deeper sand-bedded section above Silver Lake, and the bedrock and boulder dominated segment downstream of Silver Lake.

Comparison between the inland relatively high-relief system of the WBPR and the coastal low-relief Sheepscot and Narraguagus rivers provides a means to explore how rivers interact with varying paraglacial landscapes. In particular, the relative diversity of channel gradient on the WBPR relative to the other two rivers highlights the limitations

of the model and illustrates the influence of base level controls and variations in sediment supply on prediction accuracy.

Questions of habitat suitability as related to bedload entrainment and channel morphology are intrinsically connected to the overall geomorphic character of the river and the interactions between river morphology and ecologic processes. This study provides the geomorphic characterization that will allow for more detailed habitat determination on the WBPR, while also providing a grain size prediction model that is applicable to other rivers. The results are of wide application to any research or restoration project concerned with sediment mobilization and overall channel morphological controls, as stream restoration projects are frequently undertaken without a comprehensive understanding of these factors. This study provides a valuable reference for future research and restoration regarding bedload mobilization, channel morphology and fluvial ecology in an imposed-form deglaciated watershed, as well as a reference for the application of high-resolution GIS analysis to fluvial geomorphologic questions.

REFERENCES

Andrews, E. D. 1983. Entrainment of gravel from naturally sorted riverbed material, *Geol. Soc. Am. Bull.*, **94**: 1225-1231.

Arter, B. 2003. Narraguagus River watershed nonpoint source pollution management plan. Narraguagus River Watershed Council, Cherryfield, ME.

Bangor and Aroostook Railroad Company (Fred H. Clifford). *In the Maine Woods*. Passenger Dept., Bangor and Aroostook Railroad Co., 1902.

Bangor and Aroostook Railroad Company. *In the Maine Woods*. Passenger Dept., Bangor and Aroostook Railroad Co., 1904.

Bangor and Aroostook Railroad Company. *In the Maine Woods*. Passenger Dept., Bangor and Aroostook Railroad Co., 1905.

Barnes, H.H. Jr., 1967. Roughness Characteristics of Natural Channels, U.S. Geological Survey water supply paper 1849, United States Government Printing Office, Washington, D.C., 213 p.

Barnhardt, Walter A., W.R. Gehrels, Belknap D.F., Kelley J.T. 1995, Geology; Late Quaternary relative sea-level change in the western Gulf of Maine: Evidence for a migrating glacial forebulge. *Geology*, **23**: 317–320.

Belknap, D.F., Andersen, B.G., Anderson, R.S., Anderson, W.A., Borns, H.W., Jr., Jacobson, G.L., Kelley, J.T., Shipp, R.C., Smith, D.C., Stukenrath, R., Jr., Thompson, W.B., Tyler, D.A. 1987, *Late quaternary sea level changes in Maine. Special publication: The Society of Economic Paleontologists and Mineralogists*, **41**: 71-85.

Buffington J.M., Montgomery D.R. 1997. A systematic analysis of eight decades of incipient motion studies, with special reference to gravel-bedded rivers. *Water Resources Research* **33** (8): 1993-2039.

Buffington, J.M., Montgomery, D.R., and Greenberg, H.M. 2004. Basin-scale availability of salmonid spawning gravel as influenced by channel type and hydraulic roughness in mountain catchments. *Can. J. Fish. Aquat. Sci.*, **61**: 2085-2096.

Carbonneau, P.E., Lane, S.N., Bergeron, N. 2004. Catchment-scale mapping of surface grain size in gravel bed rivers using airborne digital imagery. *Water Resources Research*. doi: 10.1029/2003WR002759.

Carbonneau, P.E., Bergeron, N., Lane, S.N. 2005. Automated grain size measurements from airborne remote sensing for long profile measurements of fluvial grain sizes. *Water Resources Research*. doi: 10.1029/2005WR003994.

Castele, M.R. 2007. Modeling sediment transport and quantifying channel morphology of the Sheepscot River, coastal Maine. *Boston College Dissertations and Theses.* Paper AAI1447096. http://escholarship.bc.edu/dissertations/AAI1447096.

Coloumbe-Pontbriand, M. and LaPointe, M. 2004. Geomorphic controls, riffle substrate quality and spawning site selection in two semi-alluvial salmon rivers in the Gaspé Peninsula, Canada. *River Res. Applic*. **20**: 577-590.

Davey, C., Lapointe, M. 2007. Sedimentary links and the spatial organization of Atlantic salmon (Salmo salar) spawning habitat in a Canadian Shield river. *Geomorphology,* **83**: 82–96.

Donaldson, E.T., Sklar, L.S., Marshall, J.A.; Ligon, F.K., Dietrich, W.E. 2009. Topographic and lithologic controls on occurrence of cobble-boulder channel beds: implications for salmonid over-wintering habitat. *American Geophysical Union, Fall Meeting 2009*, abstract #EP54A-05. http://adsabs.harvard.edu/abs/2009AGUFMEP54A..05D.

Donaldson, E.T., Sklar, L.S. 2010. An empirical model to predict the occurrence of cobble-boulder channel beds. *American Geophysical Union, Fall Meeting 2010*, abstract #EP41B-0708. http://adsabs.harvard.edu/abs/2010AGUFMEP41B0708D

Dunne, T., and Leopold, L.B. 1978. *Water in Environmental Planning*. W.H. Freeman and Co., New York, 818 p.

Eastman, J. W., 1967. David Pingree's Iron Works: Essex Institute Historical Collections, Salem, Massachusetts. 189-198.

Farrar, Charles Alden John. *Illustrated guide book to Moosehead Lake and vicinity*. Lee and Shepard, 1880. 216 p.

Fay, C., Bartron, M., Craig, S., Hecht, A., Pruden, J., Saunders, R., Sheehan., T., Trial, J. 2006. Status Review for Anadromous Atlantic Salmon (*Salmo salar*) in the United States. *Report to the National Marine Fisheries Service and U.S. Fish and Wildlife Service*, 294.

Fonstad, M.A., Marcus, W.A. 2005. Remote sensing of stream depths with hydraulically assisted bathymetry (HAB) models. *Geomorphology*, **72**: 320-339.

Hazlinsky, E. J.; Snyder, N.P., 2007. Documenting 20th century changes in river morphology using aerial photographs and field surveys; Narraguagus and Sheepscot rivers, Maine. *Abstracts with Programs-Geological Society of America*, **39** (1): 44.

Hedger, R.D., Dodson, J.J., Bourque, J-F., Bergeron, N.E., Carbonneau, P.E. 2006. Improving models of juvenile Atlantic salmon habitat use through high resolution remote sensing. *Ecological Modelling*, **197**: 505-511.

Hubbard, Lucius Lee. *Hubbard's Guide to Moosehead Lake and northern Maine*. Boston: A. Williams and Co., 1882. 206 p.

Irland, L.C., 1998, Maine's forest area, 1600-1995: Review of available estimate. College of Natural Sciences, Forestry, and Agriculture, University of Maine, *Maine Agricultural and Forest Experiment Station Miscellaneous Publication* 736, 12 p.

Johnston, R.A. 2009. The Geology of Gulf Hagas, Bowdoin College Grant East, Maine, http://www.maine.gov/doc/nrimc/mgs/site.htm. Accessed 15 November 2009.

Kim, M., and LaPointe, M. 2011. Regional variability in Atlantic salmon (*Salmo salar*) riverscapes: a simple landscape ecology model explaining the large variability in size of salmon runs across Gaspé watersheds, Canada. *Ecology of Freshwater Fish*, **20**: 144–156.

Kondolf, G.M., Lisle T.E. and Wolman, M.G. 2003. Bed sediment measurement. In: Kondolf GM, Piégay H. *Tools in Fluvial Geomorphology*. John Wiley and Sons, Chichester.

Kondolf, G.M., and Wolman, M.G., 1993. The sizes of salmonid spawning gravels, *Water Resources Research*, **29**: 2275-2285.

Knighton, A.D., 1998. *Fluvial Forms and Processes: A New Perspective*, Arnold, London, 383 p.

Leopold, L.B., and Wolman, M.G., Miller J.P. 1964. *Fluvial Processes in Geomorphology*. W.H. Freeman and Company: San Francisco, 522 p.

Leopold, L. B. 1994. A view of the river. Harvard University Press, Cambridge.

Legleiter, C.J., Roberts, D.A., Marcus, W.A., Fonstad, M.A. 2004. Passive optical remote sensing of river channel morphology and in-stream habitat: Physical basis and feasibility. *Remote Sensing of Environment*, **93**: 493-510.

Lisles, G., 2000. Wild Atlantic salmon in Maine protected as endangered species, NOAA National Fish and Wildlife Service 2000-1113, http://www.publicaffairs.noaa.gov/releases2000/nov00/noaanfws1113.html

Lisle, T.E., Nelson, J.M., Pitlick, J., Madej, M.A., and Barkett, B.L. 2000. Variability of bed mobility in natural, gravel-bed channels and adjustments to sediment load at local and reach scales. *Water Resour. Res.*, **36**:(12), doi:10.1029/2000WR900238.

Magilligan, F.J., Nislow, K.H., Fisher, G.B., Wright, J., Mackey, G. and Laser, M., 2008. The geomorphic function and characteristics of large woody debris in low gradient rivers, coastal Maine, USA. *Geomorphology*, **97**: 467-482.

Maine Geological Survey. 2005. The Iron Age of Maine – 1800s – Katahdin Iron Works. State of Maine Department of Conservation. http://www.maine.gove/doc/nrimc/mgs/explore/mining/sites/sept03.htm Accessed 1 Feb. 2011.

Maine Historical Society. 2011. Image numbers: 15384, 23293, 23292. http://www.mainememory.net/item/15384, 23293, 23292. Accessed 1 Feb. 2011.

Massachusetts Division of Fisheries and Wildlife (MDFW). 2007. Life cycle of the Atlantic salmon. Massachusetts Department of Fish and Game. http://www.mass.gov/dfwele/dfw/fisheries/anadromous/salmon_life_cycle.htm. Accessed 28 March 2011.

Millar, R. G. 2005. Theoretical regime equations for mobile gravel-bed rivers with stable banks. *Geomorphology*, **67**: 204– 220.

Montgomery, D.R., Buffington, J.M., 1997. Channel-reach morphology in mountain drainage basins, *GSA Bulletin*, 109, no. 5, 596-611.

Montgomery, D.R., Buffington, J.M., 1998, Channel processes, classification, and response, *in* Naiman, R. and Bilby, R., eds., River Ecology and Management: Lessons from the Pacific Coastal Ecoregion: New York, Springer-Verlag, p. 13-42.

Montgomery, D.R., Beamer, E.M., Pess, G.R., Quinn, T.P., 1999. Channel type and salmonid spawning distribution and abundance, *Can. J. Fish. Aquat. Sci.*, **56**: 377-387.

Montgomery, D.R. 2003. King of Fish: The Thousand-year Run of Salmon. Westview Press, Boulder, CO. 290 p.

Montgomery, D.R. 2004. Geology, Geomorphology, and the restoration ecology of salmon. *GSA Today,* **14**: 4-12.

Mount, J., 1995. California Rivers and Streams: The conflict between fluvial process and land use. University of California Press, 376 p.

National Research Council, Committee on Atlantic Salmon in Maine. 2004. *Atlantic salmon in Maine*, 304 p., National Academic Press (PDF). http://www.nap.edu/catalog/10892.html.

NOAA. 2011. NOAA Fisheries Service: Atlantic Salmon recovery program. http://www.nero.noaa.gov/prot_res/altsalmon/. Accessed 28 March 2011.

Neeson, T.M, Koonce, J.F., Whiting, P.J. 2007. Predicting sea lamprey (Petromyzon marinus) ammocoete habitat using Geographic Information Systems. *J. Great Lakes Res.,* **33**:546–553.

Parker, G. 1979. Hydraulic geometry of active gravel rivers, *J. Hydraul. Div. Am. Soc. Civ. Eng*., **105** (HY9): 1185-1201.

Parker, G., P. R. Wilcock, C. Paola, W. E. Dietrich, and J. Pitlick. 2007. Physical basis for quasi-universal relations describing bankfull hydraulic geometry of single-thread gravel bed rivers, *J. Geophys. Res.*, **112**: F04005, doi:10.1029/2006JF000549.

Penobscot River Restoration Trust (PRRT). Timeline. 2011. http://penobscotriver.org/. Accessed 30 May 2011.

Pess, G.R., Montgomery, D.R., Steel, E.A., Bilby, R.E., Feist, B.E., Greenberg, H.M. 2002. Landscape characteristics, land use, and coho salmon (Oncorhynchus kisutch) abundance, Snohomish River, Wash., U.S.A. *Can. J. Fish. Aquat. Sci.*, **59**: 613-623.

Piegay, H., Thevenet, A., Kondolf, G.M. and Landon, N., 2000. Physical and human factors influencing potential fish habitat distribution along a mountain river, France. *Geogr. Ann*., **82**: 121–136.

Rice, S.P., and Church, M. 1998. Grain size along two gravel-bed rivers: statistical variation, spatial pattern and sedimentary links. *Earth Surf. Process. Landforms,* **23**: 345–363.

Schnitker, D., Belknap, D.F., Bacchus, T.S., Friez, J.K., Lusardi, B.A., Popek, D.M. 2001. Deglaciation of the Gulf of Maine, *in* Weddle, T.K., and Retelle, M.J., eds., Deglacial History and Relative Sea-Level Changes, Northern New England and Adjacent Canada; Boulder, Colorado. Geological Society of America Special Paper 351: 9-34.

Shangraw, S.J. 2005. Little Lyford Pond Camps: From Frontier Logging to Backcountry Bliss at a Traditional Sporting Camp. Appalachia. http://www.outdoors.org/publications/appalachia/2005/2005-little-lyford-pond-camps.cfm. (Cached version dated 1 Feb. 2011). Accessed 9 Feb. 2011.

Slaymaker, O. 2009. Proglacial, periglacial or paraglacial? *Geological Society, London, Special Publications*, **320**: 71 - 84.

Snyder, N.P., Whipple, K.X., Tucker, G.E., Merritts, D.J. 2000. Landscape response to tectonic forcing: Digital elevation model analysis of stream profiles in the Mendocino triple junction region, northern California. *GSA Bulletin*, **112**: 1250–1263.

Snyder, N.P., Whipple, K.X., Tucker, G.E., Merritts, D.J. 2003. Channel response to tectonic forcing: field analysis of stream morphology in the Mendocino triple junction region, northern California. *Geomorphology*, **53**: 97-127. doi: 10.1016/S0169-555X(02)00349-5.

Snyder, N.P., Castele, M.R., Wright JR. 2008. Bedload entrainment in low-gradient paraglacial coastal rivers of Maine, U.S.A.: Implications for habitat restoration. *Geomorphology*, **103**: 430-446.

Snyder, N.P. 2009. Studying stream morphology with airborne laser elevation data. *Eos,* **90** (6): 45-46.

Strouse, S. 2010. Controls on legacy sediment mobility in a post-glaciated, low-gradient river. *M.S. thesis in prep*.

Thompson, W.B., and Borns, H.W., Jr. (editors). 1985. Surficial geologic map of Maine: Maine Geological Survey (Department of Conservation). scale 1:500,000.

US Fish and Wildlife Service (USFWS), Gulf of Maine Coastal Program (GOMP), 2006. Atlantic Salmon Habitat Survey (ashab3). Office of Geographic Information Systems (MEGIS), Augusta, ME. http://megis.maine.gov/catalog/.

U.S. Geological Survey (USGS). 2009. Real-Time Water Data for USA. http://waterdata.usgs.gov. Accessed 13 Dec. 2009.

Wilkins, B.C. 2009. Geomorphic comparison of two Atlantic coastal streams: Jacquet River, New Brunswick, Canada, and Narraguagus River, Maine, USA. *College Dissertations and Theses.*

Wilkins, B. C. and Snyder, N. P. 2011, Geomorphic comparison of two Atlantic coastal rivers: Toward an understanding of physical controls on Atlantic salmon habitat. *River Research and Applications*, **27**: 135–156. doi: 10.1002/rra.1343.

Wilson, J.S. 2005. Nineteenth-century lumber surveys for Bangor, Maine: Implications for pre-European settlement forest characteristics in northern and eastern Maine. *Journal of Forestry*, 218-223.

Wolman, M.G. 1954. A method of sampling coarse river-bed material. *Eos, Transactions, American Geophysical Union*, **35**: 951-956.

Wolman, M. G., and Miller, J. P. (1960). Magnitude and frequency of forces in geomorphic processes. *Journal of Geology*, **68**: 54–74.

Appendix

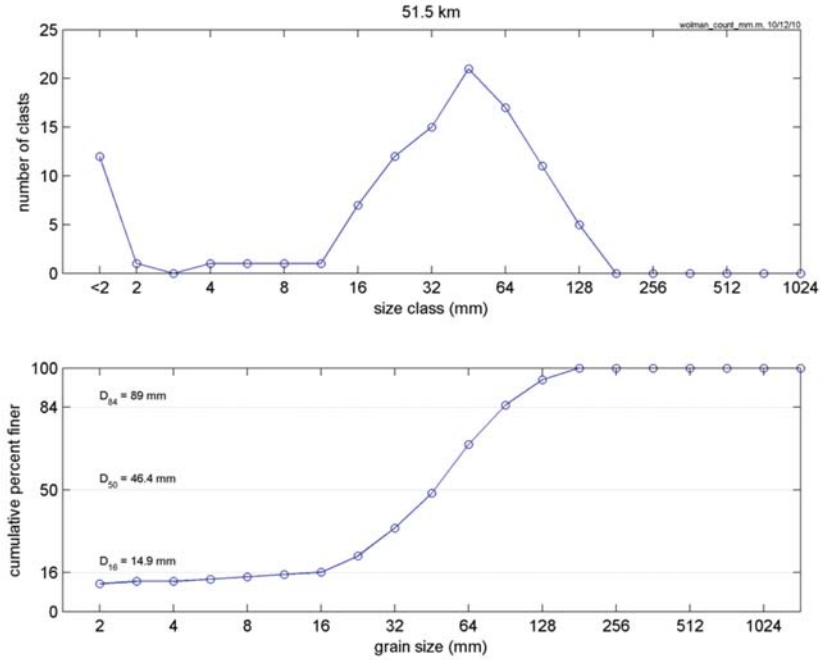
51.5 km
wolman_count_mm.m, 10/12/10
number of clasts
size class (mm)
<2
2
4
8
16
32
64
128
256
512
1024
cumulative percent finer
grain size (mm)
D84 = 89 mm
D50 = 46.4 mm
D16 = 14.9 mm

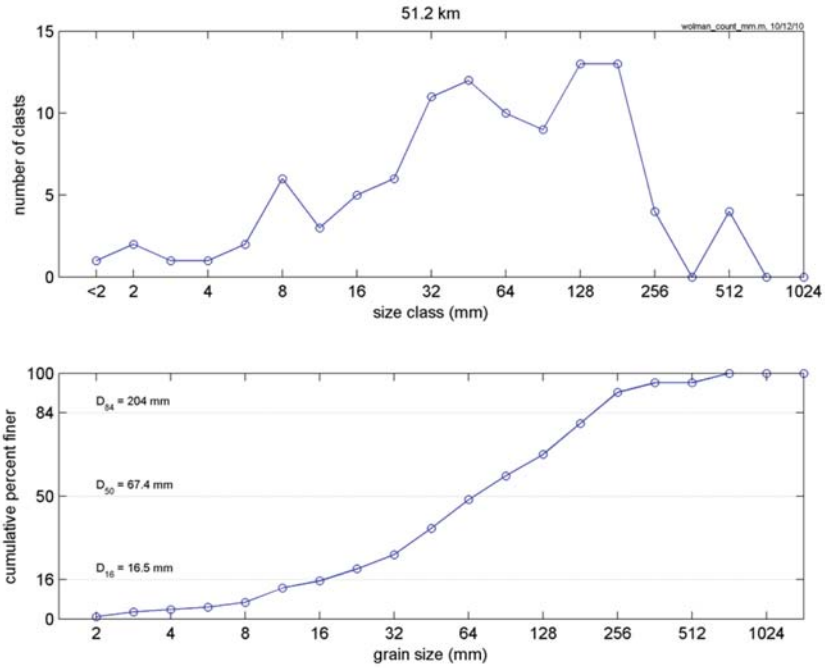
51.2 km
wolman_count_mm.m, 10/12/10
number of clasts
size class (mm)
<2
2
4
8
16
32
64
128
256
512
1024
cumulative percent finer
grain size (mm)
D84 = 204 mm
D50 = 67.4 mm
D16 = 16.5 mm

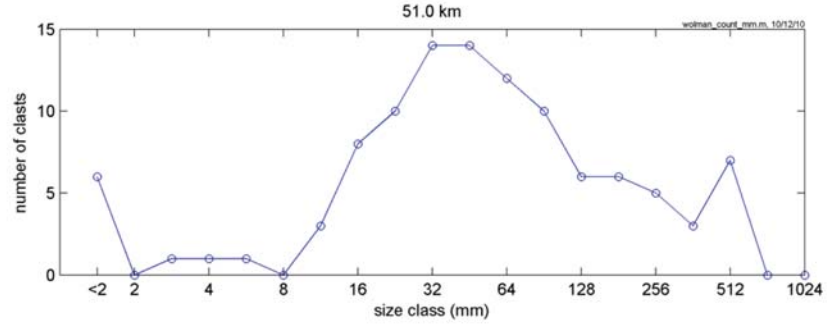
51.0 km
wolman_count_mm.m, 10/12/10
number of clasts
size class (mm)
<2
2
4
8
16
32
64
128
256
512
1024

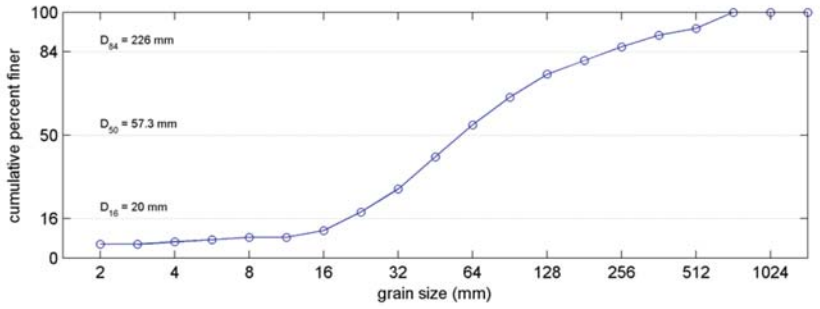
cumulative percent finer
grain size (mm)
D84 = 226 mm
D50 = 57.3 mm
D16 = 20 mm

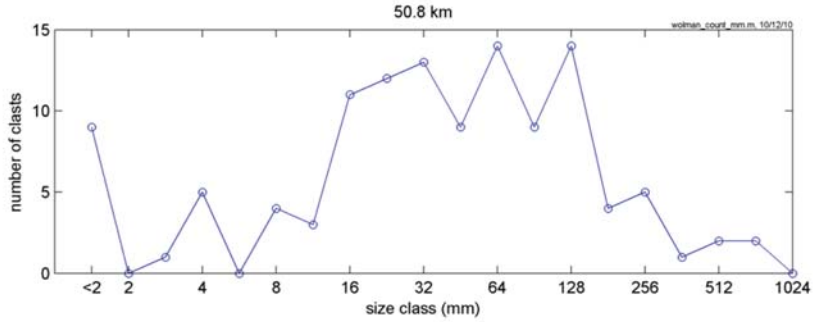
50.8 km
wolman_count_mm.m, 10/12/10
number of clasts
size class (mm)

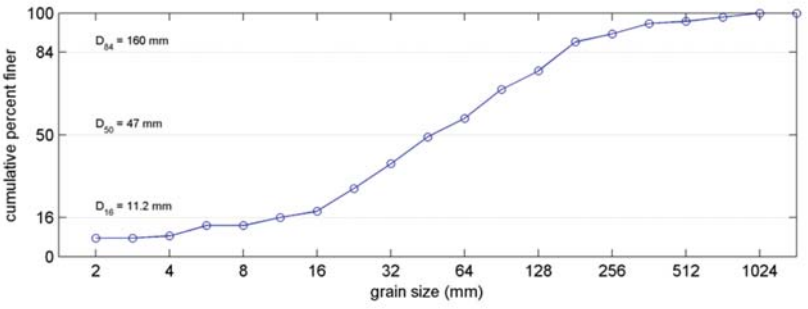
cumulative percent finer
grain size (mm)
D84 = 160 mm
D50 = 47 mm
D16 = 11.2 mm

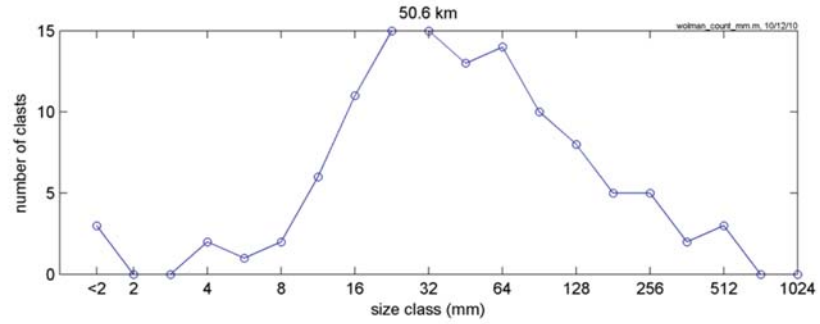
50.6 km
wolman_count_mm.m, 10/12/10
number of clasts
size class (mm)
<2
2
4
8
16
32
64
128
256
512
1024

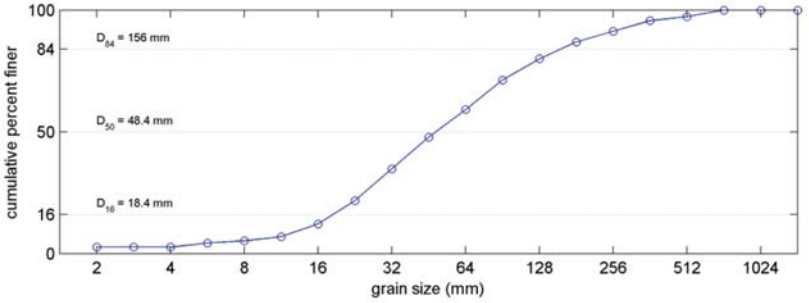
cumulative percent finer
grain size (mm)
D84 = 156 mm
D50 = 48.4 mm
D16 = 18.4 mm

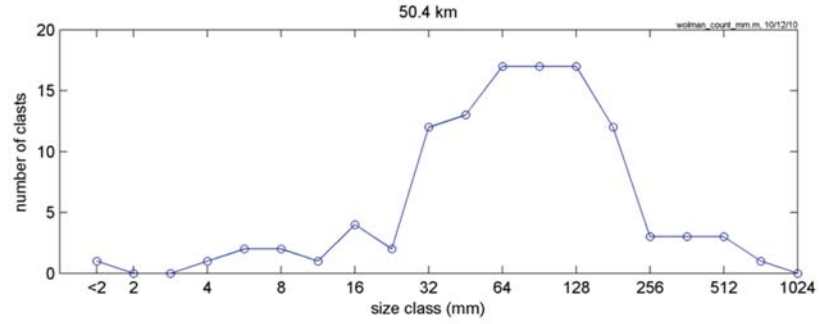
50.4 km
wolman_count_mm.m, 10/12/10
number of clasts
size class (mm)
<2
2
4
8
16
32
64
128
256
512
1024

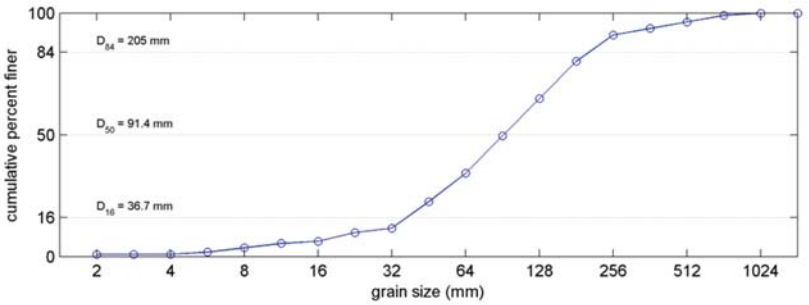
cumulative percent finer
grain size (mm)
D84 = 205 mm
D50 = 91.4 mm
D16 = 36.7 mm

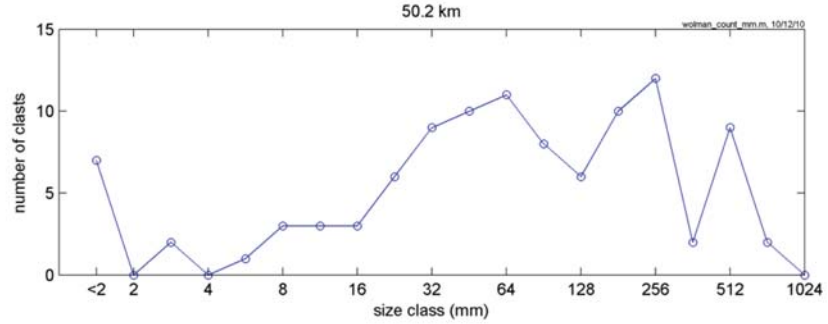
50.2 km
wolman_count_mm.m, 10/12/10
number of clasts
size class (mm)
<2
2
4
8
16
32
64
128
256
512
1024

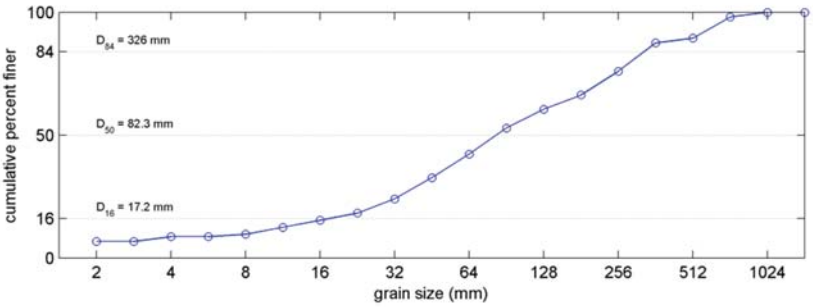
cumulative percent finer
grain size (mm)
D84 = 326 mm
D50 = 82.3 mm
D16 = 17.2 mm

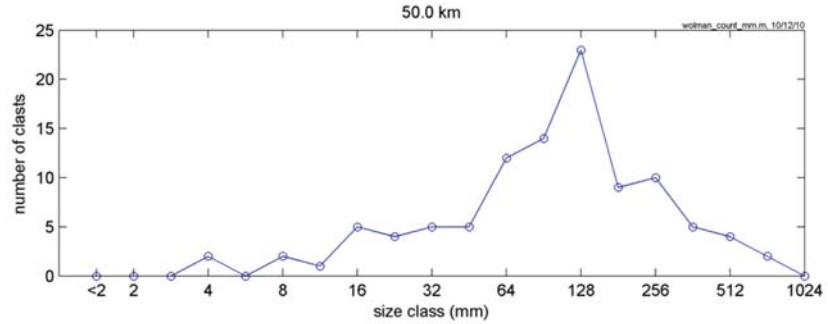
50.0 km
wolman_count_mm.m, 10/12/10
number of clasts
size class (mm)
<2
2
4
8
16
32
64
128
256
512
1024

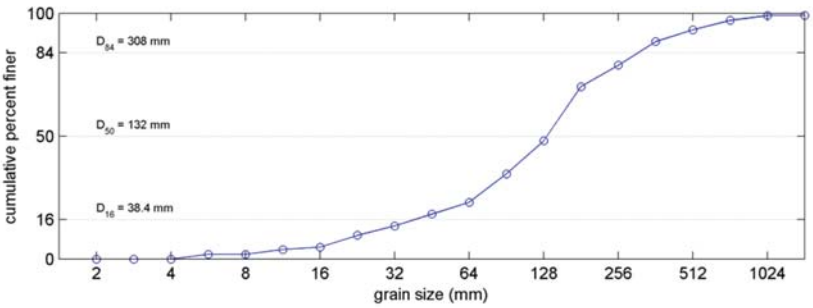
cumulative percent finer
grain size (mm)
D84 = 308 mm
D50 = 132 mm
D16 = 38.4 mm

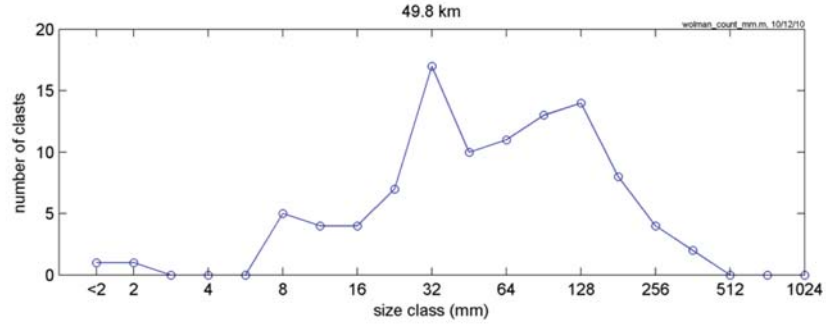
49.8 km
wolman_count_mm.m, 10/12/10
number of clasts
size class (mm)
<2
2
4
8
16
32
64
128
256
512
1024

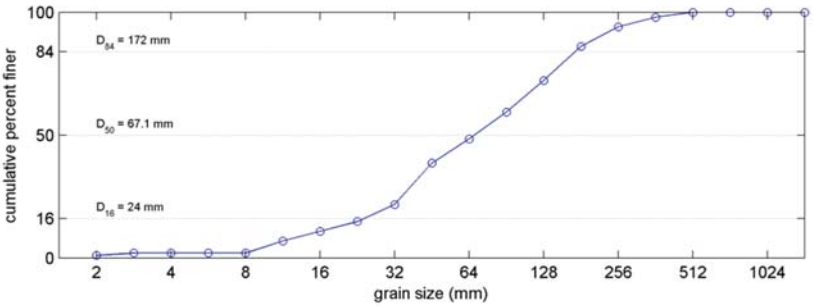
cumulative percent finer
grain size (mm)
D84 = 172 mm
D50 = 67.1 mm
D16 = 24 mm

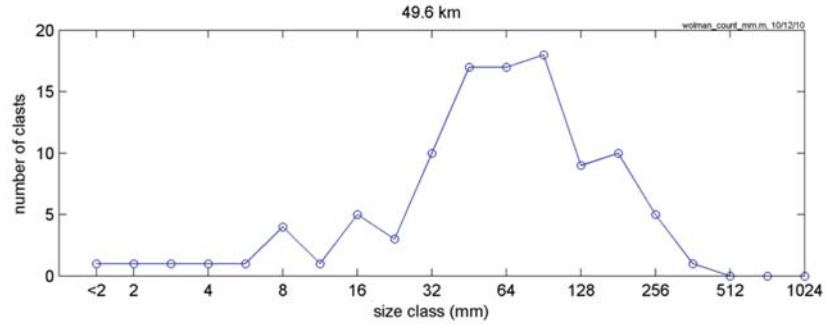
49.6 km
wolman_count_mm.m, 10/12/10
number of clasts
size class (mm)

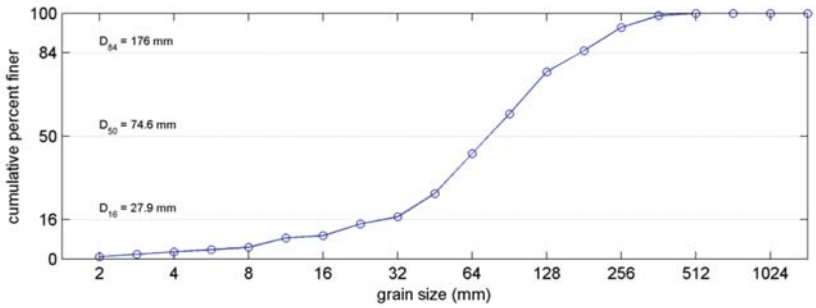
cumulative percent finer
grain size (mm)
D84 = 176 mm
D50 = 74.6 mm
D16 = 27.9 mm

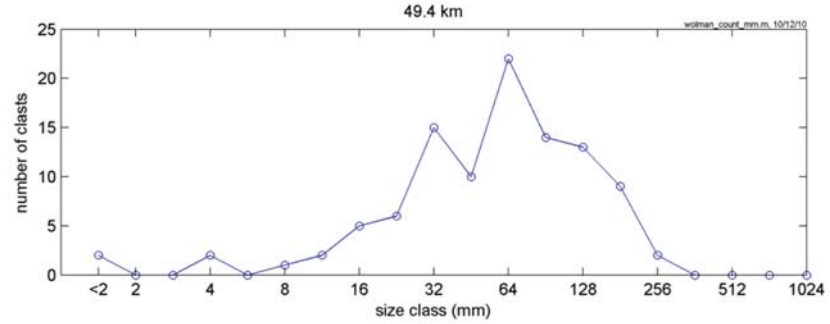
49.4 km
wolman_count_mm.m, 10/12/10
number of clasts
size class (mm)
<2
2
4
8
16
32
64
128
256
512
1024

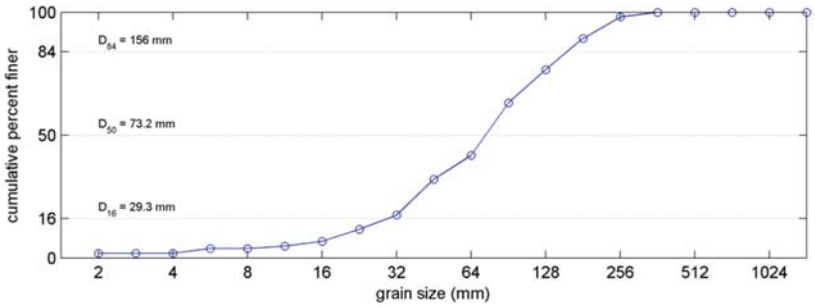
cumulative percent finer
grain size (mm)
D84 = 156 mm
D50 = 73.2 mm
D16 = 29.3 mm

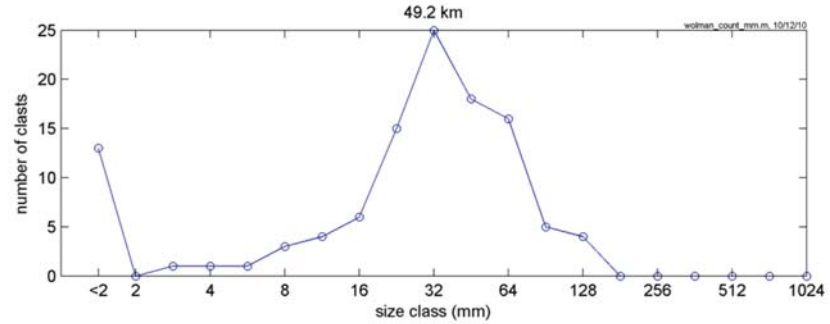
49.2 km
wolman_count_mm.m, 10/12/10
number of clasts
size class (mm)
<2
2
4
8
16
32
64
128
256
512
1024

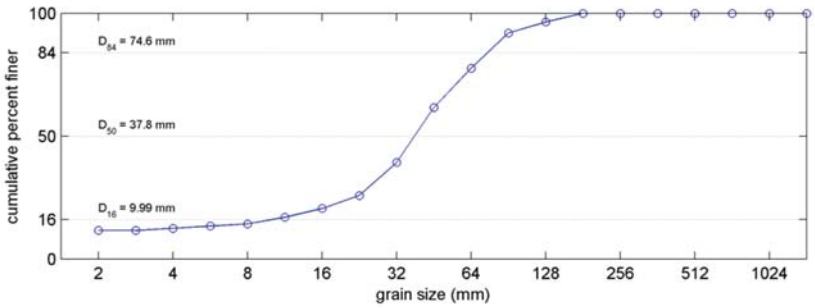
cumulative percent finer
grain size (mm)
D84 = 74.6 mm
D50 = 37.8 mm
D16 = 9.99 mm

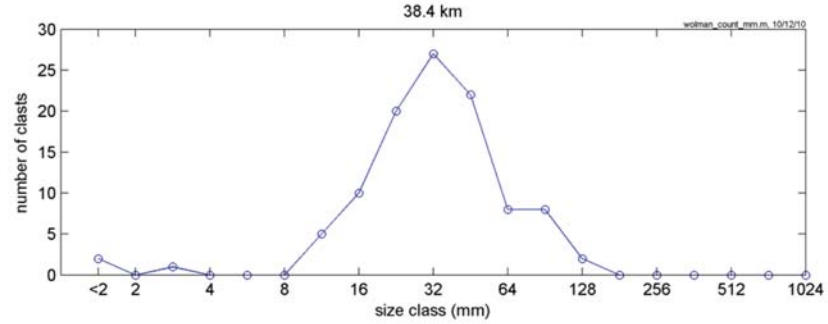
38.4 km
wolman_count_mm.m, 10/12/10
number of clasts
size class (mm)
<2
2
4
8
16
32
64
128
256
512
1024

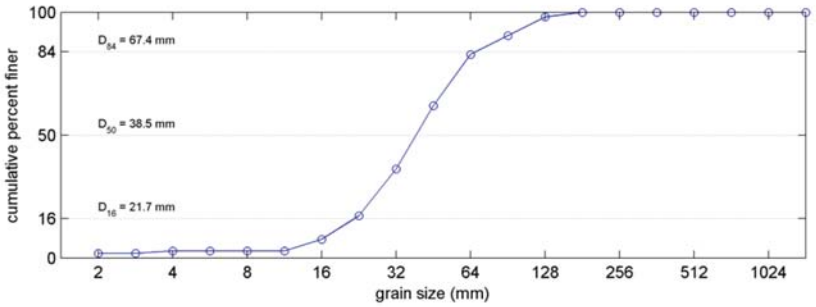
cumulative percent finer
grain size (mm)
D84 = 67.4 mm
D50 = 38.5 mm
D16 = 21.7 mm

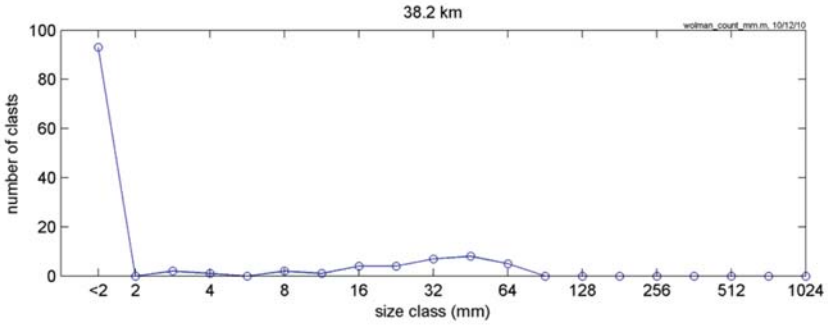
38.2 km
wolman_count_mm.m, 10/12/10
number of clasts
size class (mm)
<2
2
4
8
16
32
64
128
256
512
1024

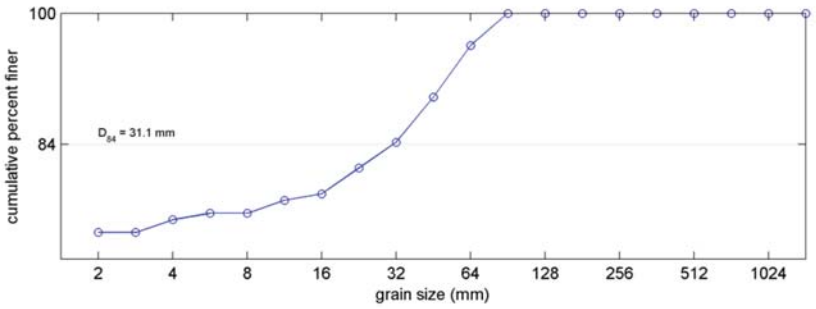
cumulative percent finer
grain size (mm)
D84 = 31.1 mm

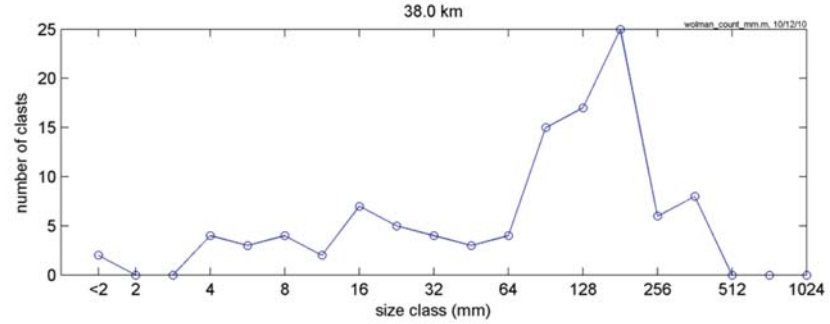
38.0 km
wolman_count_mm.m, 10/12/10
number of clasts
size class (mm)
<2
2
4
8
16
32
64
128
256
512
1024

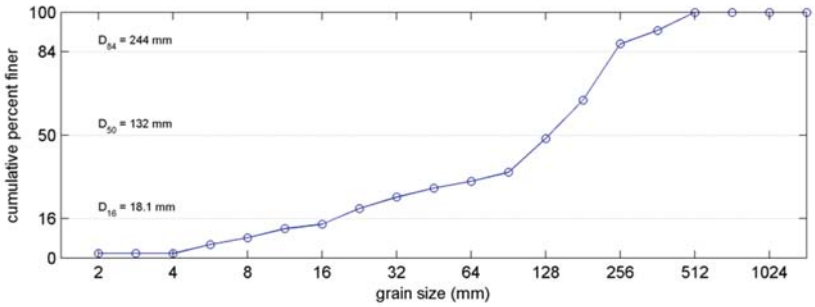
cumulative percent finer
grain size (mm)
D84 = 244 mm
D50 = 132 mm
D16 = 18.1 mm

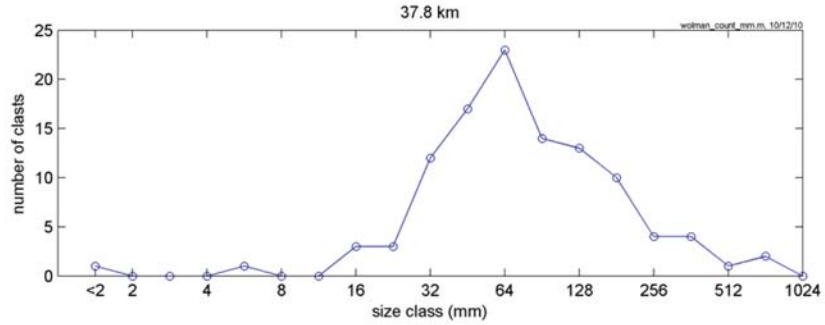
37.8 km
wolman_count_mm.m, 10/12/10
number of clasts
size class (mm)
<2
2
4
8
16
32
64
128
256
512
1024

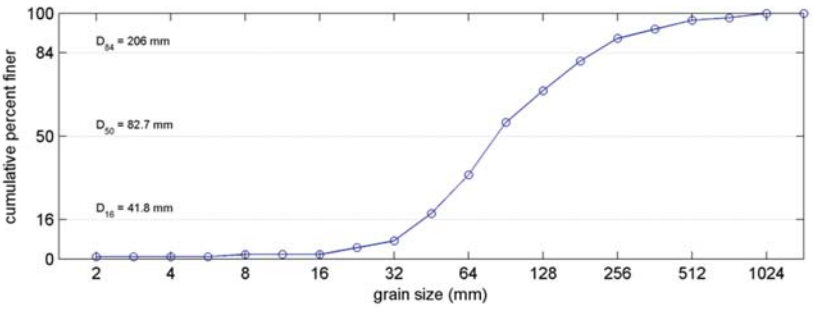
cumulative percent finer
grain size (mm)
D84 = 206 mm
D50 = 82.7 mm
D16 = 41.8 mm

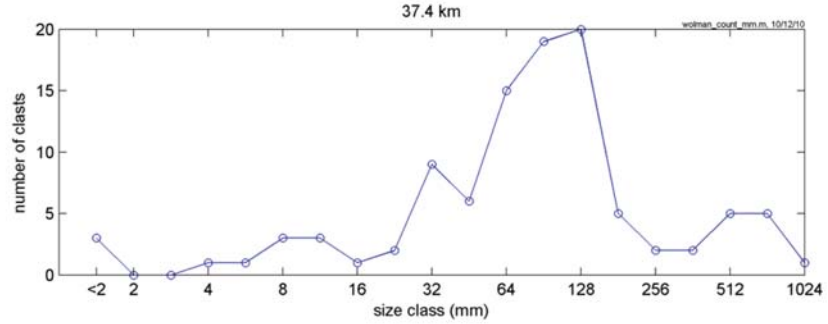
37.4 km
wolman_count_mm.m, 10/12/10
number of clasts
size class (mm)
<2
2
4
8
16
32
64
128
256
512
1024

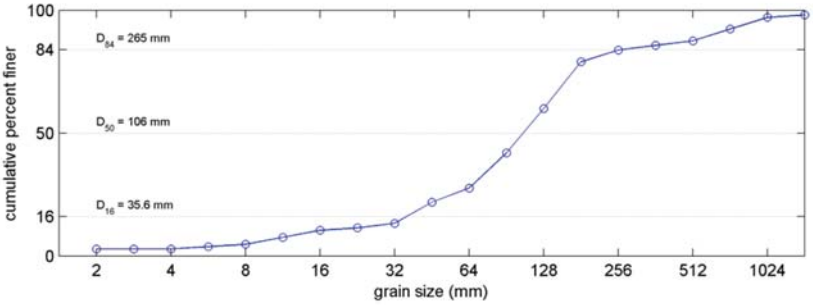
cumulative percent finer
grain size (mm)
D84 = 265 mm
D50 = 106 mm
D16 = 35.6 mm

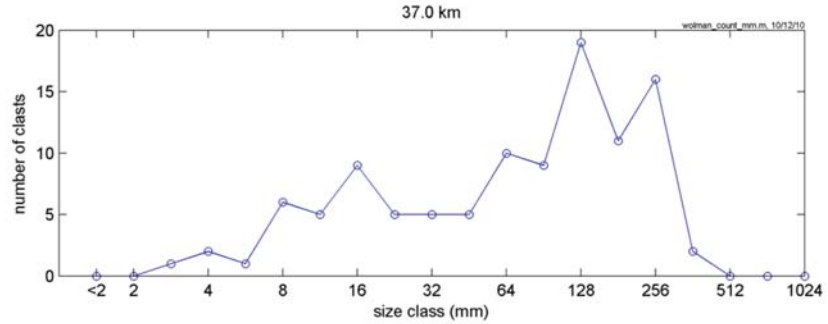
37.0 km
wolman_count_mm.m, 10/12/10
number of clasts
size class (mm)

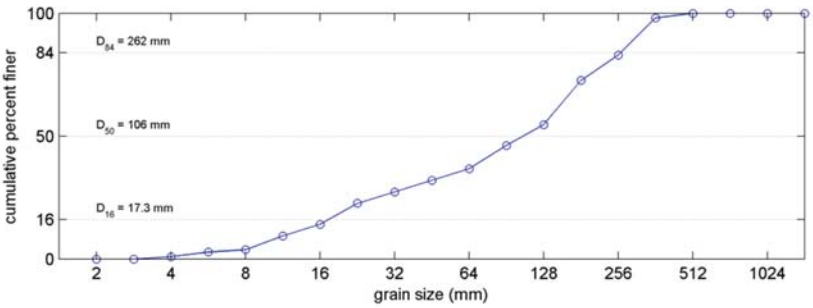
cumulative percent finer
grain size (mm)
D84 = 262 mm
D50 = 106 mm
D16 = 17.3 mm

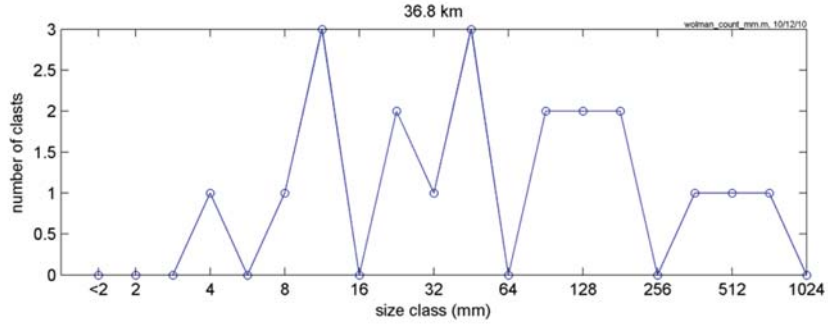
36.8 km
wolman_count_mm.m, 10/12/10
number of clasts
size class (mm)
<2
2
4
8
16
32
64
128
256
512
1024

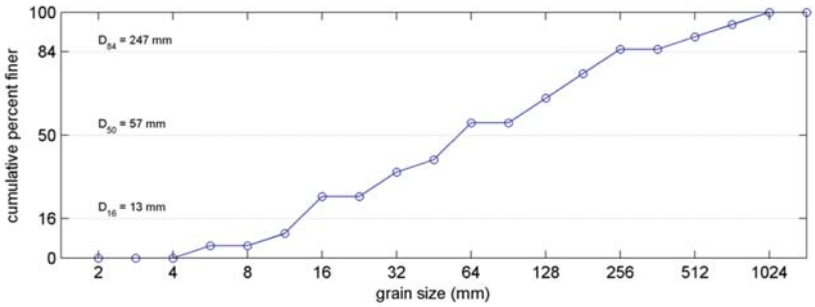
cumulative percent finer
grain size (mm)
D84 = 247 mm
D50 = 57 mm
D16 = 13 mm

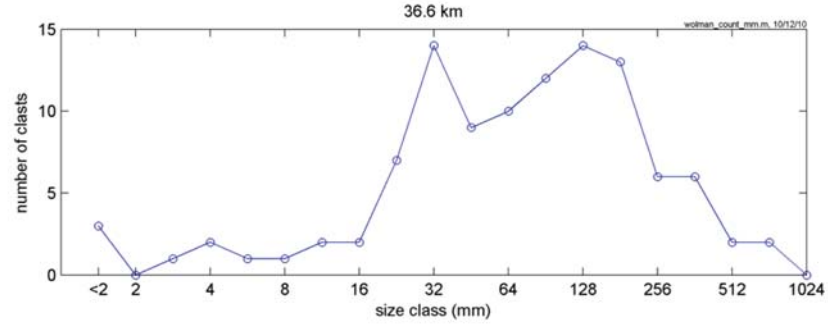
36.6 km
wolman_count_mm.m, 10/12/10
number of clasts
size class (mm)
<2
2
4
8
16
32
64
128
256
512
1024

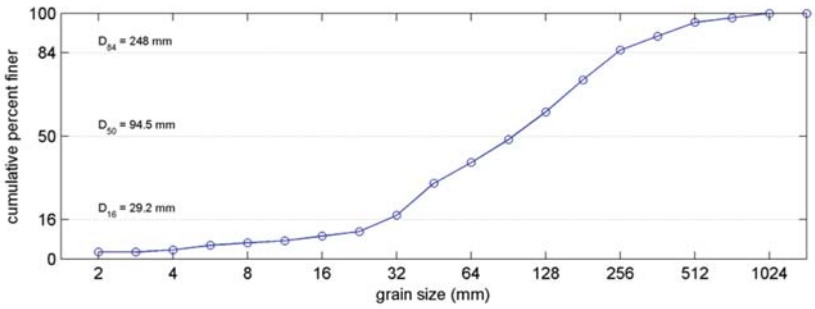
cumulative percent finer
grain size (mm)
D84 = 248 mm
D50 = 94.5 mm
D16 = 29.2 mm

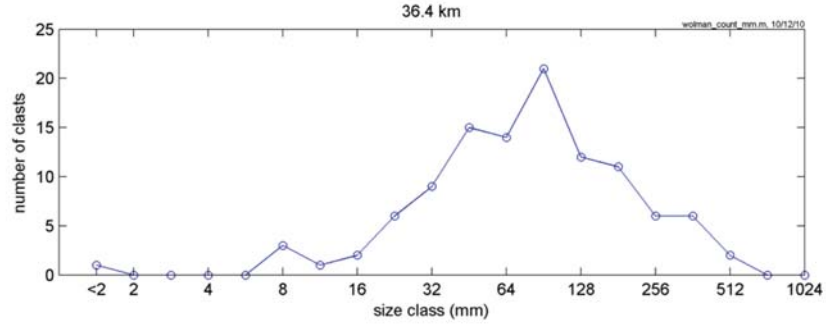
36.4 km
wolman_count_mm.m, 10/12/10
number of clasts
size class (mm)
<2
2
4
8
16
32
64
128
256
512
1024

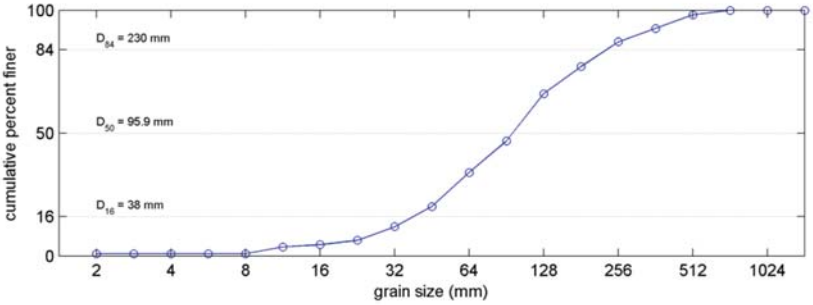
cumulative percent finer
grain size (mm)
D84 = 230 mm
D50 = 95.9 mm
D16 = 38 mm

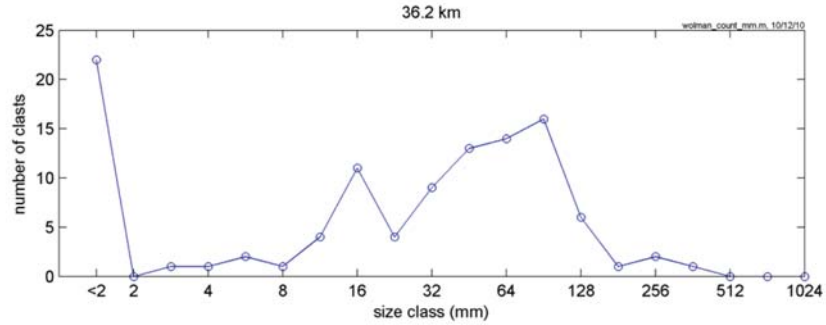
36.2 km
wolman_count_mm.m, 10/12/10
number of clasts
size class (mm)

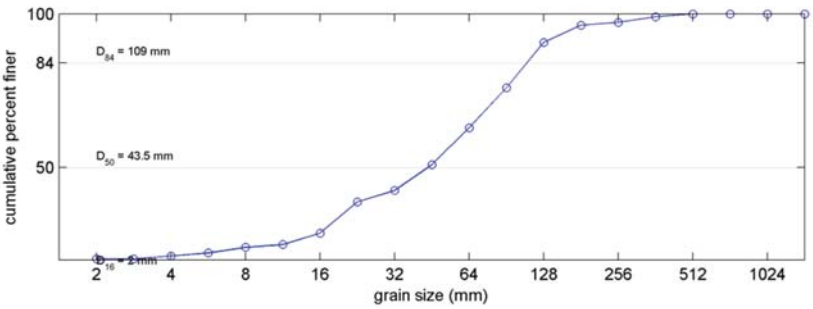
cumulative percent finer
grain size (mm)
D84 = 109 mm
D50 = 43.5 mm

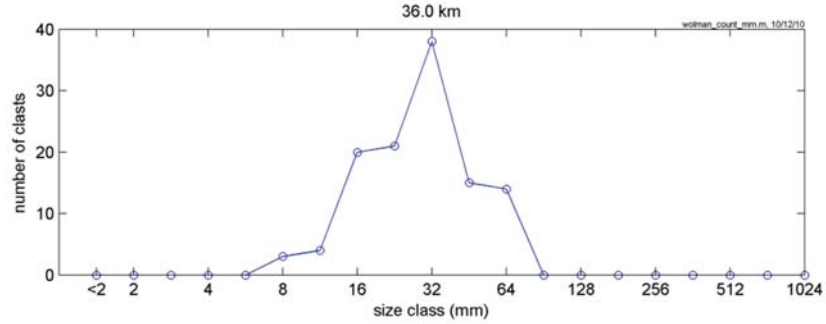
36.0 km
wolman_count_mm.m, 10/12/10
number of clasts
size class (mm)
<2
2
4
8
16
32
64
128
256
512
1024

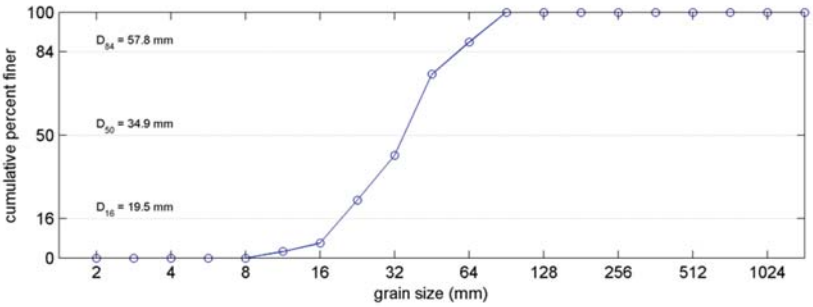
cumulative percent finer
grain size (mm)
D84 = 57.8 mm
D50 = 34.9 mm
D16 = 19.5 mm

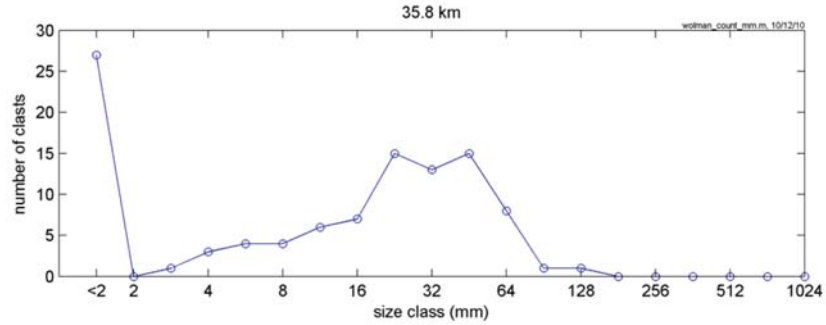
35.8 km
wolman_count_mm.m, 10/12/10
number of clasts
size class (mm)

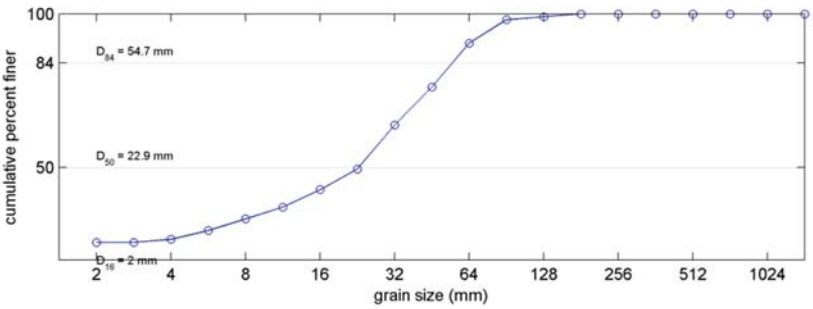
cumulative percent finer
grain size (mm)
D84 = 54.7 mm
D50 = 22.9 mm
D16 = 2 mm

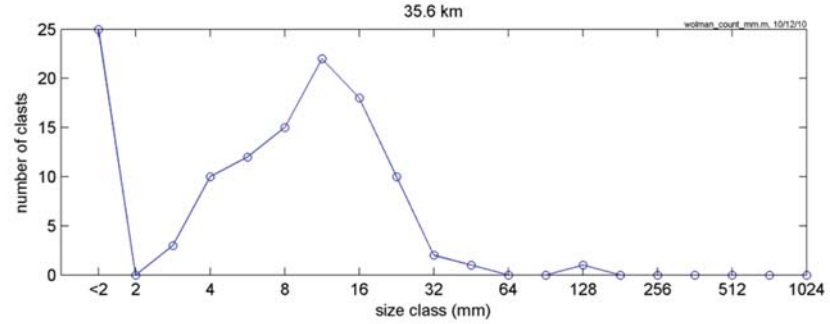
35.6 km
wolman_count_mm.m, 10/12/10
number of clasts
size class (mm)
<2
2
4
8
16
32
64
128
256
512
1024

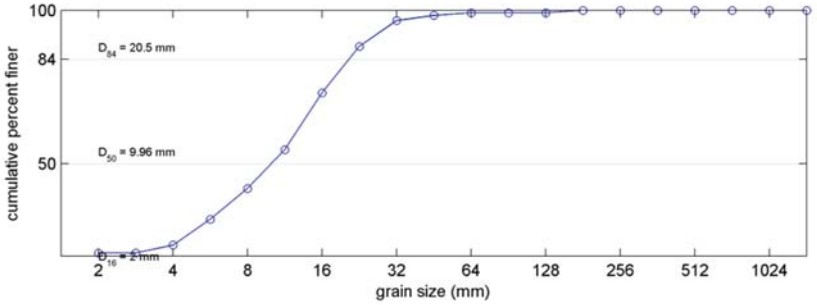
cumulative percent finer
grain size (mm)
D84 = 20.5 mm
D50 = 9.96 mm
D16 = 2 mm

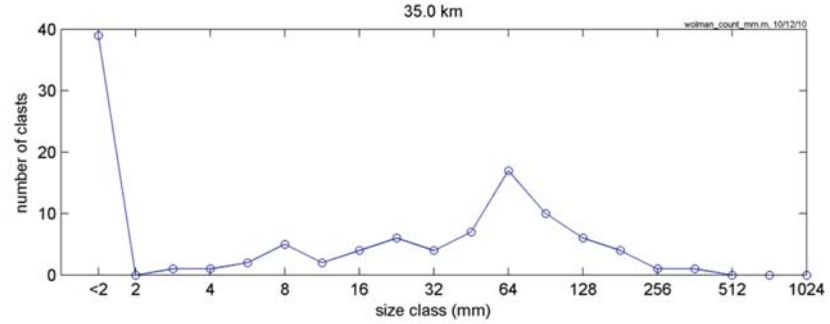
35.0 km
wolman_count_mm.m, 10/12/10
number of clasts
size class (mm)

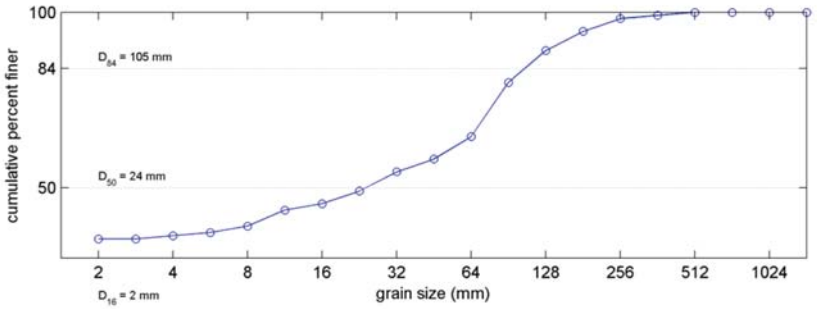
cumulative percent finer
grain size (mm)
D84 = 105 mm
D50 = 24 mm
D16 = 2 mm

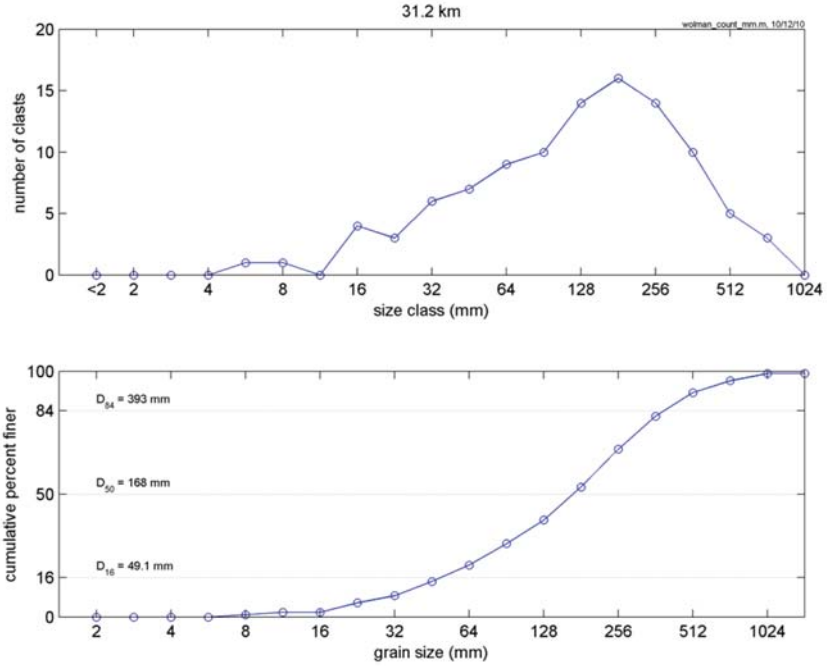
31.2 km
wolman_count_mm.m, 10/12/10
number of clasts
size class (mm)
<2
2
4
8
16
32
64
128
256
512
1024
cumulative percent finer
grain size (mm)
D84 = 393 mm
D50 = 168 mm
D16 = 49.1 mm

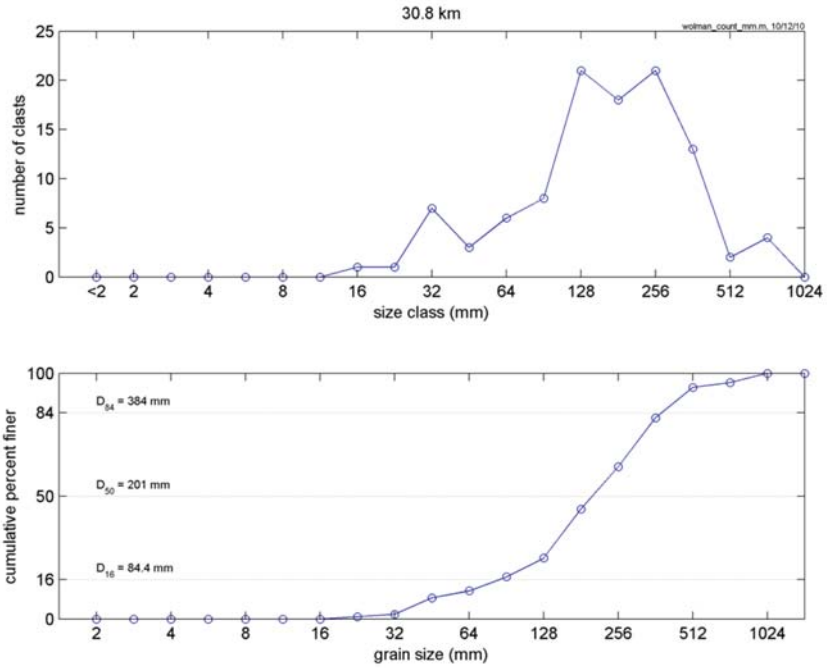
30.8 km
wolman_count_mm.m, 10/12/10
number of clasts
size class (mm)
<2
2
4
8
16
32
64
128
256
512
1024
cumulative percent finer
grain size (mm)
D84 = 384 mm
D50 = 201 mm
D16 = 84.4 mm

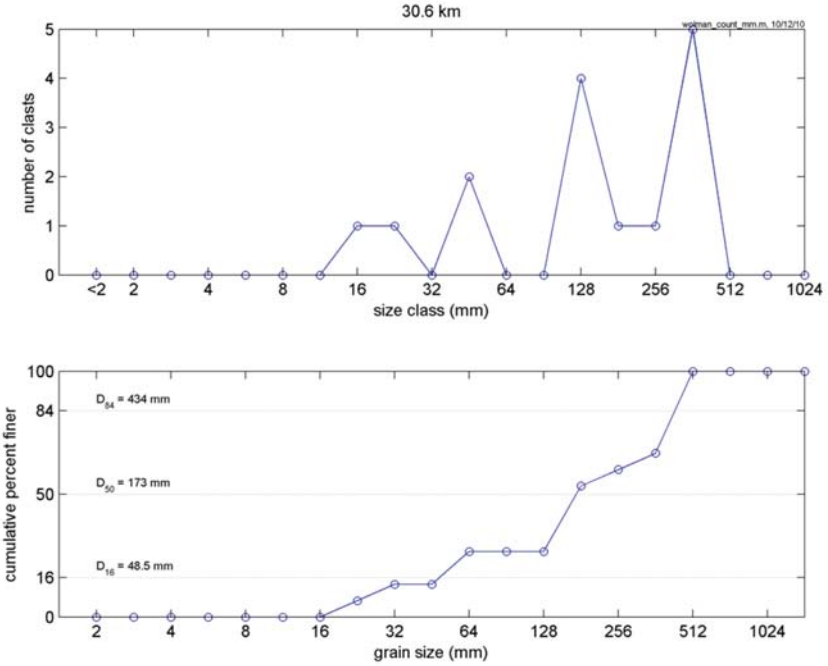
30.6 km
wolman_count_mm.m, 10/12/10
number of clasts
size class (mm)
<2
2
4
8
16
32
64
128
256
512
1024
cumulative percent finer
grain size (mm)
D84 = 434 mm
D50 = 173 mm
D16 = 48.5 mm

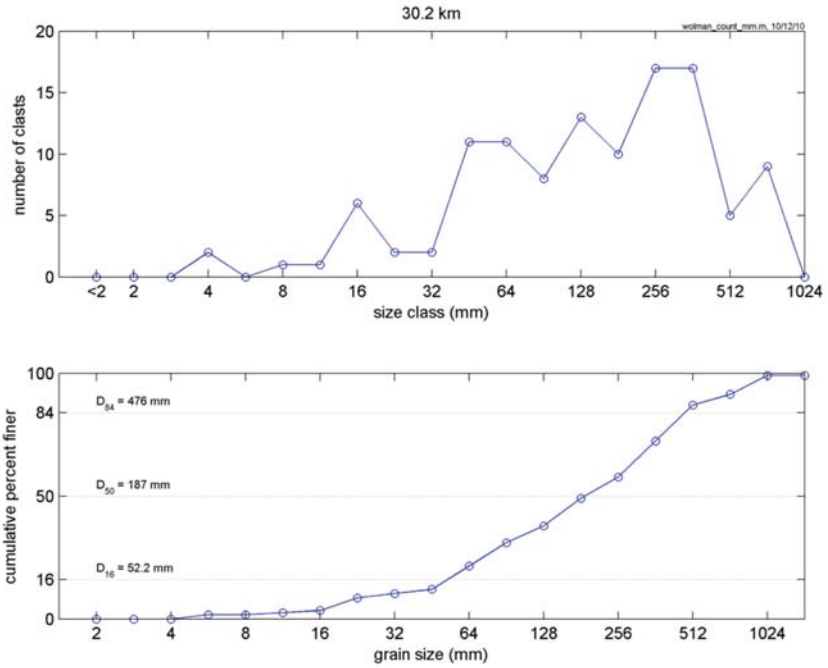
30.2 km
wolman_count_mm.m, 10/12/10
number of clasts
size class (mm)
<2
2
4
8
16
32
64
128
256
512
1024
cumulative percent finer
grain size (mm)
D84 = 476 mm
D50 = 187 mm
D16 = 52.2 mm

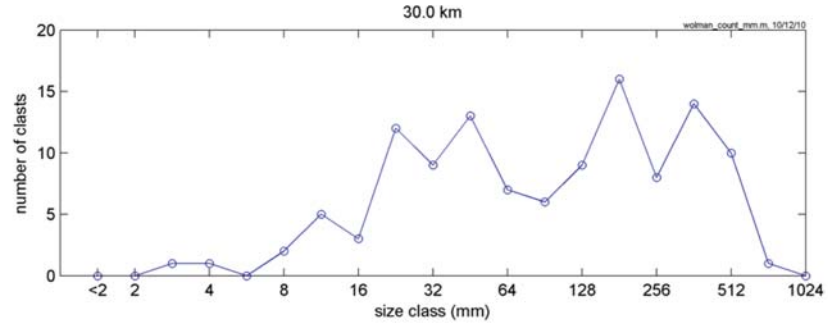
30.0 km
wolman_count_mm.m, 10/12/10
number of clasts
size class (mm)
<2
2
4
8
16
32
64
128
256
512
1024

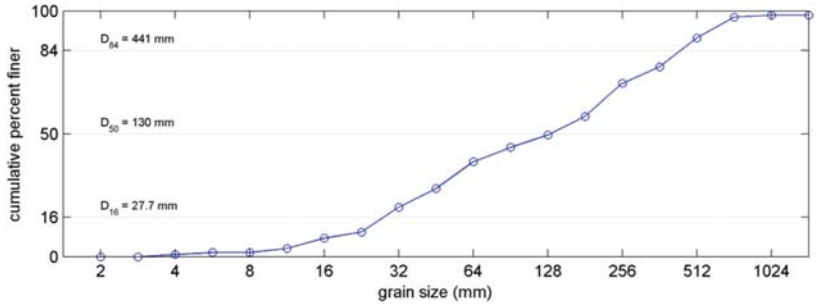
cumulative percent finer
grain size (mm)
D84 = 441 mm
D50 = 130 mm
D16 = 27.7 mm

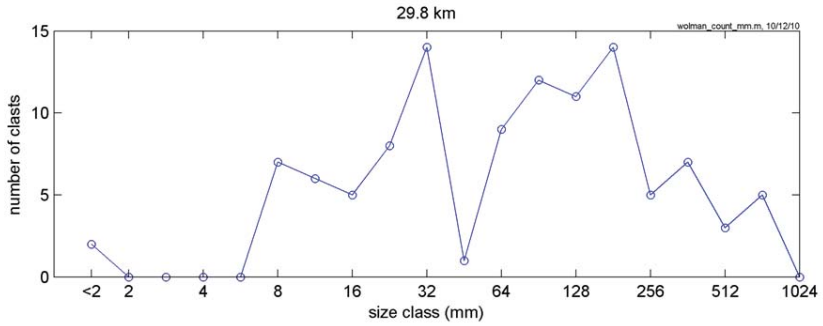
29.8 km
wolman_count_mm.m, 10/12/10
number of clasts
size class (mm)

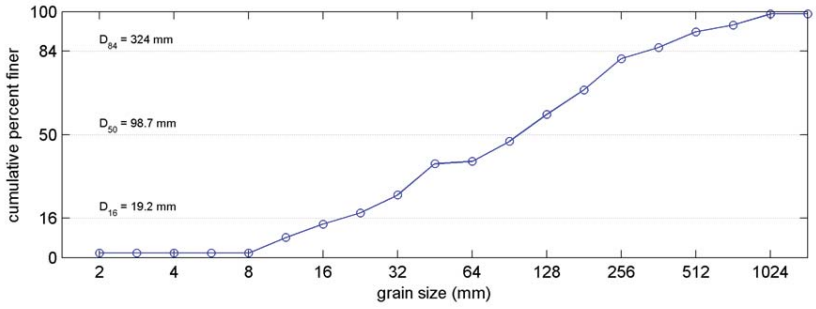
cumulative percent finer
grain size (mm)
D84 = 324 mm
D50 = 98.7 mm
D16 = 19.2 mm

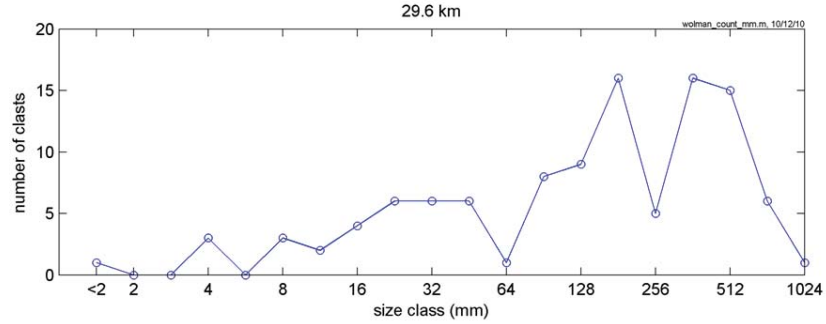
29.6 km
wolman_count_mm.m, 10/12/10
number of clasts
size class (mm)
<2
2
4
8
16
32
64
128
256
512
1024

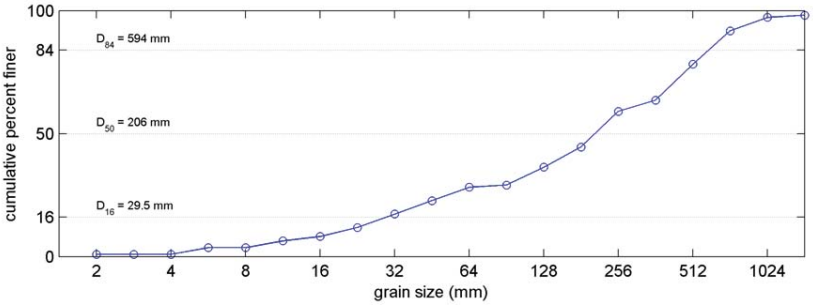
cumulative percent finer
grain size (mm)
D84 = 594 mm
D50 = 206 mm
D16 = 29.5 mm

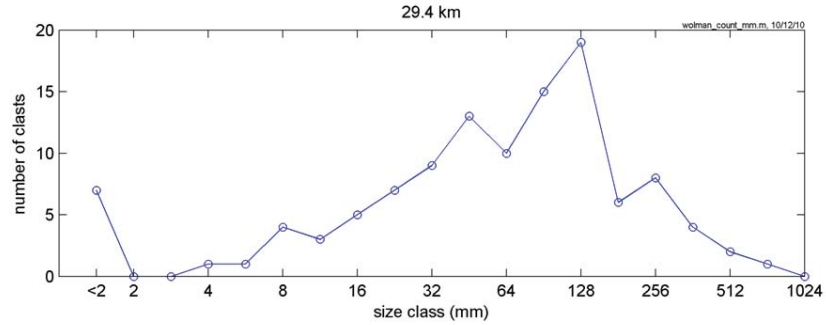
29.4 km
wolman_count_mm.m, 10/12/10
number of clasts
size class (mm)
<2
2
4
8
16
32
64
128
256
512
1024

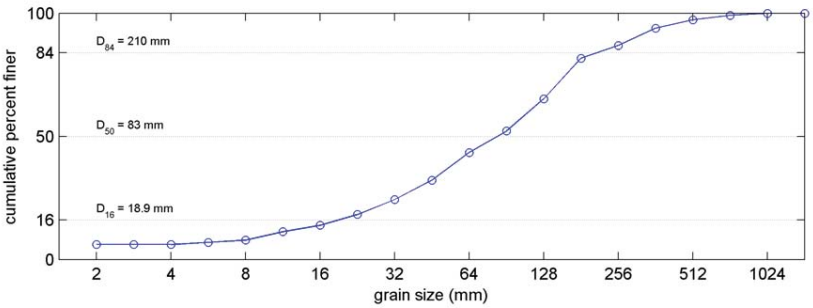
cumulative percent finer
grain size (mm)
D84 = 210 mm
D50 = 83 mm
D16 = 18.9 mm

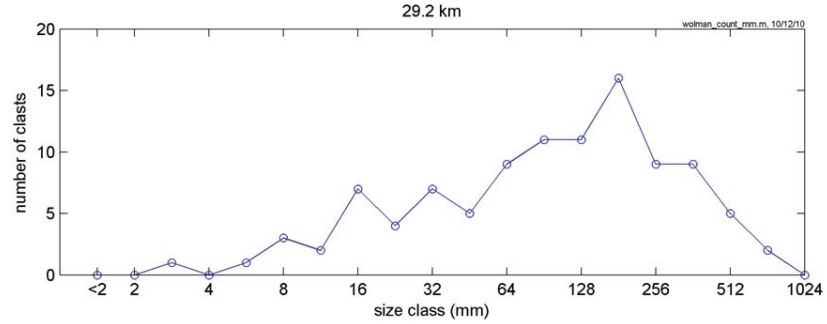
29.2 km
wolman_count_mm.m. 10/12/10
number of clasts
size class (mm)
<2
2
4
8
16
32
64
128
256
512
1024

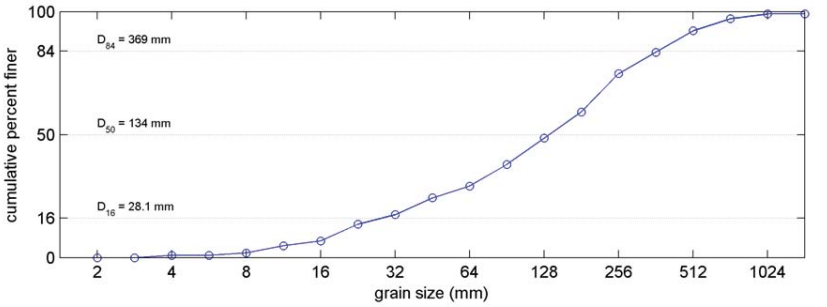
cumulative percent finer
grain size (mm)
D84 = 369 mm
D50 = 134 mm
D16 = 28.1 mm

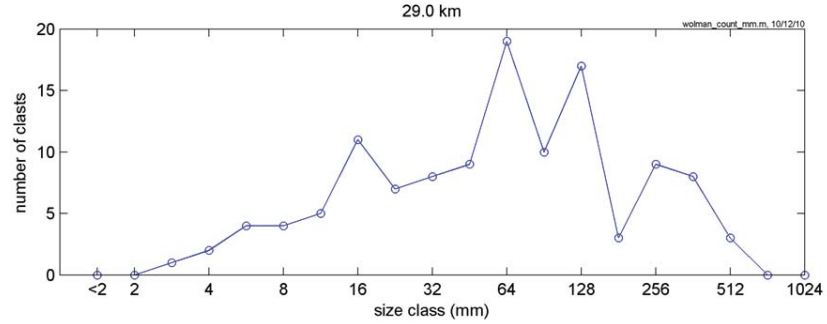
29.0 km
wolman_count_mm.m. 10/12/10
number of clasts
size class (mm)

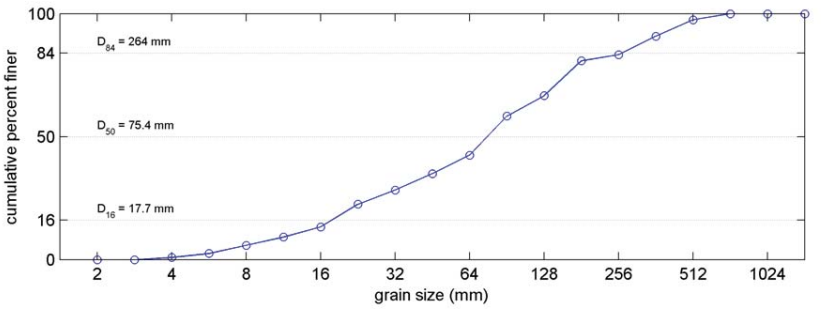
cumulative percent finer
grain size (mm)
D84 = 264 mm
D50 = 75.4 mm
D16 = 17.7 mm

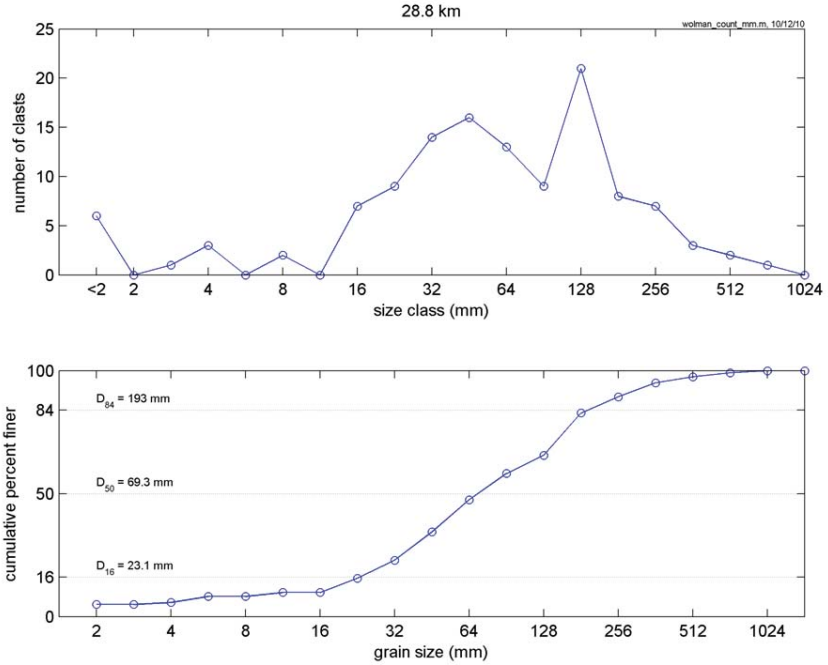
28.8 km
wolman_count_mm.m, 10/12/10
number of clasts
size class (mm)
<2
2
4
8
16
32
64
128
256
512
1024
cumulative percent finer
grain size (mm)
D84 = 193 mm
D50 = 69.3 mm
D16 = 23.1 mm

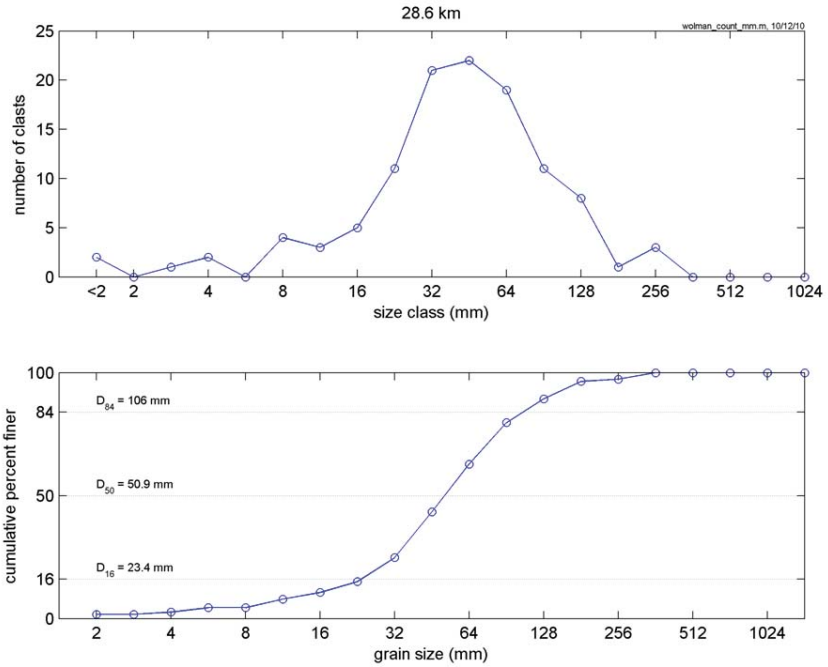
28.6 km
wolman_count_mm.m, 10/12/10
number of clasts
size class (mm)
<2
2
4
8
16
32
64
128
256
512
1024
cumulative percent finer
grain size (mm)
D84 = 106 mm
D50 = 50.9 mm
D16 = 23.4 mm

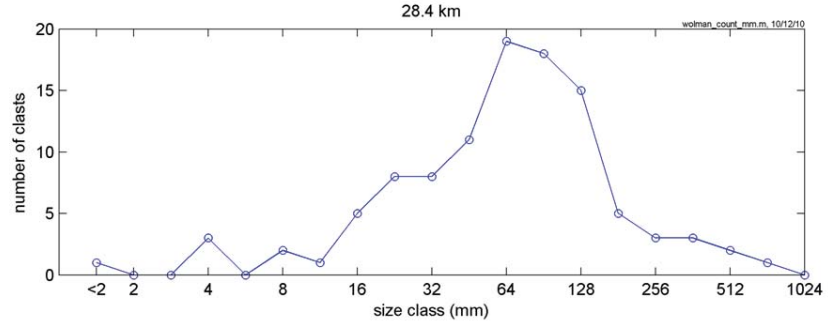
28.4 km
wolman_count_mm.m, 10/12/10
number of clasts
size class (mm)
<2
2
4
8
16
32
64
128
256
512
1024

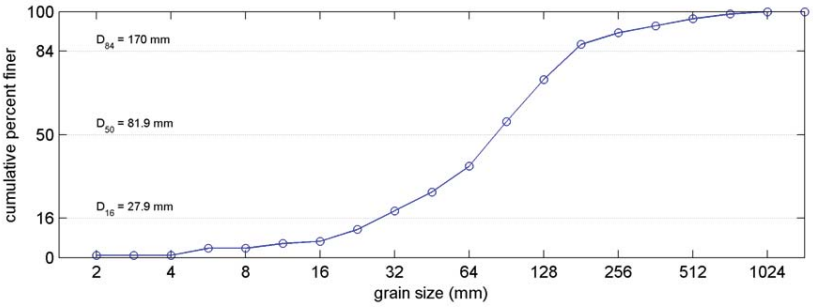
cumulative percent finer
grain size (mm)
D84 = 170 mm
D50 = 81.9 mm
D16 = 27.9 mm

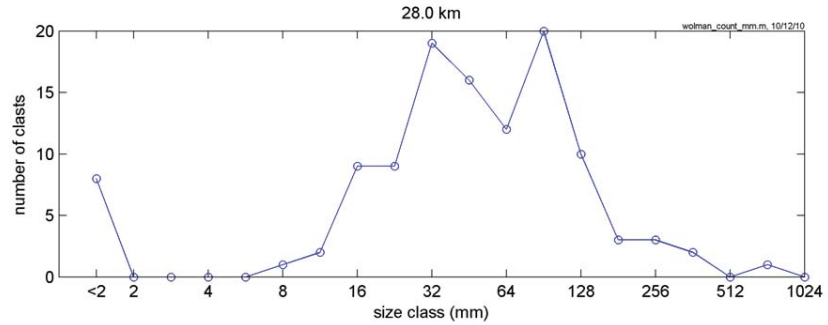
28.0 km
wolman_count_mm.m, 10/12/10
number of clasts
size class (mm)
<2
2
4
8
16
32
64
128
256
512
1024

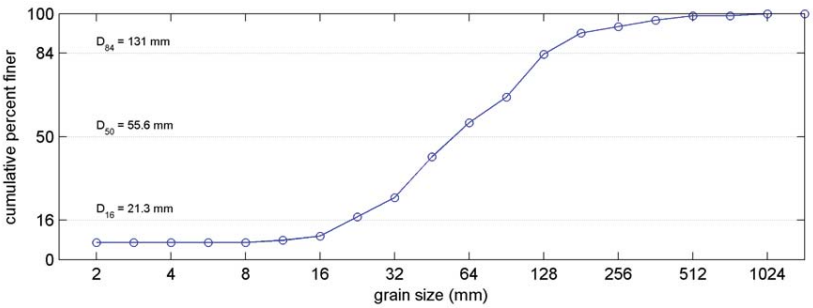
cumulative percent finer
grain size (mm)
D84 = 131 mm
D50 = 55.6 mm
D16 = 21.3 mm

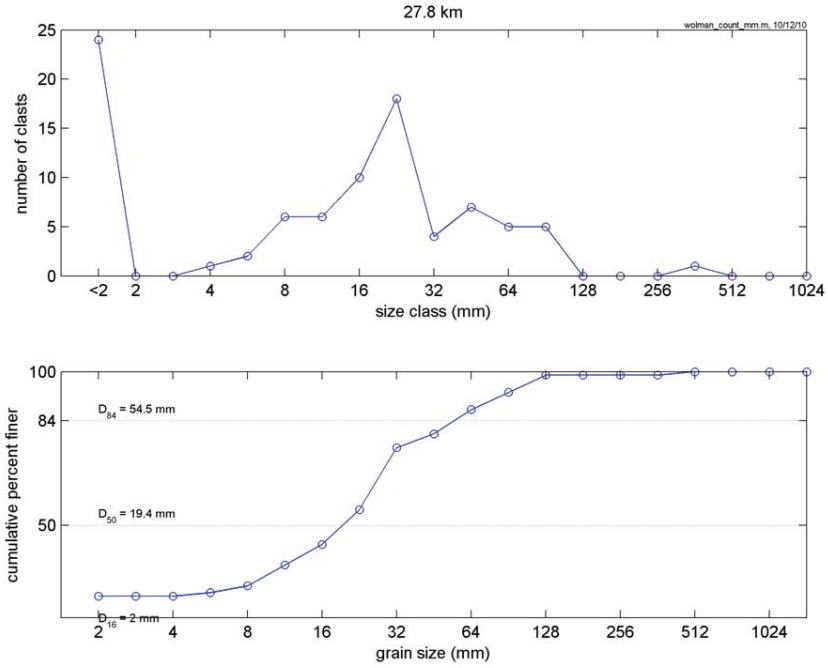
27.8 km
wolman_count_mm.m, 10/12/10
number of clasts
size class (mm)
<2
2
4
8
16
32
64
128
256
512
1024
cumulative percent finer
grain size (mm)
D84 = 54.5 mm
D50 = 19.4 mm
D16 = 2 mm

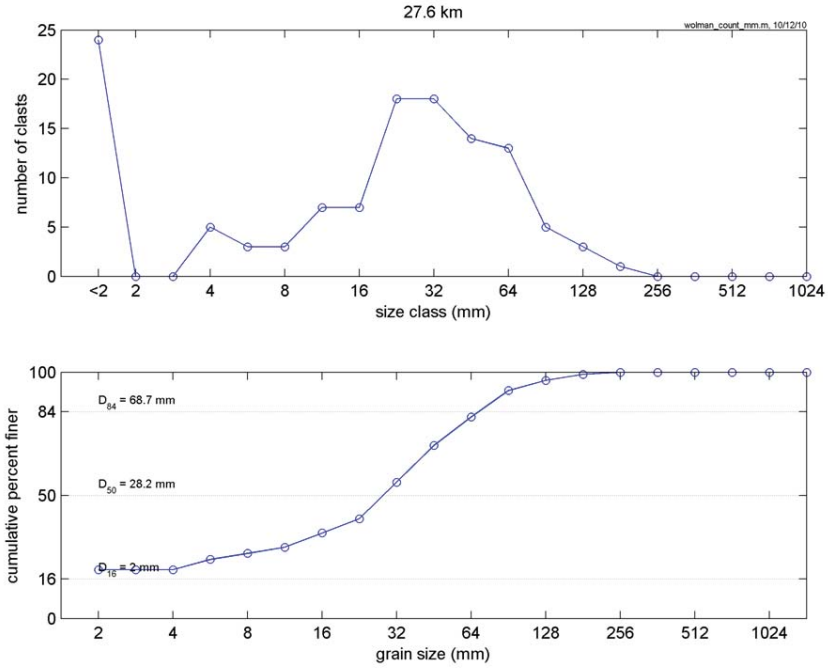
27.6 km
wolman_count_mm.m, 10/12/10
number of clasts
size class (mm)
<2
2
4
8
16
32
64
128
256
512
1024
cumulative percent finer
grain size (mm)
D84 = 68.7 mm
D50 = 28.2 mm
D16 = 2 mm

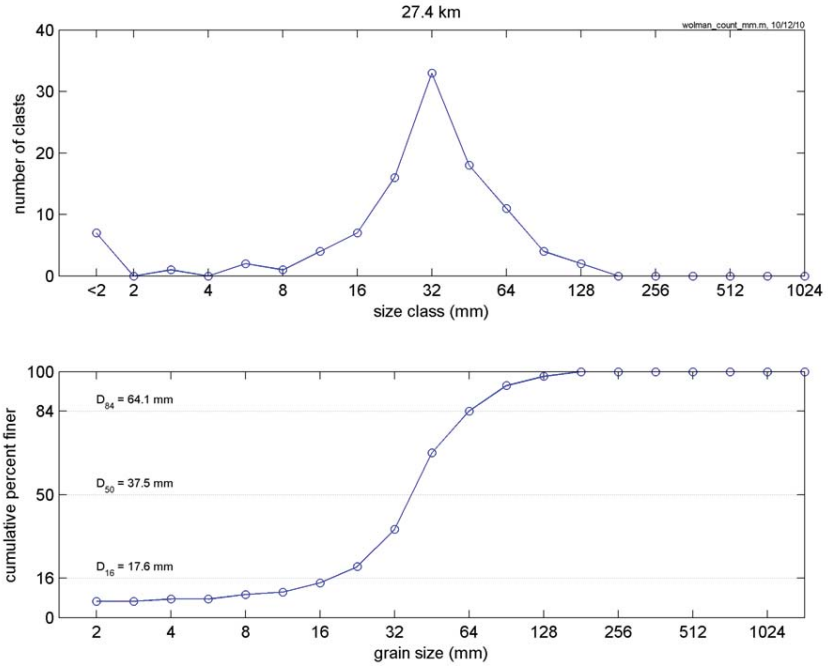
27.4 km
wolman_count_mm.m, 10/12/10
number of clasts
size class (mm)
<2
2
4
8
16
32
64
128
256
512
1024
cumulative percent finer
grain size (mm)
D84 = 64.1 mm
D50 = 37.5 mm
D16 = 17.6 mm

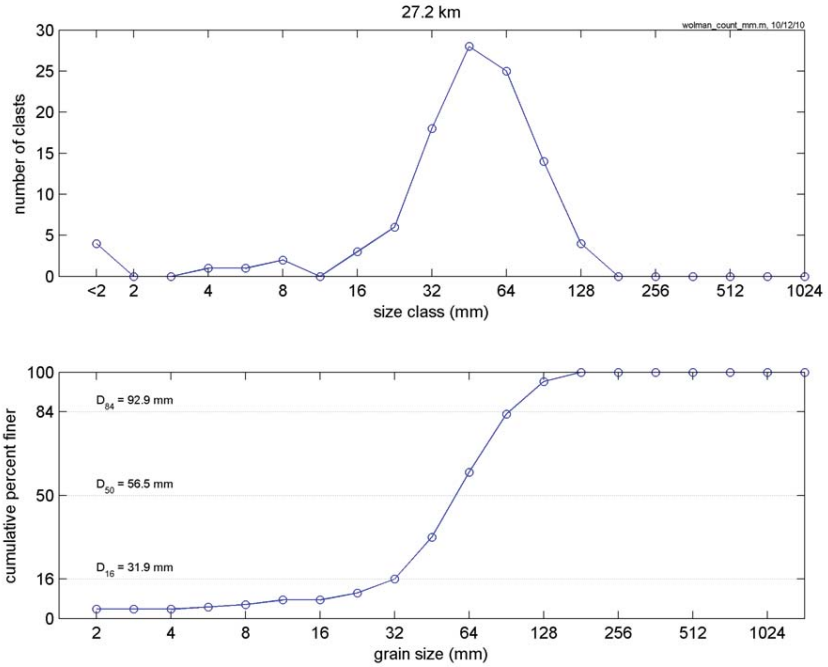
27.2 km
wolman_count_mm.m, 10/12/10
number of clasts
size class (mm)
<2
2
4
8
16
32
64
128
256
512
1024
cumulative percent finer
grain size (mm)
D84 = 92.9 mm
D50 = 56.5 mm
D16 = 31.9 mm

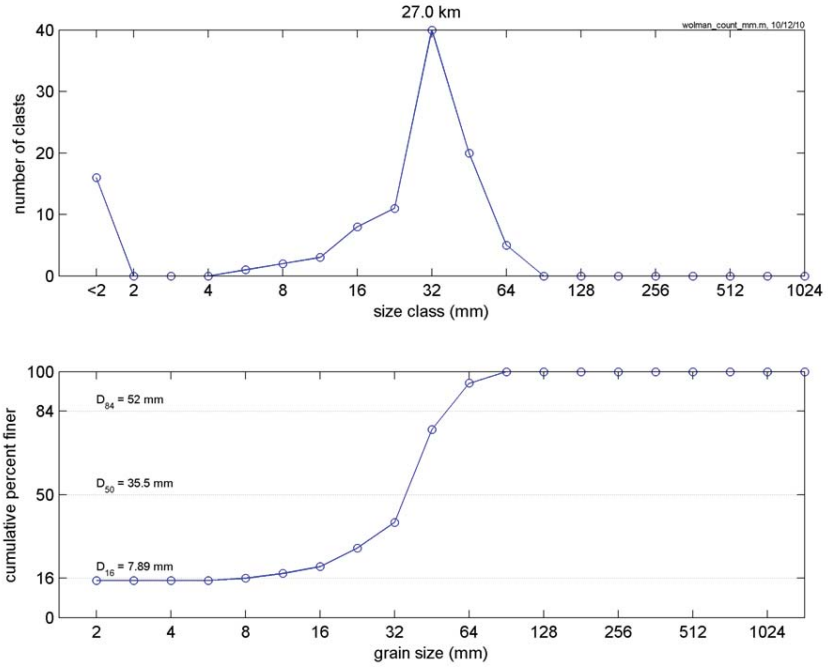
27.0 km
wolman_count_mm.m, 10/12/10
number of clasts
size class (mm)
<2
2
4
8
16
32
64
128
256
512
1024
cumulative percent finer
D84 = 52 mm
D50 = 35.5 mm
D16 = 7.89 mm
grain size (mm)

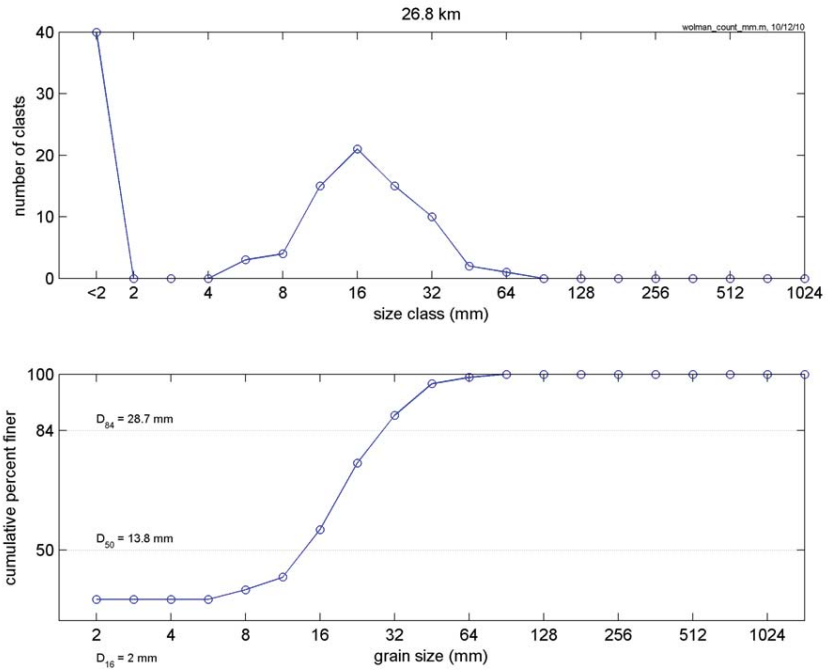
26.8 km
wolman_count_mm.m, 10/12/10
number of clasts
size class (mm)
<2
2
4
8
16
32
64
128
256
512
1024
cumulative percent finer
D84 = 28.7 mm
D50 = 13.8 mm
D16 = 2 mm
grain size (mm)

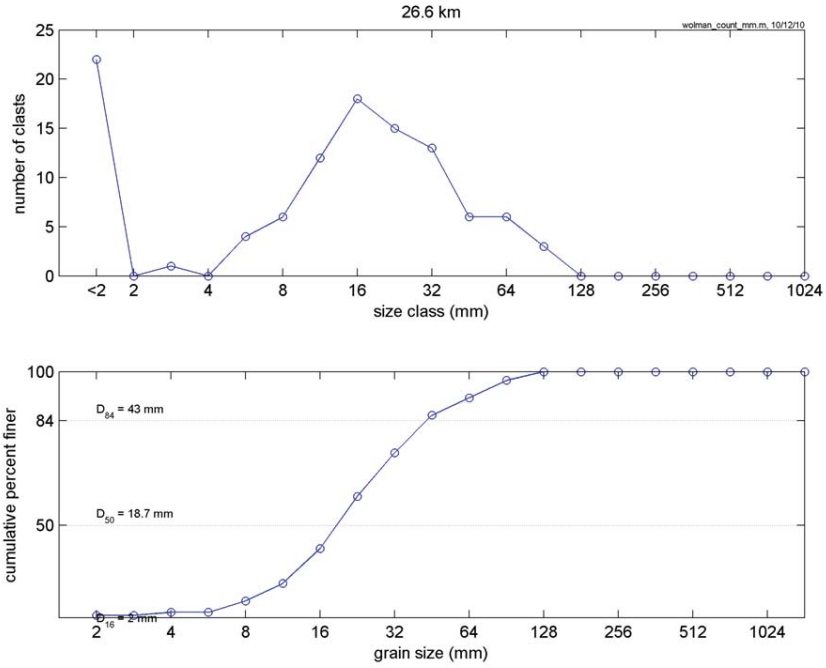
26.6 km
wolman_count_mm.m, 10/12/10
number of clasts
size class (mm)
<2
2
4
8
16
32
64
128
256
512
1024
cumulative percent finer
grain size (mm)
D84 = 43 mm
D50 = 18.7 mm
D16 = 2 mm

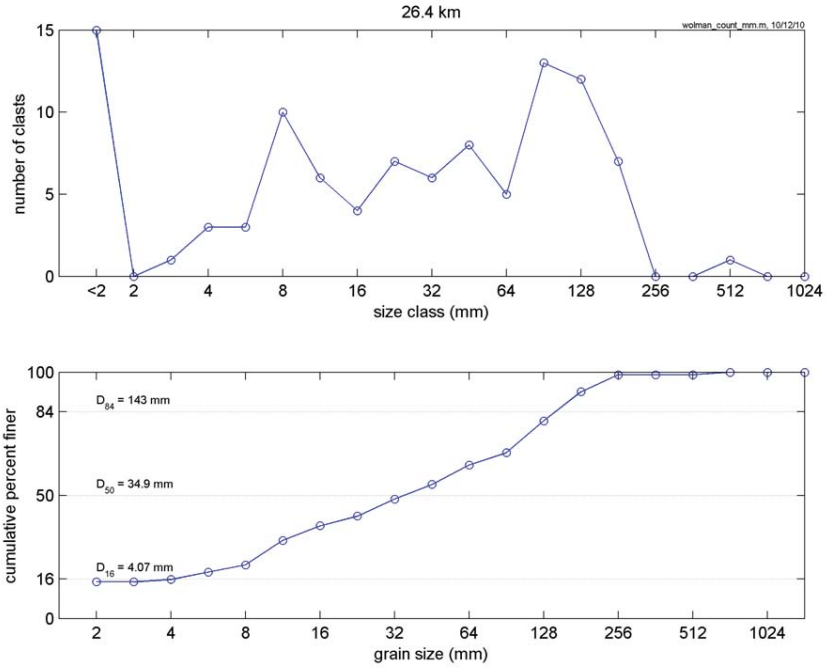
26.4 km
wolman_count_mm.m, 10/12/10
number of clasts
size class (mm)
<2
2
4
8
16
32
64
128
256
512
1024
cumulative percent finer
grain size (mm)
D84 = 143 mm
D50 = 34.9 mm
D16 = 4.07 mm

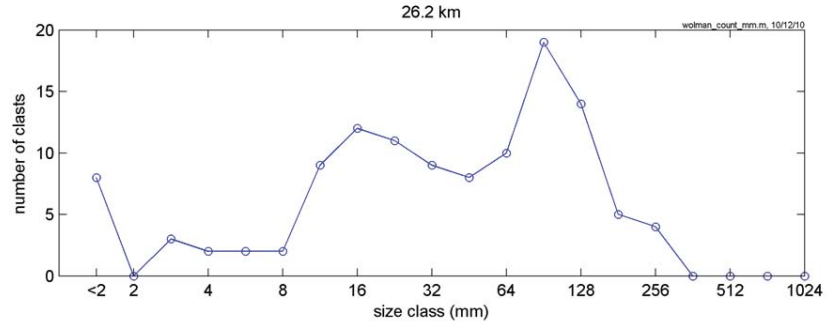
26.2 km
wolman_count_mm.m, 10/12/10
number of clasts
size class (mm)
<2
2
4
8
16
32
64
128
256
512
1024

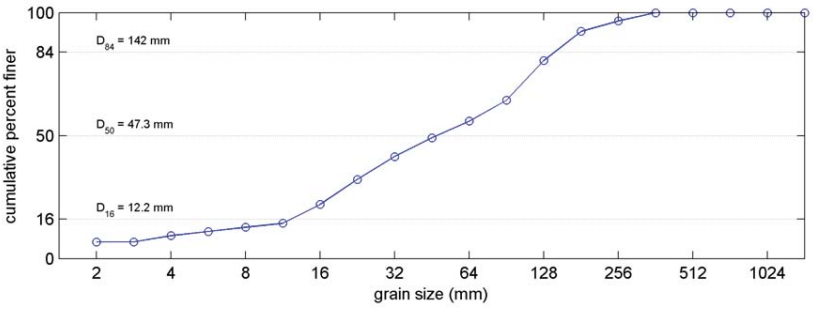
cumulative percent finer
grain size (mm)
D84 = 142 mm
D50 = 47.3 mm
D16 = 12.2 mm

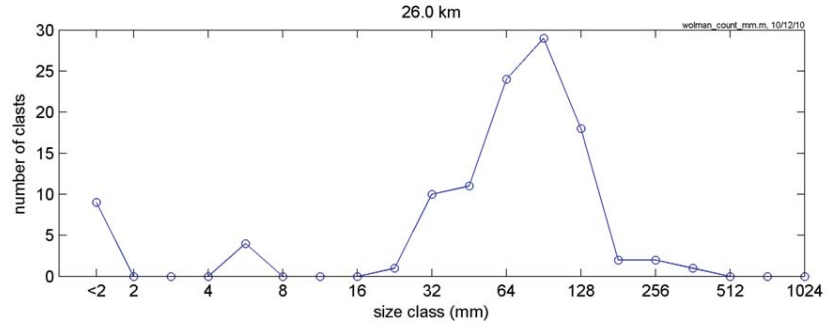
26.0 km
wolman_count_mm.m, 10/12/10
number of clasts
size class (mm)
<2
2
4
8
16
32
64
128
256
512
1024

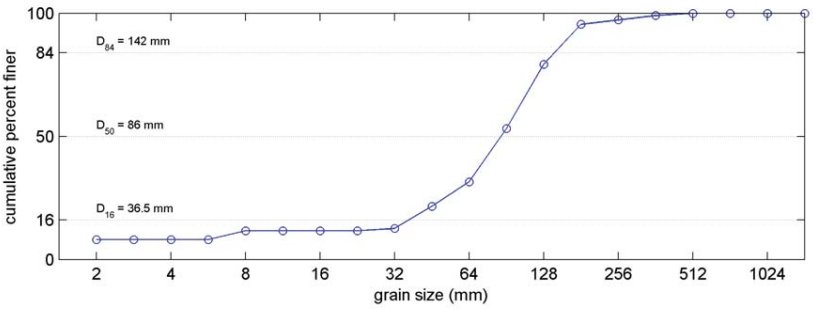
cumulative percent finer
grain size (mm)
D84 = 142 mm
D50 = 86 mm
D16 = 36.5 mm

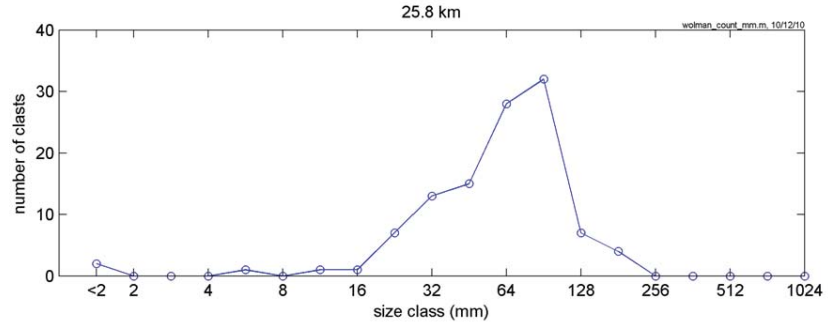
25.8 km
wolman_count_mm.m, 10/12/10
number of clasts
size class (mm)
<2
2
4
8
16
32
64
128
256
512
1024

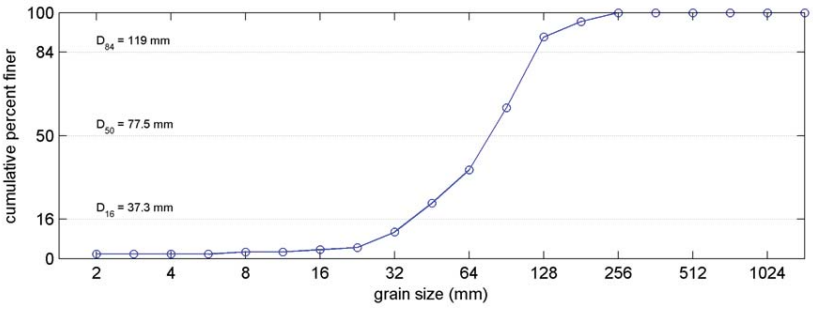
cumulative percent finer
grain size (mm)
D84 = 119 mm
D50 = 77.5 mm
D16 = 37.3 mm

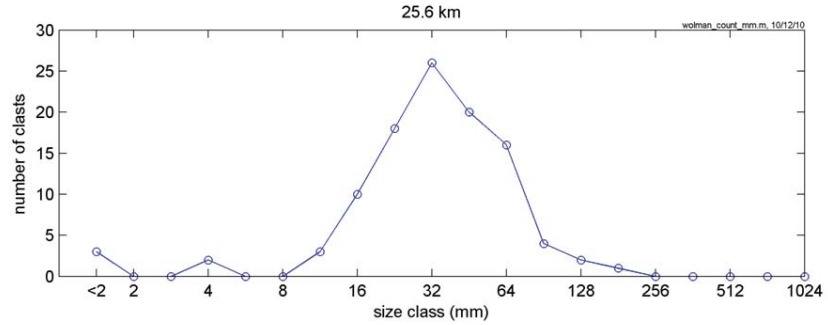
25.6 km
wolman_count_mm.m, 10/12/10
number of clasts
size class (mm)
<2
2
4
8
16
32
64
128
256
512
1024

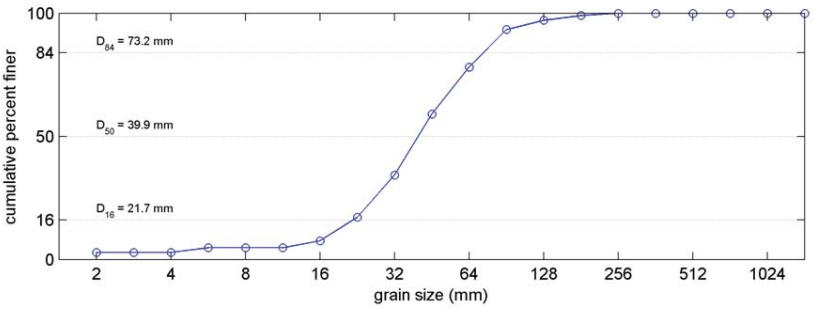
cumulative percent finer
grain size (mm)
D84 = 73.2 mm
D50 = 39.9 mm
D16 = 21.7 mm

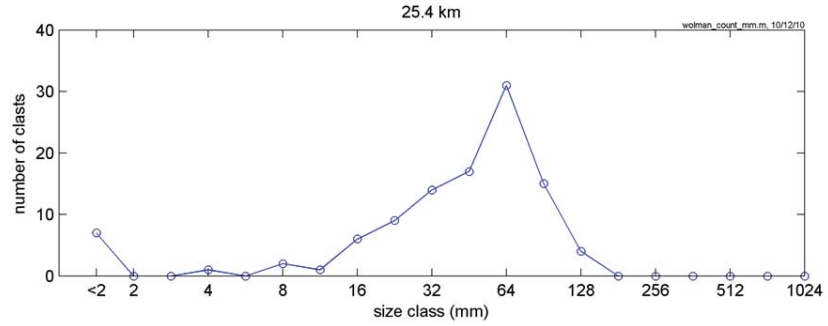
25.4 km
wolman_count_mm.m, 10/12/10
number of clasts
size class (mm)
<2
2
4
8
16
32
64
128
256
512
1024

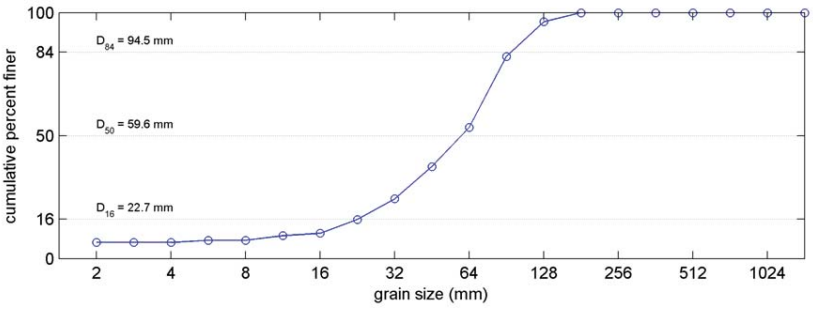
cumulative percent finer
grain size (mm)
D84 = 94.5 mm
D50 = 59.6 mm
D16 = 22.7 mm

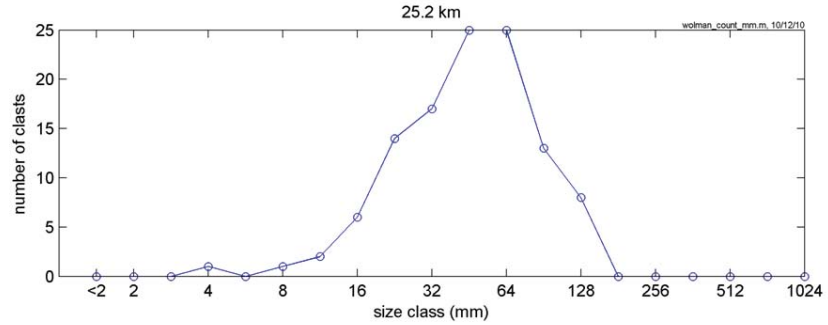
25.2 km
wolman_count_mm.m, 10/12/10
number of clasts
size class (mm)
<2
2
4
8
16
32
64
128
256
512
1024

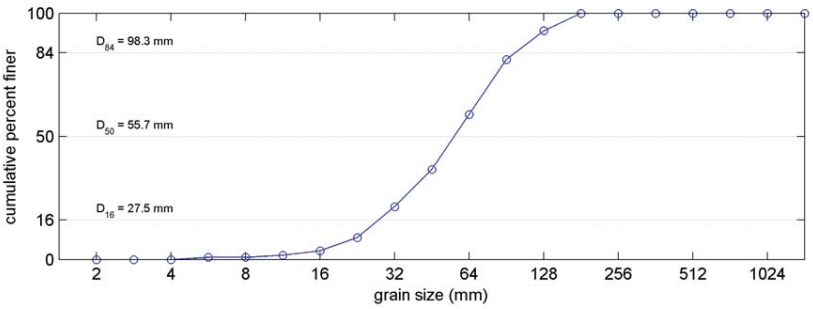
cumulative percent finer
grain size (mm)
D84 = 98.3 mm
D50 = 55.7 mm
D16 = 27.5 mm

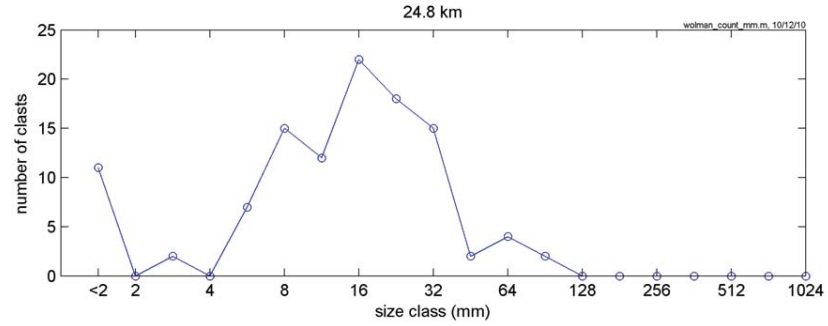
24.8 km
wolman_count_mm.m, 10/12/10
number of clasts
size class (mm)
<2
2
4
8
16
32
64
128
256
512
1024

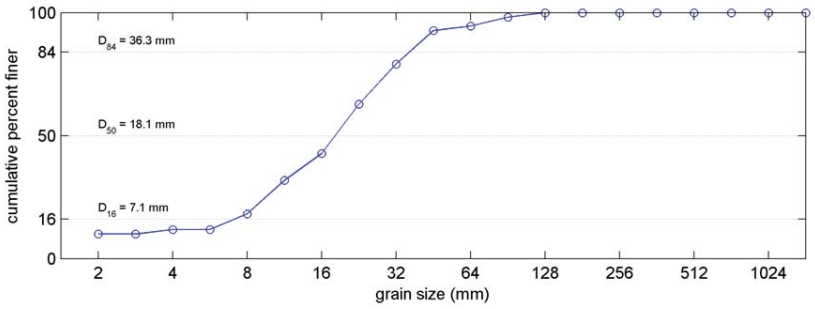
cumulative percent finer
grain size (mm)
D84 = 36.3 mm
D50 = 18.1 mm
D16 = 7.1 mm

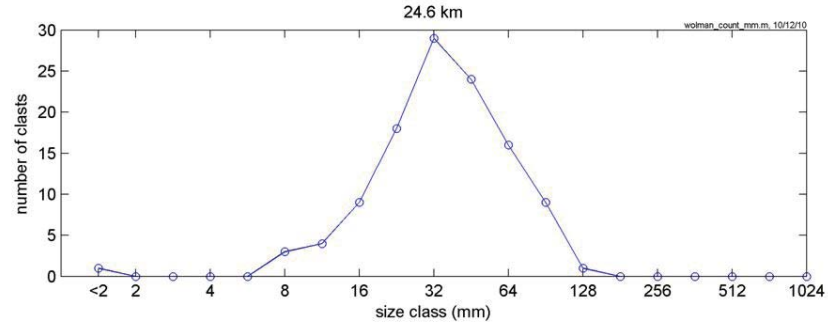
24.6 km
wolman_count_mm.m, 10/12/10
number of clasts
size class (mm)
<2
2
4
8
16
32
64
128
256
512
1024

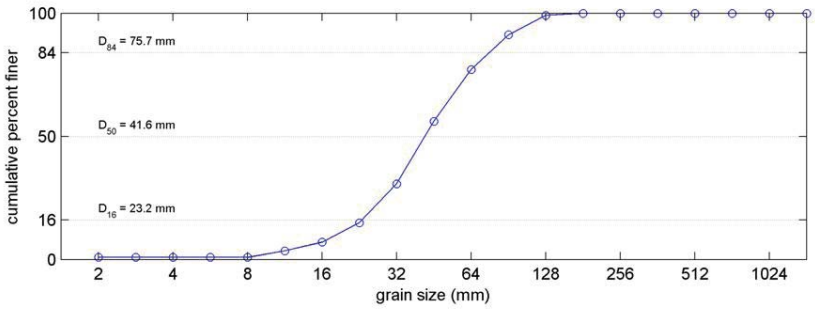
cumulative percent finer
grain size (mm)
D84 = 75.7 mm
D50 = 41.6 mm
D16 = 23.2 mm

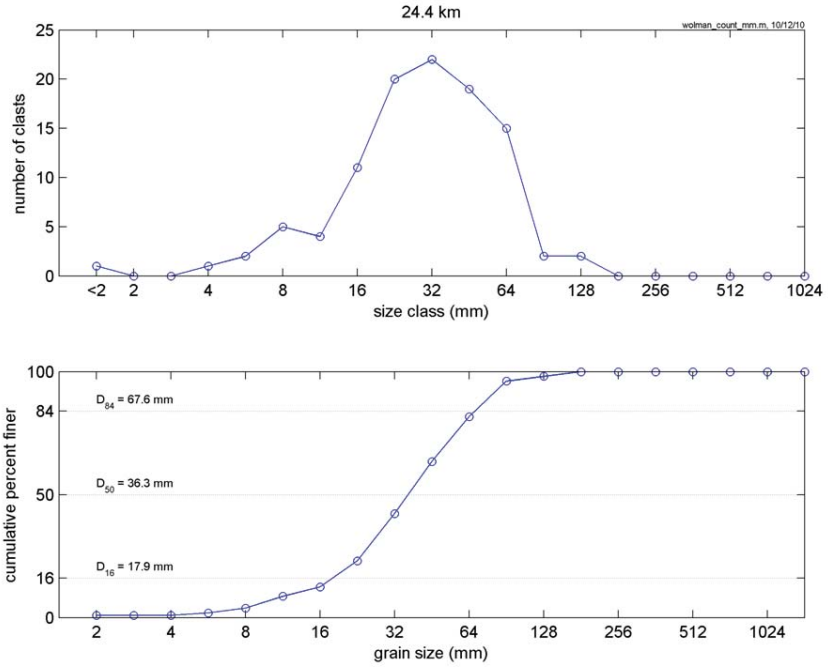
24.4 km
wolman_count_mm.m, 10/12/10
number of clasts
size class (mm)
<2
2
4
8
16
32
64
128
256
512
1024
cumulative percent finer
grain size (mm)
D84 = 67.6 mm
D50 = 36.3 mm
D16 = 17.9 mm

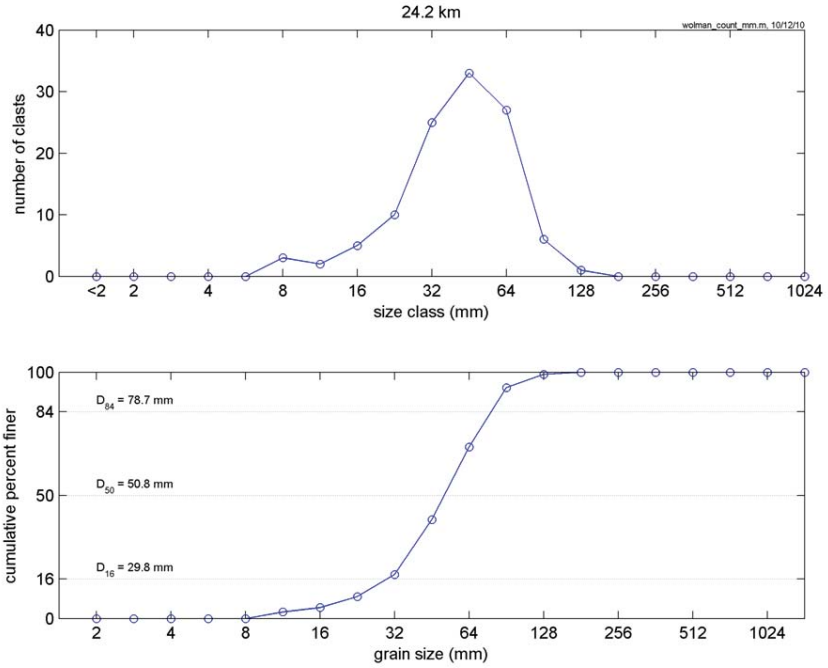
24.2 km
wolman_count_mm.m, 10/12/10
number of clasts
size class (mm)
<2
2
4
8
16
32
64
128
256
512
1024
cumulative percent finer
grain size (mm)
D84 = 78.7 mm
D50 = 50.8 mm
D16 = 29.8 mm

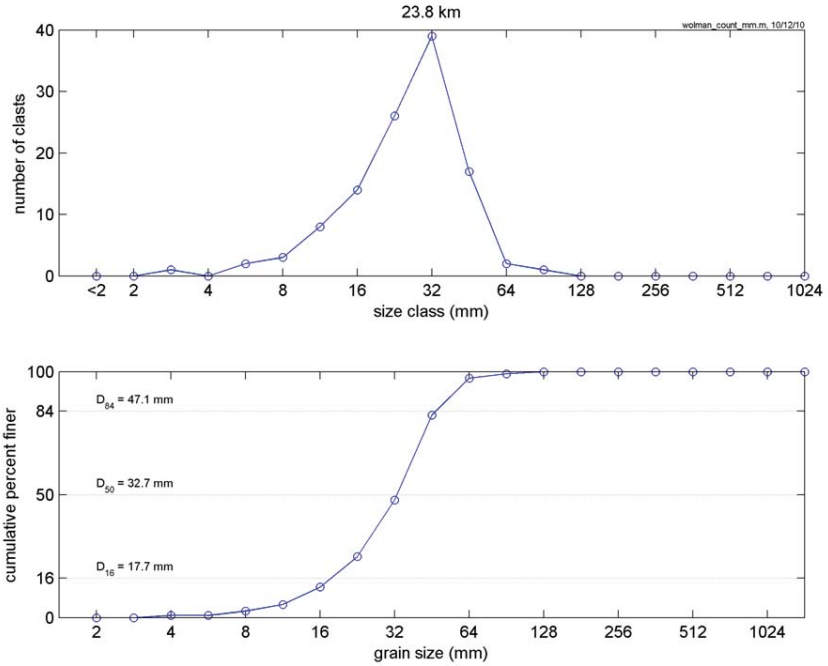
23.8 km
wolman_count_mm.m, 10/12/10
number of clasts
size class (mm)
<2
2
4
8
16
32
64
128
256
512
1024
cumulative percent finer
grain size (mm)
D84 = 47.1 mm
D50 = 32.7 mm
D16 = 17.7 mm

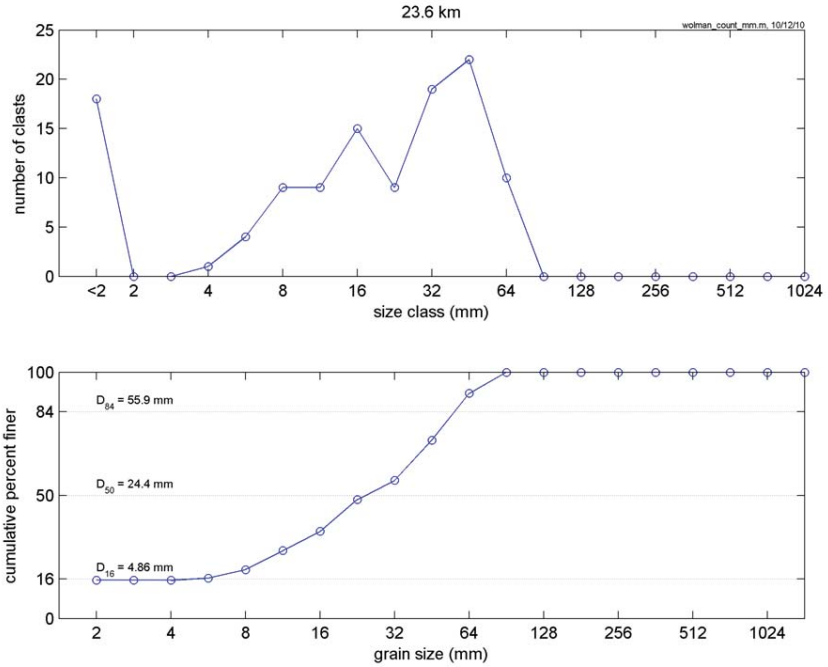
23.6 km
wolman_count_mm.m, 10/12/10
number of clasts
size class (mm)
<2
2
4
8
16
32
64
128
256
512
1024
cumulative percent finer
grain size (mm)
D84 = 55.9 mm
D50 = 24.4 mm
D16 = 4.86 mm

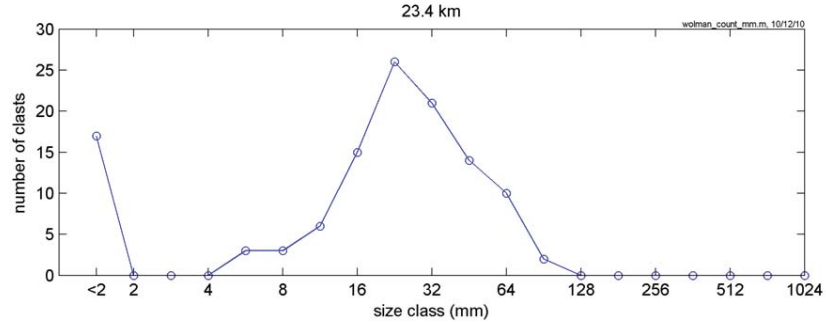
23.4 km
wolman_count_mm.m, 10/12/10
number of clasts
size class (mm)
<2
2
4
8
16
32
64
128
256
512
1024

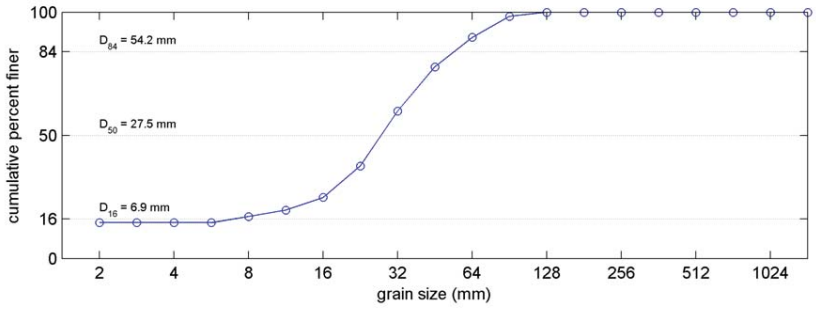
cumulative percent finer
grain size (mm)
D84 = 54.2 mm
D50 = 27.5 mm
D16 = 6.9 mm

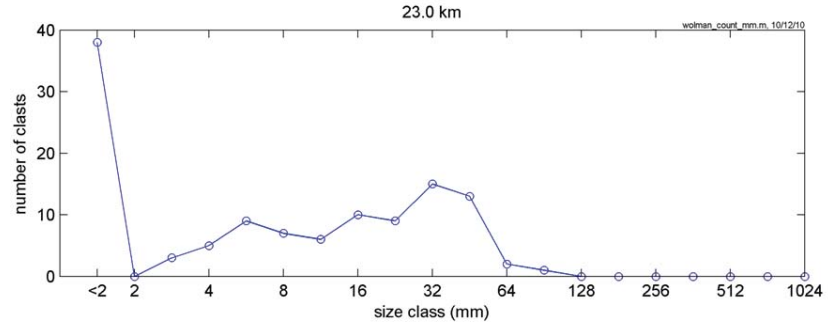
23.0 km
wolman_count_mm.m, 10/12/10
number of clasts
size class (mm)

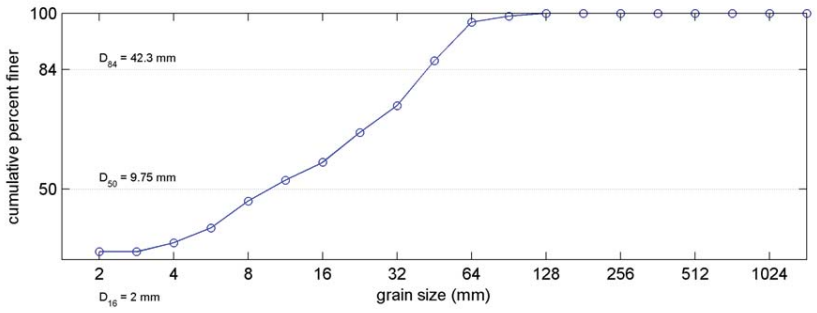
cumulative percent finer
grain size (mm)
D84 = 42.3 mm
D50 = 9.75 mm
D16 = 2 mm

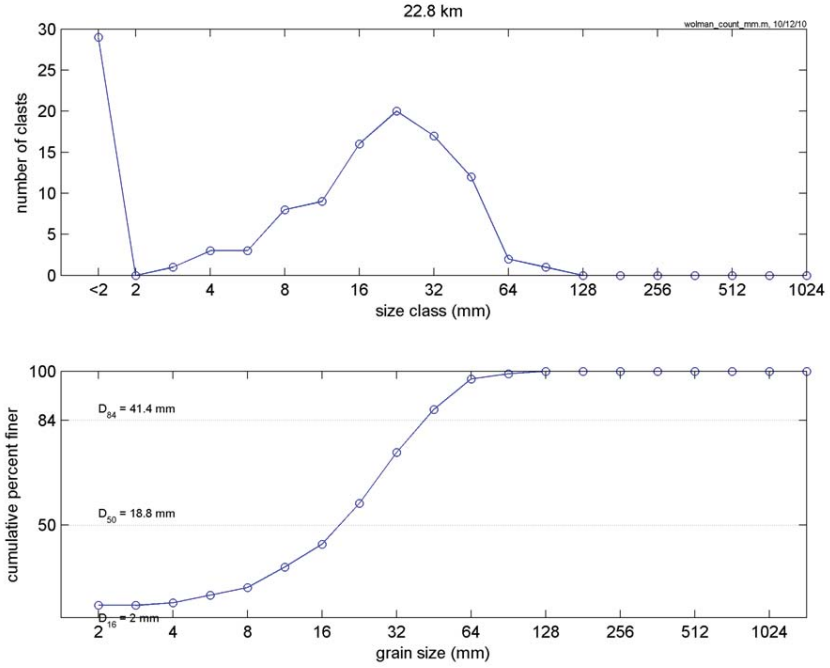
22.8 km
wolman_count_mm.m, 10/12/10
number of clasts
size class (mm)
cumulative percent finer
D84 = 41.4 mm
D50 = 18.8 mm
D16 = 2 mm
grain size (mm)

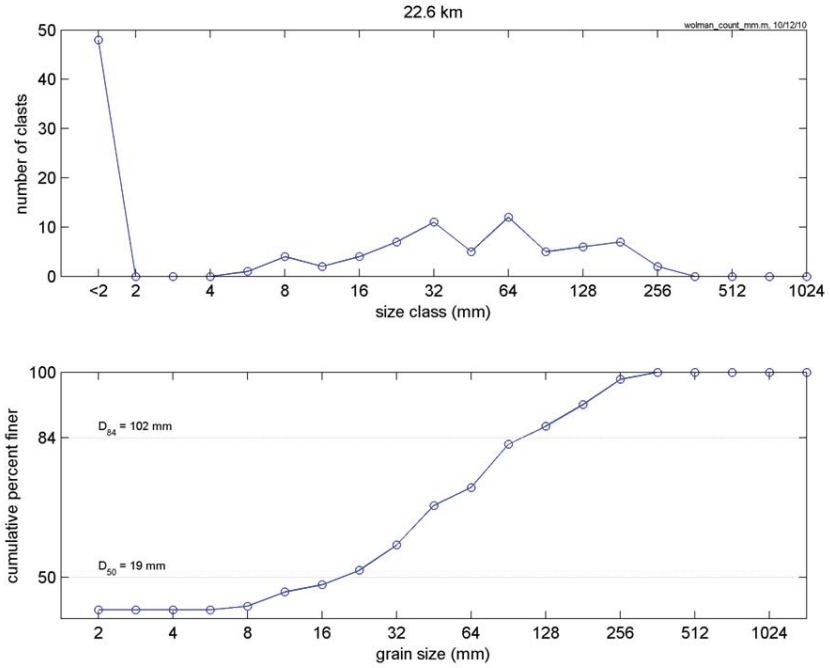
22.6 km
wolman_count_mm.m, 10/12/10
number of clasts
size class (mm)
cumulative percent finer
D84 = 102 mm
D50 = 19 mm
grain size (mm)

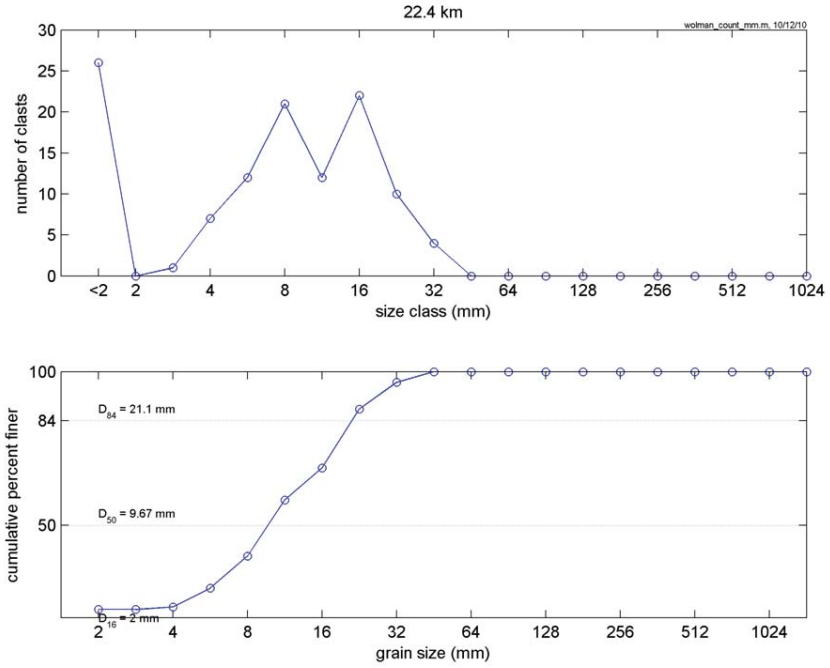
22.4 km
wolman_count_mm.m, 10/12/10
number of clasts
size class (mm)
<2
2
4
8
16
32
64
128
256
512
1024
cumulative percent finer
grain size (mm)
D84 = 21.1 mm
D50 = 9.67 mm
D16 = 2 mm

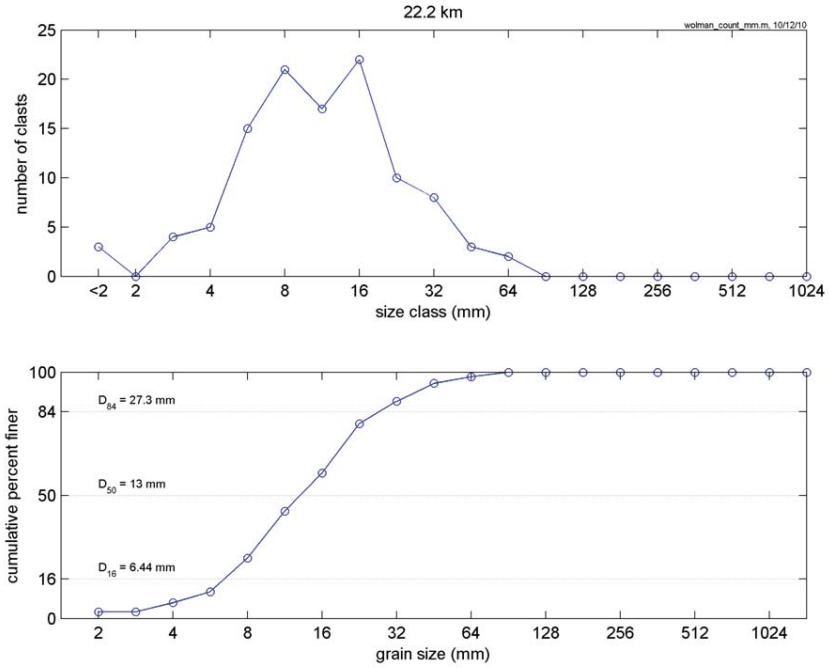
22.2 km
wolman_count_mm.m, 10/12/10
number of clasts
size class (mm)
<2
2
4
8
16
32
64
128
256
512
1024
cumulative percent finer
grain size (mm)
D84 = 27.3 mm
D50 = 13 mm
D16 = 6.44 mm

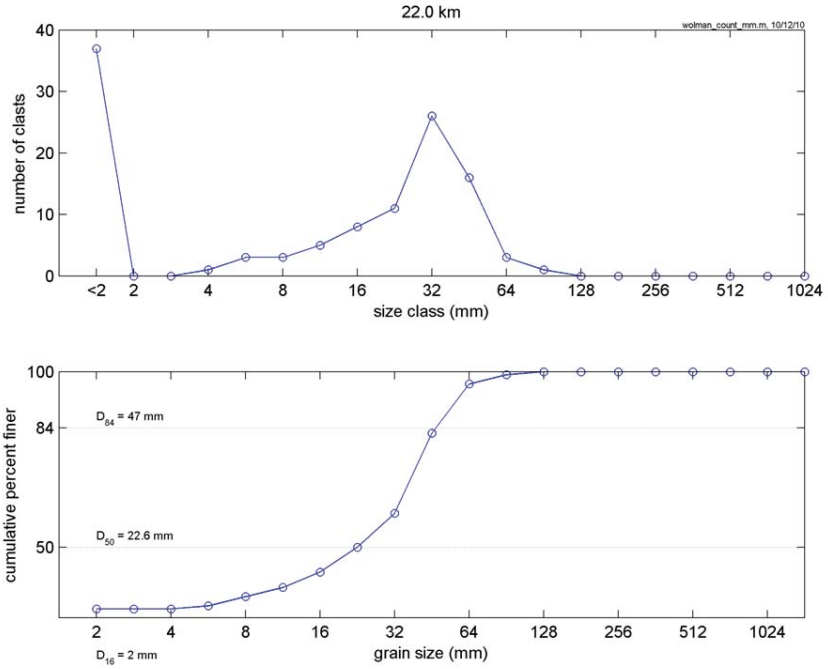
22.0 km
wolman_count_mm.m, 10/12/10
number of clasts
size class (mm)
<2
2
4
8
16
32
64
128
256
512
1024
cumulative percent finer
grain size (mm)
D84 = 47 mm
D50 = 22.6 mm
D16 = 2 mm

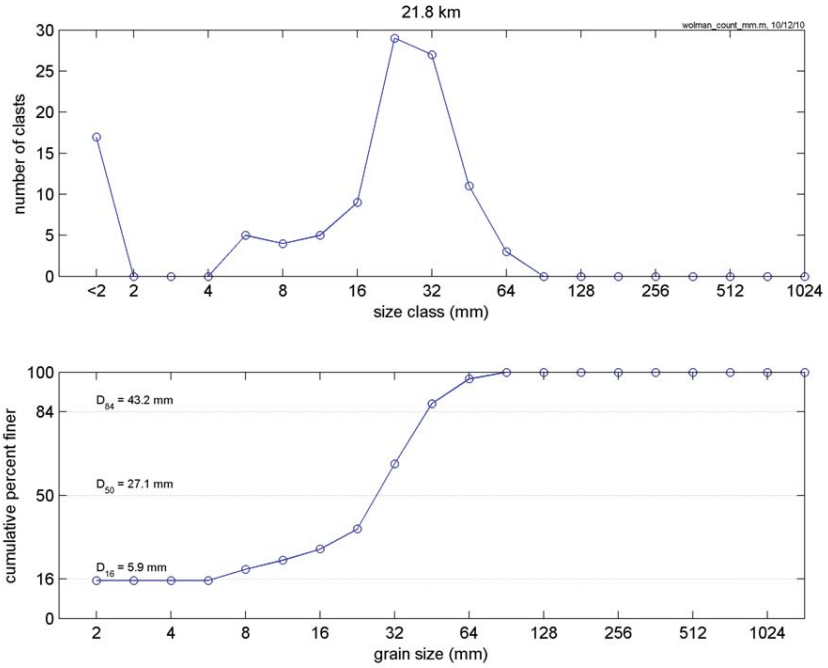
21.8 km
wolman_count_mm.m, 10/12/10
number of clasts
size class (mm)
<2
2
4
8
16
32
64
128
256
512
1024
cumulative percent finer
grain size (mm)
D84 = 43.2 mm
D50 = 27.1 mm
D16 = 5.9 mm

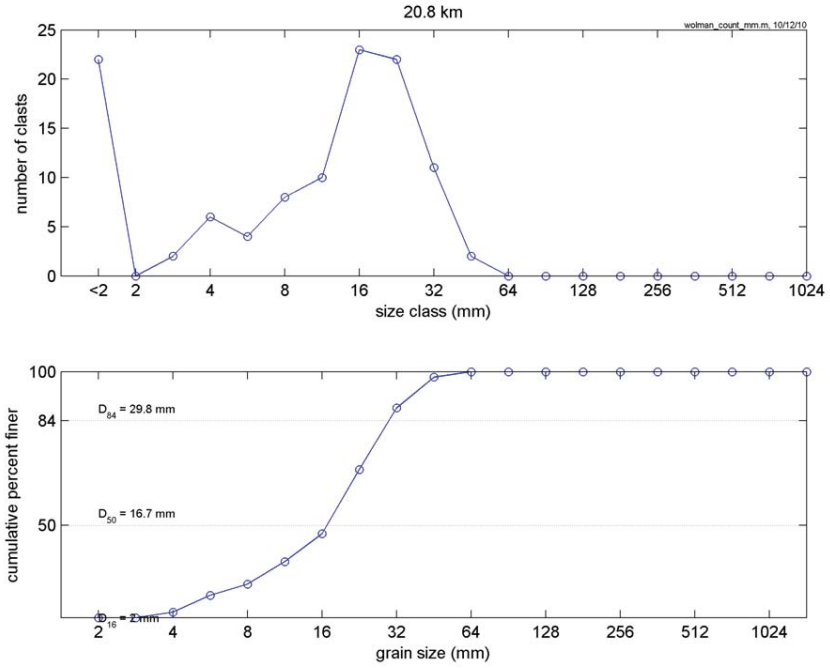
20.8 km
wolman_count_mm.m, 10/12/10
number of clasts
size class (mm)
<2
2
4
8
16
32
64
128
256
512
1024
cumulative percent finer
grain size (mm)
D84 = 29.8 mm
D50 = 16.7 mm
D16 = 2 mm

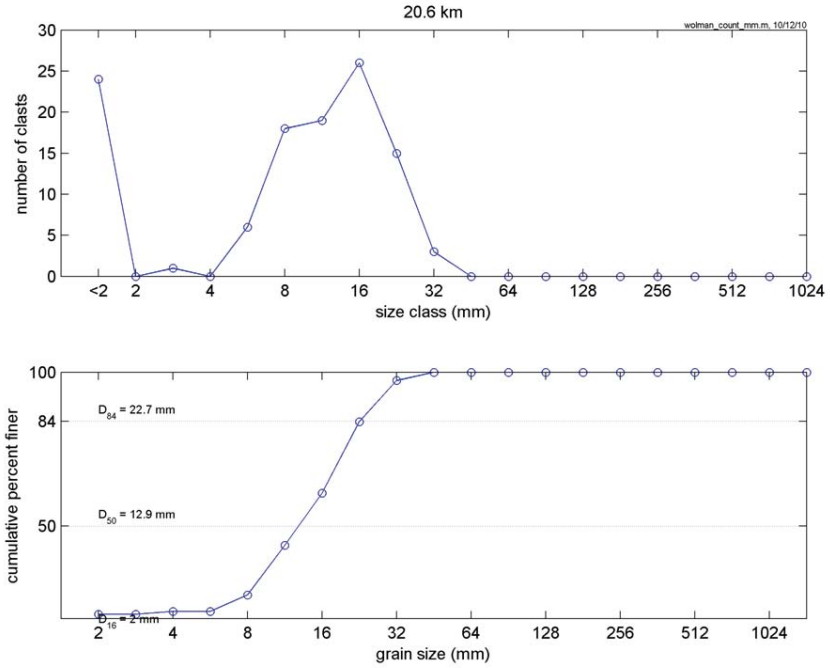
20.6 km
wolman_count_mm.m, 10/12/10
number of clasts
size class (mm)
<2
2
4
8
16
32
64
128
256
512
1024
cumulative percent finer
grain size (mm)
D84 = 22.7 mm
D50 = 12.9 mm
D16 = 2 mm

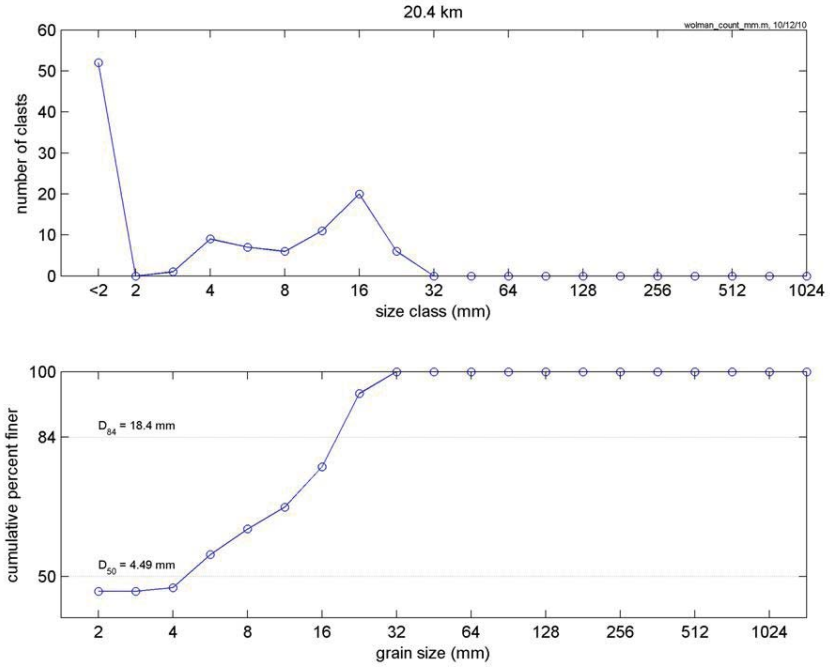
20.4 km
wolman_count_mm.m, 10/12/10
number of clasts
size class (mm)
cumulative percent finer
grain size (mm)
D84 = 18.4 mm
D50 = 4.49 mm

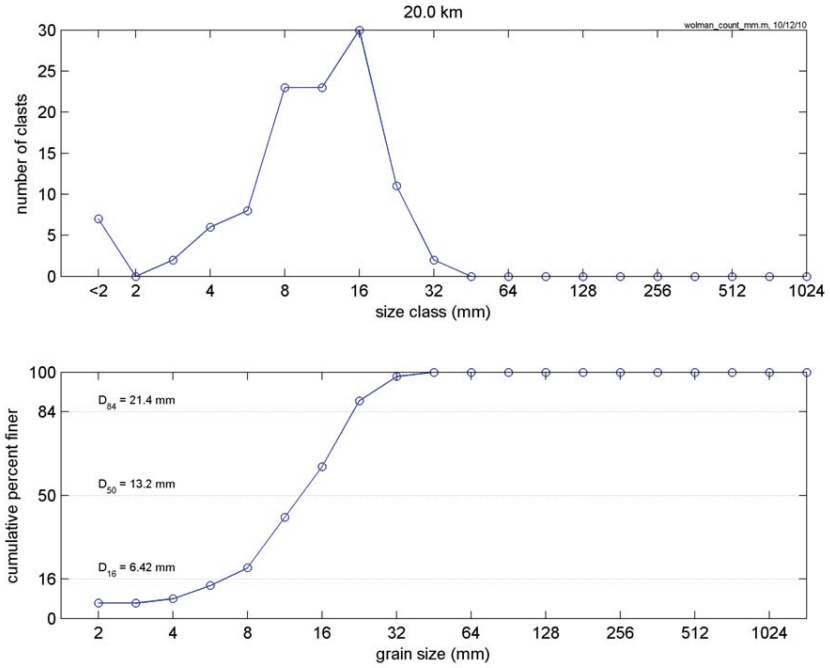
20.0 km
wolman_count_mm.m, 10/12/10
number of clasts
size class (mm)
cumulative percent finer
grain size (mm)
D84 = 21.4 mm
D50 = 13.2 mm
D16 = 6.42 mm

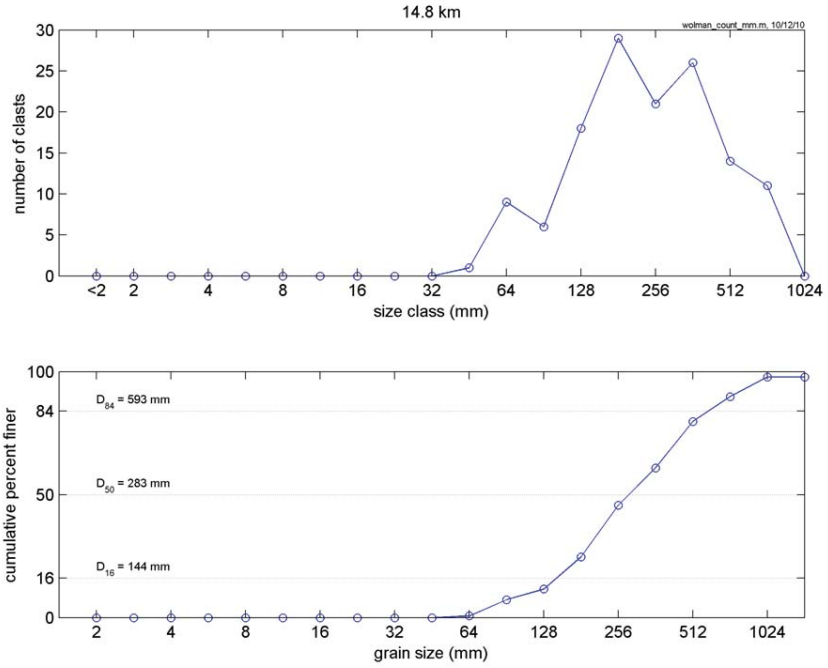
14.8 km
wolman_count_mm.m, 10/12/10
number of clasts
size class (mm)
<2
2
4
8
16
32
64
128
256
512
1024
cumulative percent finer
grain size (mm)
D84 = 593 mm
D50 = 283 mm
D16 = 144 mm

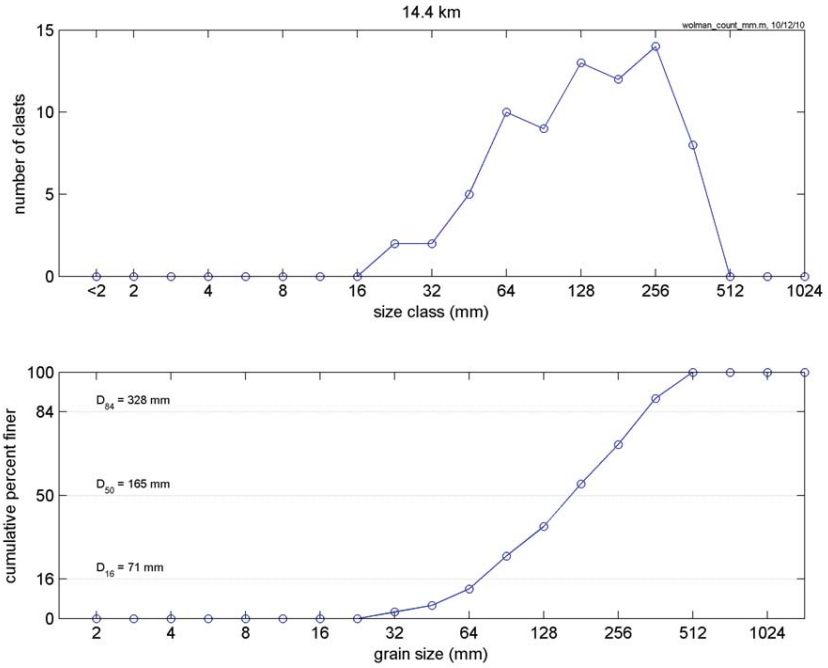
14.4 km
wolman_count_mm.m, 10/12/10
number of clasts
size class (mm)
<2
2
4
8
16
32
64
128
256
512
1024
cumulative percent finer
grain size (mm)
D84 = 328 mm
D50 = 165 mm
D16 = 71 mm

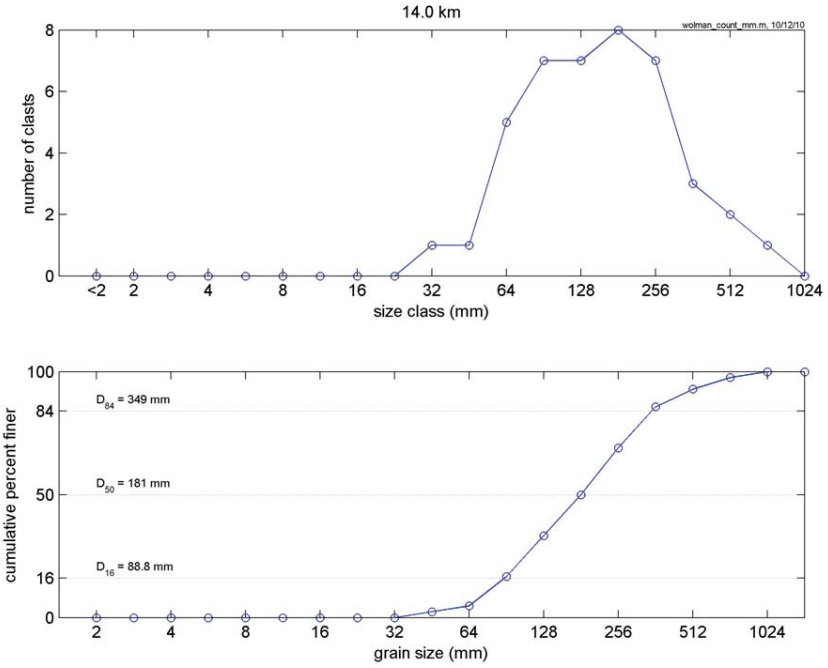
14.0 km
wolman_count_mm.m, 10/12/10
number of clasts
size class (mm)
<2
2
4
8
16
32
64
128
256
512
1024
cumulative percent finer
grain size (mm)
D84 = 349 mm
D50 = 181 mm
D16 = 88.8 mm

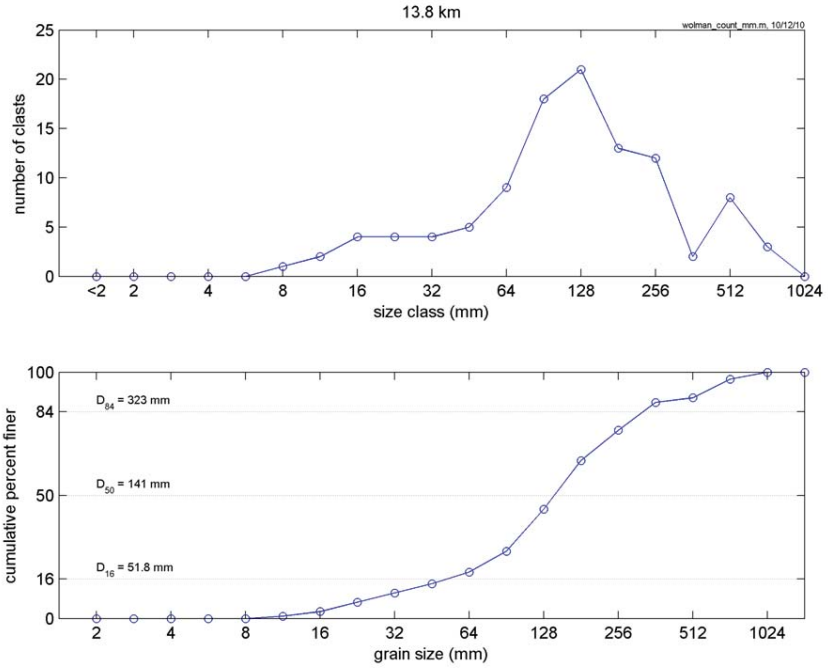
13.8 km
wolman_count_mm.m, 10/12/10
number of clasts
size class (mm)
<2
2
4
8
16
32
64
128
256
512
1024
cumulative percent finer
grain size (mm)
D84 = 323 mm
D50 = 141 mm
D16 = 51.8 mm

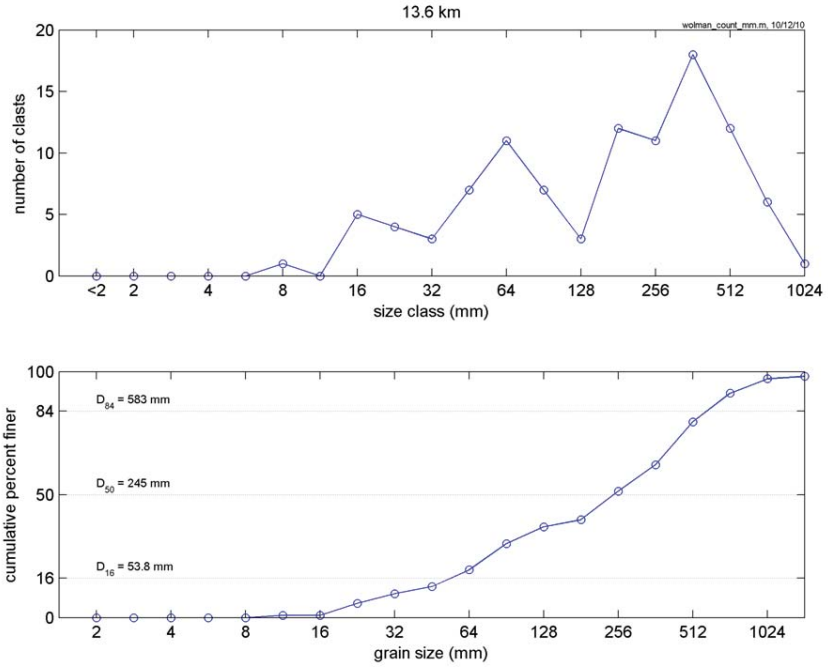
13.6 km
wolman_count_mm.m, 10/12/10
number of clasts
size class (mm)
<2
2
4
8
16
32
64
128
256
512
1024
cumulative percent finer
grain size (mm)
D84 = 583 mm
D50 = 245 mm
D16 = 53.8 mm

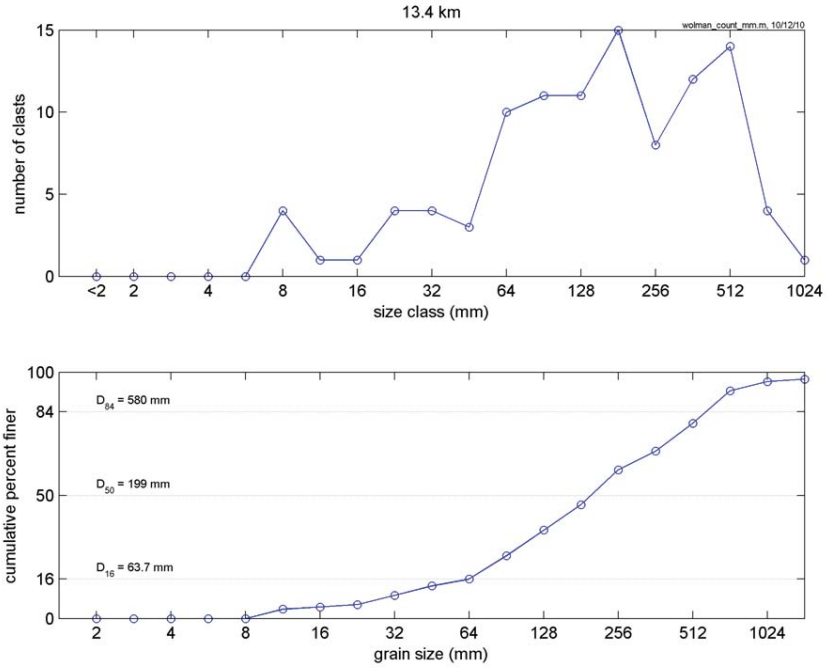
13.4 km
wolman_count_mm.m, 10/12/10
number of clasts
size class (mm)
<2
2
4
8
16
32
64
128
256
512
1024
cumulative percent finer
grain size (mm)
D84 = 580 mm
D50 = 199 mm
D16 = 63.7 mm

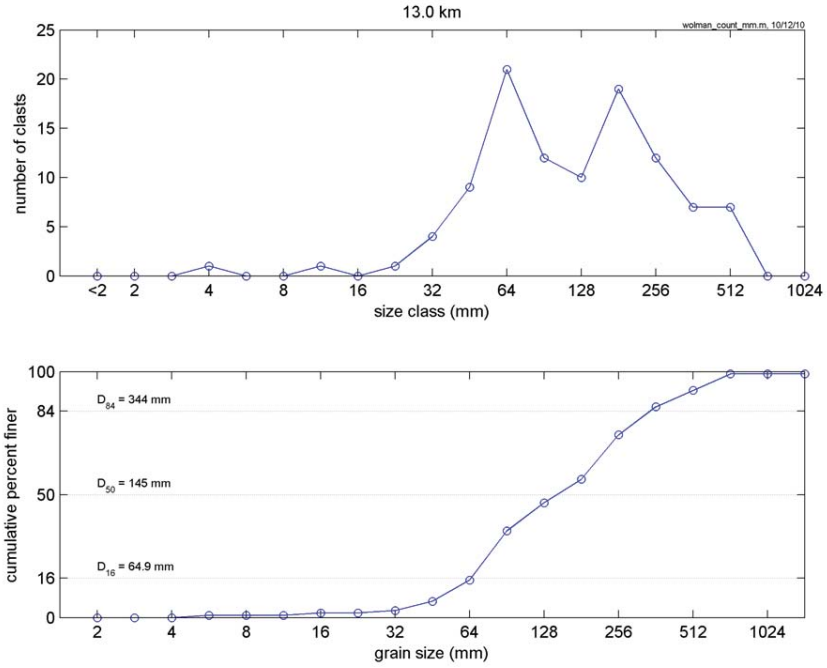
13.0 km
wolman_count_mm.m, 10/12/10
number of clasts
size class (mm)
<2
2
4
8
16
32
64
128
256
512
1024
cumulative percent finer
grain size (mm)
D84 = 344 mm
D50 = 145 mm
D16 = 64.9 mm

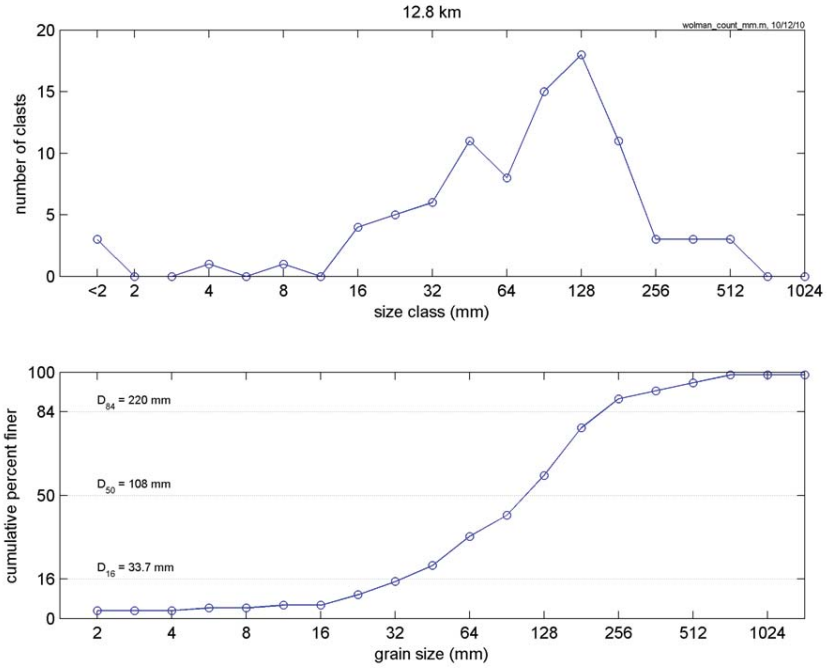
12.8 km
wolman_count_mm.m, 10/12/10
number of clasts
size class (mm)
<2
2
4
8
16
32
64
128
256
512
1024
cumulative percent finer
grain size (mm)
D84 = 220 mm
D50 = 108 mm
D16 = 33.7 mm

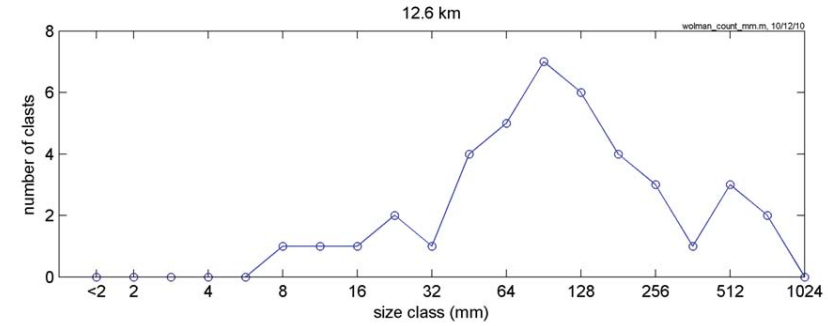
12.6 km
wolman_count_mm.m, 10/12/10
number of clasts
size class (mm)
<2
2
4
8
16
32
64
128
256
512
1024

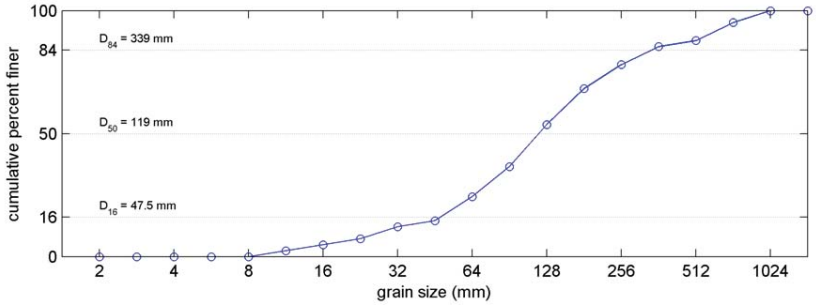
cumulative percent finer
grain size (mm)
D84 = 339 mm
D50 = 119 mm
D16 = 47.5 mm

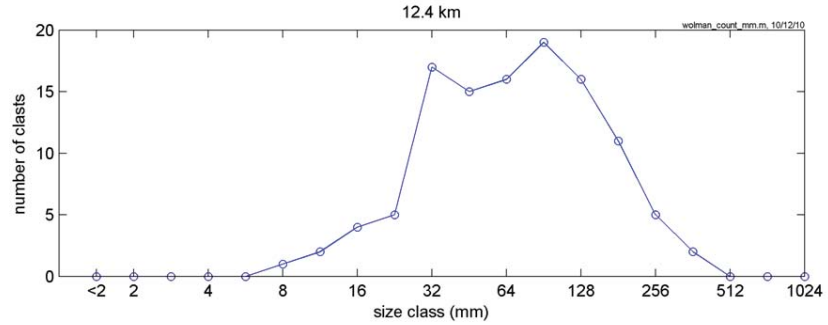
12.4 km
wolman_count_mm.m, 10/12/10
number of clasts
size class (mm)
<2
2
4
8
16
32
64
128
256
512
1024

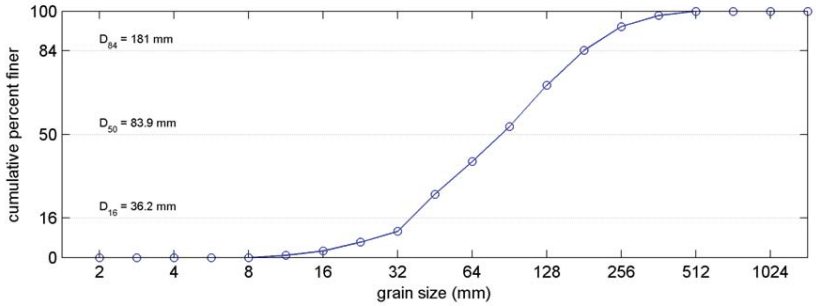
cumulative percent finer
grain size (mm)
D84 = 181 mm
D50 = 83.9 mm
D16 = 36.2 mm

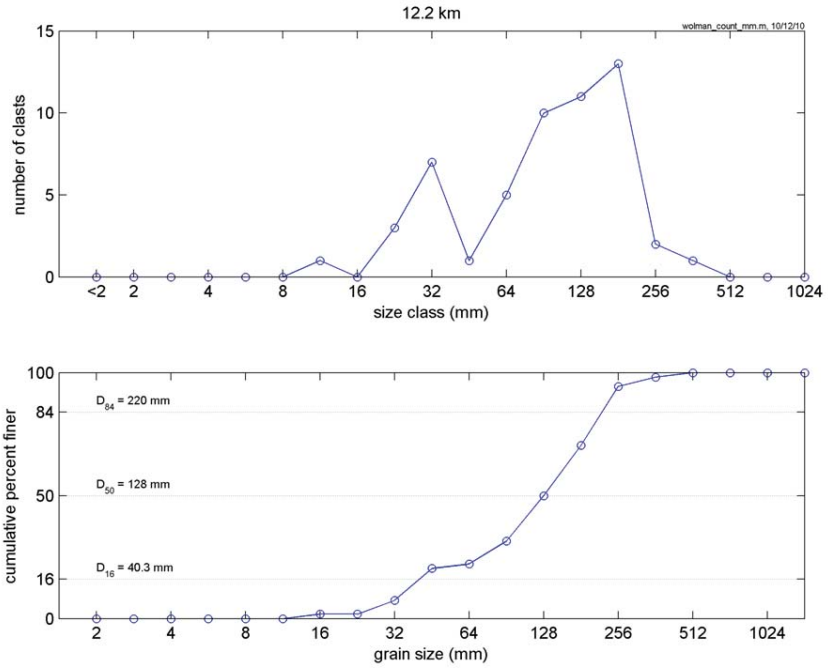
12.2 km
wolman_count_mm.m, 10/12/10
number of clasts
size class (mm)
cumulative percent finer
grain size (mm)
D84 = 220 mm
D50 = 128 mm
D16 = 40.3 mm

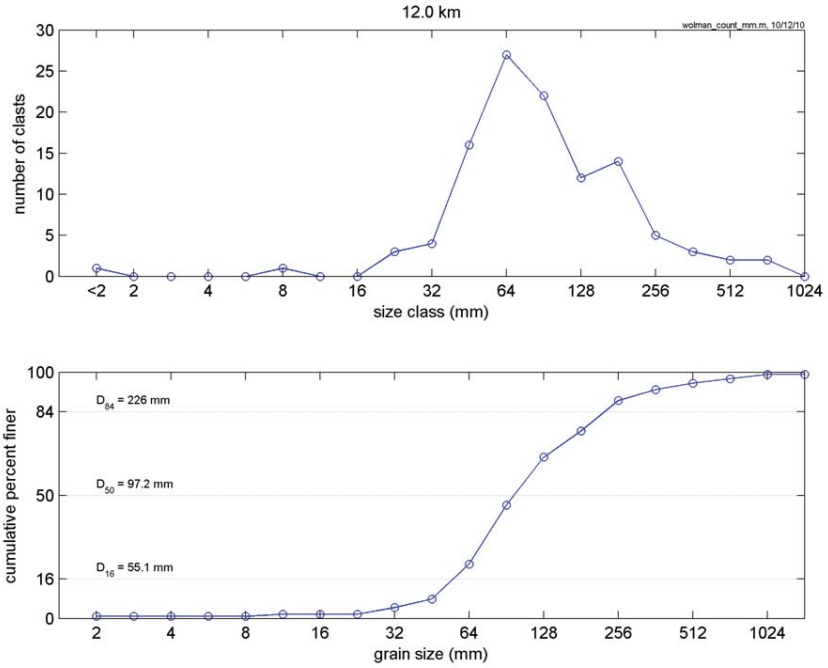
12.0 km
wolman_count_mm.m, 10/12/10
number of clasts
size class (mm)
cumulative percent finer
grain size (mm)
D84 = 226 mm
D50 = 97.2 mm
D16 = 55.1 mm

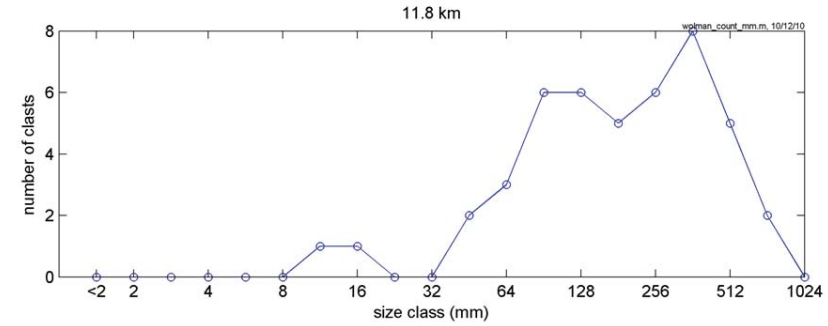
11.8 km
wolman_count_mm.m, 10/12/10
number of clasts
size class (mm)
<2
2
4
8
16
32
64
128
256
512
1024

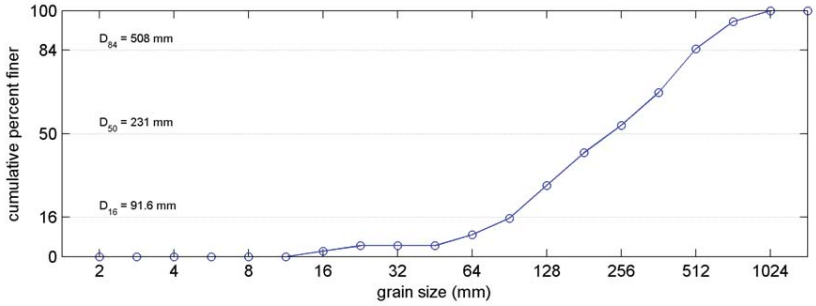
cumulative percent finer
grain size (mm)
D84 = 508 mm
D50 = 231 mm
D16 = 91.6 mm

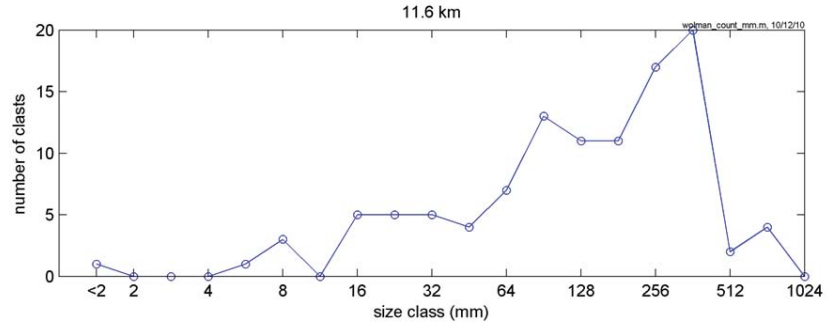
11.6 km
wolman_count_mm.m, 10/12/10
number of clasts
size class (mm)
<2
2
4
8
16
32
64
128
256
512
1024

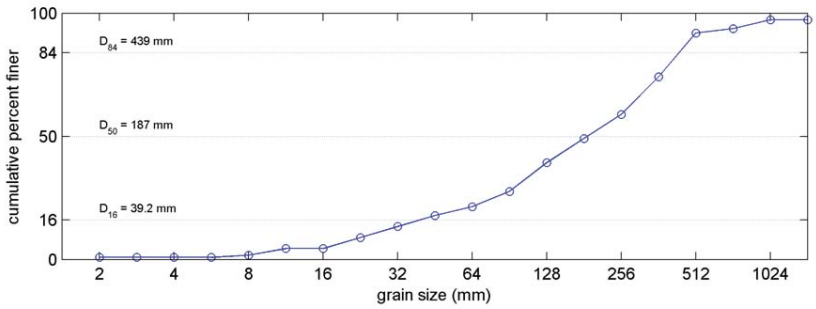
cumulative percent finer
grain size (mm)
D84 = 439 mm
D50 = 187 mm
D16 = 39.2 mm

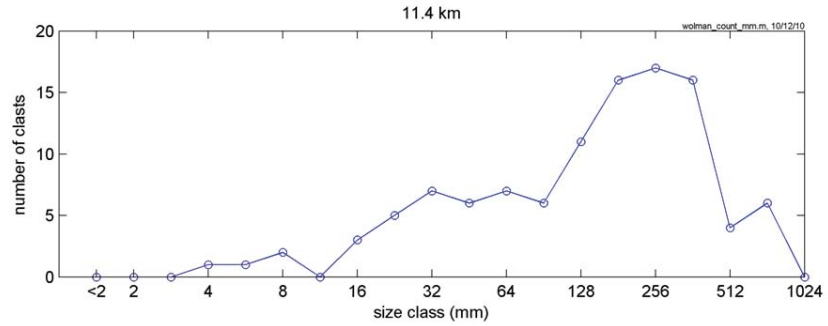
11.4 km
wolman_count_mm.m, 10/12/10
number of clasts
size class (mm)
<2
2
4
8
16
32
64
128
256
512
1024

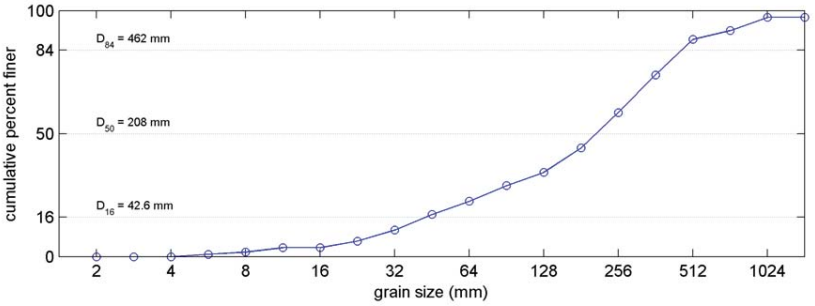
cumulative percent finer
grain size (mm)
D84 = 462 mm
D50 = 208 mm
D16 = 42.6 mm

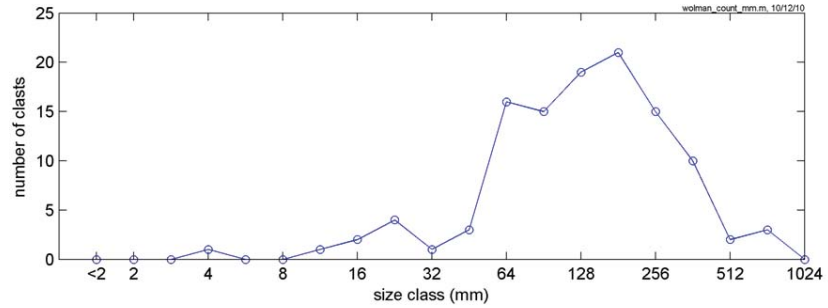
wolman_count_mm.m, 10/12/10
number of clasts
size class (mm)

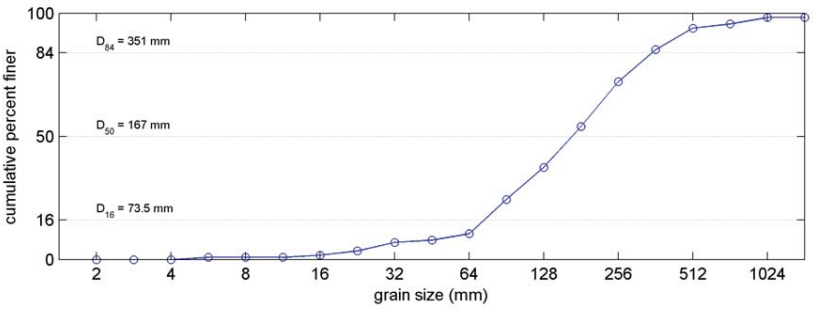
cumulative percent finer
grain size (mm)
D84 = 351 mm
D50 = 167 mm
D16 = 73.5 mm

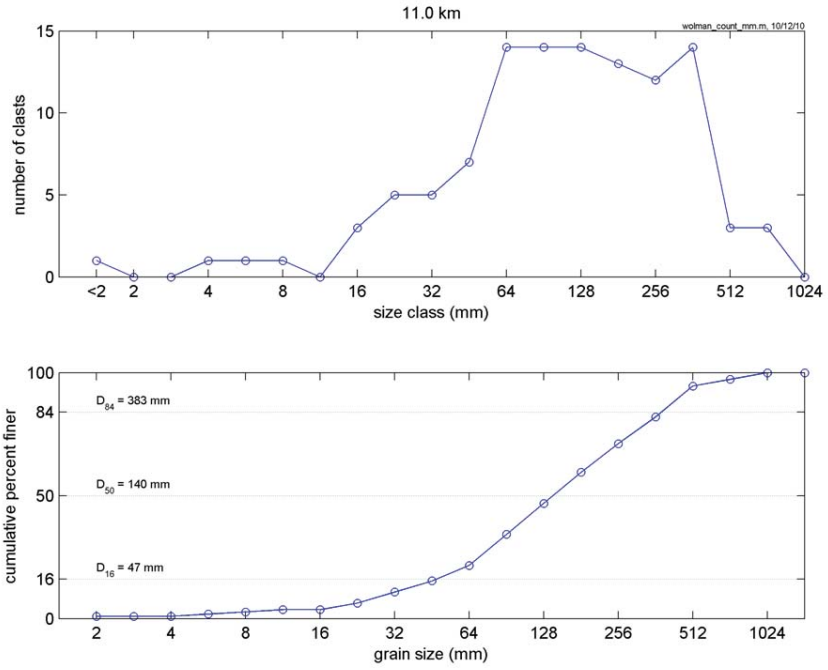
11.0 km
wolman_count_mm.m, 10/12/10
number of clasts
size class (mm)
<2
2
4
8
16
32
64
128
256
512
1024
cumulative percent finer
grain size (mm)
D84 = 383 mm
D50 = 140 mm
D16 = 47 mm

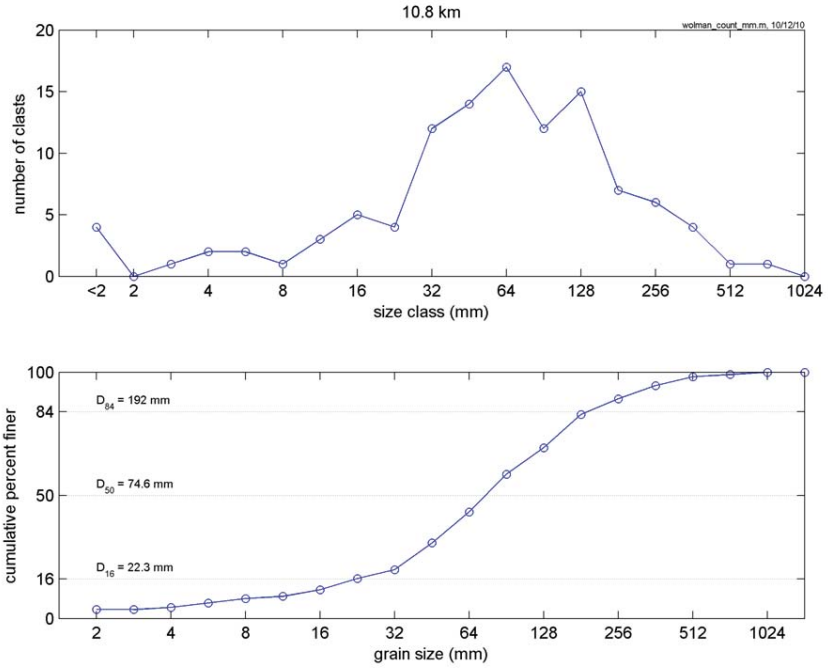
10.8 km
wolman_count_mm.m, 10/12/10
number of clasts
size class (mm)
<2
2
4
8
16
32
64
128
256
512
1024
cumulative percent finer
grain size (mm)
D84 = 192 mm
D50 = 74.6 mm
D16 = 22.3 mm

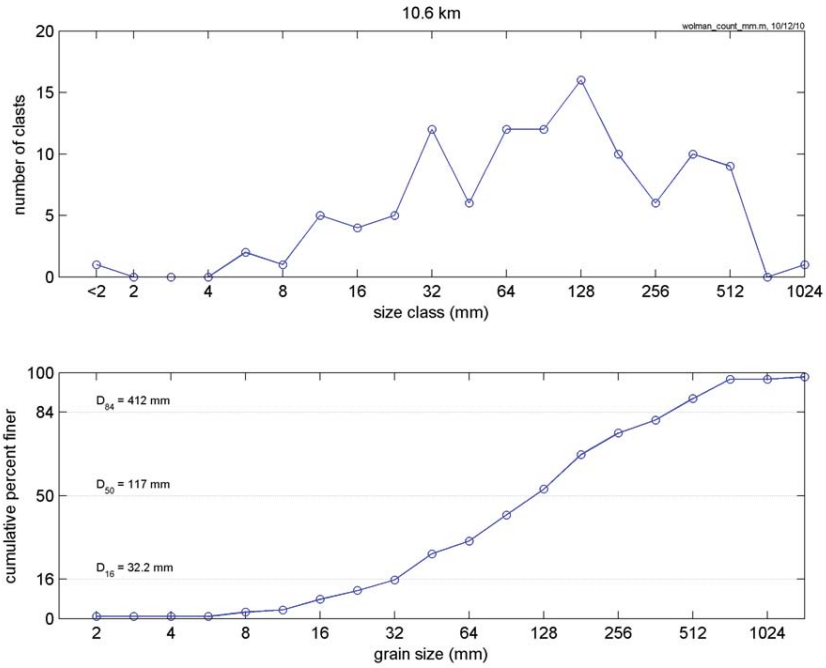
10.6 km
wolman_count_mm.m, 10/12/10
number of clasts
size class (mm)
<2
2
4
8
16
32
64
128
256
512
1024
cumulative percent finer
grain size (mm)
D84 = 412 mm
D50 = 117 mm
D16 = 32.2 mm